UNIVERSITÀ
DEGLI STUDI
DI TRIESTE

UNIVERSITÀ DEGLI STUDI DI TRIESTE

XXXIV CICLO DEL DOTTORATO DI RICERCA IN FISICA

A MULTISCALE APPROACH OF PHASE-CONTRAST TOMOGRAPHY FOR BREAST IMAGING

Settore scientifico-disciplinare: FIS/07

Ph. D. student
Lucía Mariel Arana Peña

Ph. D. program Coordinator
Prof. Francesco Longo

Thesis Supervisors
Prof. Renata Longo

Dr. Giuliana Tromba

ACADEMIC YEAR 2021–2022

Abstract

Breast cancer is a widespread and increasing problem among women globally. Traditional X-ray imaging techniques for detecting breast cancer suffer from poor soft-tissue contrast. Phase-contrast (PhC) imaging techniques, on the other hand, are able to address this issue by leveraging the phase-shift effects induced on X-rays traversing matter instead of the attenuation of X-rays. This study explores the use of synchrotron x-ray imaging for radiological applications and virtual histology of breast tissues using the propagation-based (PB) PhC technique at Elettra synchrotron (Trieste, Italy.) With the intense coherent photon beam, and long sample-to-detector distances, this technique has the potential to be an effective 3D imaging tool for detecting and diagnosing breast cancer while limiting radiation exposure. The study includes results from original experiments that support the clinical implementation of the PB for breast CT technique using a monochromatic synchrotron beam and a pixel size of 60 μm. These experiments range from optimizing a dedicated reconstruction algorithm for optimal clinical image visualization, to assessing an optical tracking method to compensate for patient motion artifacts. Moreover, a 3D thermoplastic breast immobilization system forseen to be used in a PB CT clinical environment is also presented. Additionally, the PhC micro-CT technique is explored as a useful alternative for breast sample virtual histology of paraffin-embedded breast sample blocks using a polychromatic synchrotron beam and a pixel size of 4 μm. This work shows the significant progress in evaluating the use of PhC CT as a tool for breast imaging in a multiscale approach, transitioning from whole breast sample imaging using PB breast-CT to virtual histology of breast tissue samples using PB micro-CT imaging. PB techniques allow for clear differentiation of breast structures, lesions, and microcalcifications at various resolutions making it a promising clinically-compatible tool for detecting cancer in full volume breast samples or for identifying structures in paraffin-embedded breast tissue samples.

Acknowledgements

Contents

Preface

Breast cancer is the most prevalent form of cancer among women worldwide, and its prevalence is alarmingly rising. Statistics (Bray et al., 2021) show that one in every twelve women will be affected by breast cancer at some point in their lives. In 2020, 685 million deaths due to breast cancer were reported. To significantly reduce the present mortality rates, different strategies for routinely detecting breast cancer early through screening, making an accurate diagnosis, and receiving the best care must be provided in a clinical practice, where the effective use of technology in a patient-centered manner is achieved through cooperation of a multidisciplinary team. Breast imaging tools allow to evaluate and have a better understanding of the breast structure and its abnormalities. The main limitation of conventional breast x-ray imaging is the lack of specificity to discern among the different healthy soft tissue components and invasive breast cancers usually due to the poor attenuation contrast among them (small differences in the atomic number and density of these low-Z materials), which can lead to false negative cases. On the contrary, phase-contrast imaging techniques (PhC) rely on the phase-shift effects induced on X-rays traversing matter rather than their attenuation, making it a promising tool for breast imaging to overcome the aforementioned limitation.

This thesis work aims to address some of the challenges of conventional breast imaging and explore the potential of PhC techniques for breast imaging in various scales. The work is based on a multiscale approach, combining different imaging techniques and analysis methods to study breast tissue at various spatial resolutions. The chapters in this thesis cover different aspects of research, as the management of breast cancer takes place in a multidisciplinary setting. In the realm of breast imaging, medical physicists contribute to this working force by using their analytical and problem-solving abilities in a clinical setting. In addition to clinical dosimetry, image quality, and the creation of radiation technologies for the investigation of tissue features and composition, a clinical medical physicist is responsible for ensuring that ionizing radiation is used in imaging facilities in a safe and efficient manner. Therefore, the

present thesis work aligns with the principles of Medical Physics 3.0 (AAPM) as "Every health-care facility can benefit from medical physics and every patient's care can be improved by a medical physicist".

The first chapter of the thesis work introduces the foundations of breast cancer along with ways that medical physicists might advance medical knowledge and practice for the benefit of patients. The physical characteristics of the several traditional x-ray breast imaging modalities are discussed, outlining the significance of each modality as well as its benefits and limita-tions. The use of X-ray PhC imaging techniques with synchrotron radiation is presented as an approach of overcoming the poor image contrast found in attenuation-based x-ray imaging modalities. The framework will describe propagation-based PhC imaging techniques from im-age production through the applications in medicine in the SYRMEP beamline at Elettra, the Italian synchrotron radiation facility in Trieste, demonstrating why they are an effective tool and have the potential to transform X-ray imaging.

Chapter 2 focuses on dosimetry in X-ray imaging, as X-ray breast imaging modalities require specific considerations and optimization practices due to the breast tissue's high ra-diosensitivity and to reduce radiation effects on the breast. The limitations of current breast dosimetry models are explored. This chapter presents the findings of a Monte Carlo simu-lation comparing the radiation dose estimates derived using homogeneous breast models in mammography versus the estimates utilizing realistic fibroglandular tissue distributions.

Chapter 3 presents the propagation-based (PB) PhC breast computed tomography (PB-bCT) as a 3D imaging tool capable of providing high spatial and high contrast resolution of breast tissues using a radiation dose level comparable to a standard 2-view mammography. In this context, the SYRMA-3D project is explained, under which most of the experiments of this thesis were carried out. The tomographic imaging setup is presented, together with the specialized patient support, image processing, tomographic reconstruction methods, and dosimetry system. A more thorough post-processing technique to remove ring-artifacts from the reconstructed images is also provided.

Chapter 4 describes the experimental PB-bCT developments towards a synchrotron clin-ical setting, where patients are required to lie in prone position on the patient couch while it rotates around the synchrotron beam and the detector during image acquisition. The patient's rotation and respiratory motion, along with the uncompressed breast pendant geometry, may give rise to involuntary movements of the breast, which may lead to motion artifacts in tomo-

graphic reconstructions and lower the diagnostic quality of the images. One approach to solve this problem involved the use of 3D-printed breast prototypes to create a 3D thermoplastic breast immobilization system. This chapter covers their creation, as well as the advantages and disadvantages of each prototype. Another approach to assess and compensate for such motion artifacts is discussed through the use of an optical tracking method, for which the results of the complete investigation, that encompassed three inter-connected purposes, is explained. In the journey towards the clinical implementation of PhC bCT requires the employment of powerful reconstruction algorithms, for which an original investigation conducted to customize and optimize a simultaneous algebraic reconstruction algorithm is described. Finally, a collaborative radiological assessment study with the Australian synchrotron is also presented.

Chapter 5 discusses the availability of PB micro computed tomography (PB-μCT) as a feasible option for virtual histology to provide additional information on breast tissue microarchitechture. While X-ray imaging tests play a non-invasive role in the detection and management of cancer, the only reliable technique to diagnose and stage cancer is through the evaluation and characterization of a breast tissue sample via histology. This chapter discusses how histology is restricted by the two-dimensional analysis of features to a small portion of the sample. Virtual histology using PB-μCT is introduced as a fully three-dimensional, non-destructive method with good soft tissue sensitivity to study specimens that require imaging down to a micrometer resolution that could overcome histology drawbacks. This proposed method could be a valuable asset for pathological evaluation, offering virtual slicing planes that enhance tissue visualization and that could serve as a guide for histological sectioning across sample regions of interest. Results from two original studies using PB-μCT virtual histology for breast samples are presented: one that serves as guideline in the choice of the imaging parameters for virtual histology studies and the second one, where original results of morphological comparative evaluation demonstrate the use PB-μCT as a prospective complementing tool to conventional histology.

Chapter 6 embraces both of the proposed methodologies to be used jointly for the multiscale imaging analysis of a breast sample in a multidisciplinary clinical context. The study that is presented in this chapter, bridges spatial resolutions within a same sample: from the radiologic level of whole breast imaging to the virtual histology level of an extracted paraffin-embedded block sample imaging. The volume co-registration of a full specimen scan via PB-bCT and the paraffin-embeded breast sample scan via PB-μCT is explained. Moreover, the

multiscae technique is presented as a potential tool for improving clinical decisions, specifically for pathologist, who could benefit from either the 3D inspection the entire 3D organ to decide the best region to extract tissue sample, as well as inspection the 3D paraffin-embedded block, to locate "in-depth" structures prior section cutting, thus, enhancing diagnosis and prognosis.

The presented findings are achieved in an interdisciplinary context, where medical physicists worked closely with imaging specialists, histologists, radiologists, and physicists who specialize in synchrotron radiation and innovative imaging setups. It is the author's belief that thanks to the expertise in both technical and clinical aspects, medical physicists may be the key to advancing techniques and encouraging collaboration in interdisciplinary settings, with the aim of improving breast cancer care and outcomes for women worldwide.

Chapter 1

General Introduction

1.1 Medical physics in healthcare

A large number of physicists have used their skills to analyze an environment, detect problems and create novel solutions that are nowadays used in the field of medicine to promote and benefit human health. They gave rise to what we nowadays know as Medical Physics. To this day, this function is essential for the research and creation of new imaging technologies and radiation therapy. Medical physicists combine their technical, analytical and problem-solving skills with an acute knowledge of the clinical setting to contribute to healthcare. Specifically, they ensure that radiation doses from medical equipment are applied correctly to patients and are key to the safe and effective use of radiation in medical environment (International Atomic Energy Agency, 2018), such as in the battle against cancer, as it is becoming more prevalent as the leading cause of premature death worldwide (Bray et al., 2021). According to GLOBOCAN 2020 estimates, 2.3 million new cases and 685,000 deaths fatal cases of breast cancer were detected globally. This accounts for one in four new cases and one in six cancer-related deaths worldwide (Sung et al., 2021). Breast cancer is the most common type of cancer in women, which has now surpassed lung cancer as the main cause of cancer incidence. Age, family history, hormone exposure and lifestyle factors play an important role in increasing breast cancer risk amongst different female populations (Aydiner et al., 2019). Strategies for the primary prevention of breast cancer is of significance due to the rise of disease incidence and the inevitable risk factors. The implementation of population-based screening programmes is the most reliable way for an early detection of breast cancer (Oeffinger et al., 2015; Canelo-Aybar et al., 2022). In this context, medical physicist work to optimize radiation-emitting equipment to perform high quality imaging for the detection and diagnosis of breast cancer, as well as to provide safe and effective doses for radiotherapy treatment. Optimization is a multidisci-

plinary task involving the medical physicist, radiologist, radiographer, hospital and department management (International Atomic Energy Agency, 2014). In order to assure high quality services of these practices in the modern era of diagnostic radiology, clinically qualified medical physicists ensure a safe and effective performance of the current equipment by carrying out quality performance activities to verify that it complies with standard requirements. They have a leading role in a comprehensive framework of continuous quality improvement in a diagnostic imaging facility, as they must also analyze the needs and specifications for acquirement of any equipment (Delis et al., 2017). Patients can benefit from the unique skills provided by medical physicists as health professionals for the development and practice of medicine, as it summed up by the motto of the initiative Medical Physics 3.0 (AAPM): "Physics for every patient".

1.2 Breast structure and lesions

Breast imaging involves evaluating the morphology of macroscopically observable breast structures. To optimize the design and imaging techniques, it is important to understand the basic premises of breast anatomy and its lesions. Distinguishing between the many components of normal tissue is very useful in order to identify both benign and malignant alterations and to, subsequently, produce an accurate diagnosis. This section intends to broaden the clinical context of the breast anatomy and lesions since the management of cancer involves a multidisciplinary approach.

The morphological structure of the breast consists of various functional and supporting structures, and it can generally be considered as having mainly three major elements: skin, subcutaneous tissue, and breast parenchyma, which is formed of adipose tissue (fat), fibrous stroma, and glandular epithelium. For breast models used in medical physics, explained in detail in the following chapter, the breast can be considered of being composed of skin, adipose tissue and fibroglandular tissue. The fibroglandular tissue comprises the major portion of the nonlactating adult breast, and the relative proportions of fibrous tissue and adipose tissue vary with age and among individuals (Mills, 2012). In reality, the structure of the breast is a complex network of lobes and ducts, arranged like a branch with a bunch of grapes, surrounded by tissues that provide nutrition and protection, as it is illustrated in fig.1.1. The glandular epithelium comprises approximately 10–15% of the adult female breast and it is composed of 15–20 lobes. Each lobe has many small glandular sac-like structures (similar to grapes), called lobules, which are the functional and structural glands in charge of milk production. The

lobules end in dozens of tiny bulbs, known as lobular acinar units or acini, that open into the terminal ductal lobular units (TDLU) (Aydiner et al., 2019). The lobes, lobules, and acini are all linked by lactiferous ducts (the branch of the grapes) , that lead to the nipple in the center of the breast. Fig. 1.1 on the left shows the scheme of a developed breast lobular unit embedded within an extra lobular stroma composed of varying amounts of fibrous and adipose tissue.
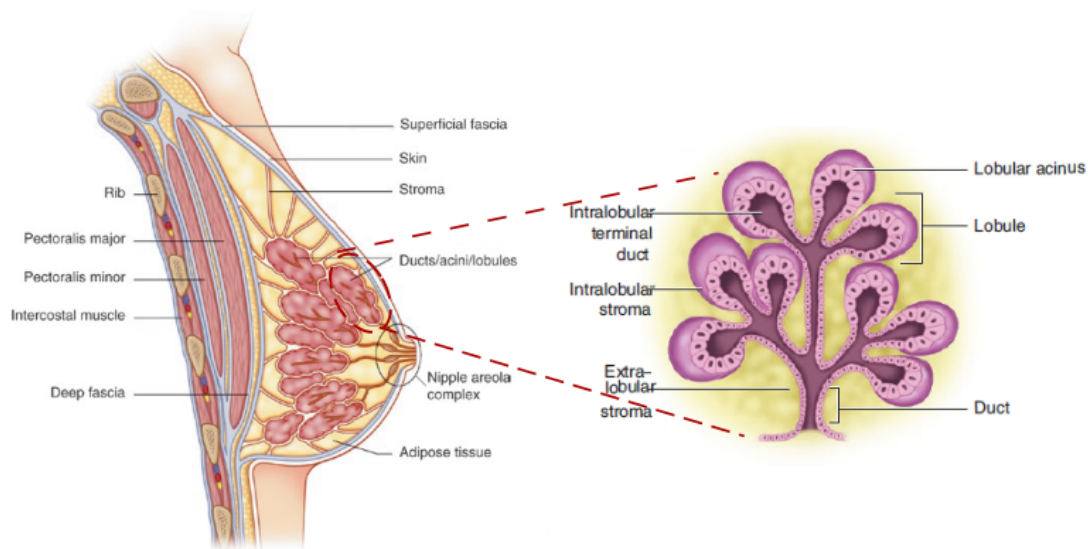
Figure 1.1: Illustration of the components of the breast (left), and an inner-view of the structure of a fully developed breast lobular unit (right). Images adapted from Aydiner et al. (2019).

Breast lesions constitute a heterogeneous group of breast diseases with variable patterns of presentation, morphology, and clinical behavior, and they are traditionally classified as benign and malignant conditions. Their behavior can, in the wide majority of cases, be predicted with a reasonable degree of precision (Rakha et al., 2016). Breast abnormalities may be associated with palpable breast masses that are usually discovered through breast self-examination. Upon a suspicious area in the breast, such as a breast lump found in a clinical exam or other signs in radiological images, patients are required to perform further clinical examinations, breast imaging and biopsies. A breast biopsy is a procedure that involves removing a sample of breast tissue for testing, after which pathologists examine and provide a diagnosis. Therefore, a breast biopsy can reveal whether the area in question is cancerous or not. Following the evaluation of such exams, patients may be diagnosed with noncancerous or benign breast tumors, such as breast cysts, fibroadenomas, and intraductal papillomas. The latter are benign breast neoplasms that develop within the mammary duct and were the focus of one of the studies carried out in this thesis. They get their name from their microscopic appearance and papillary architecture.

With a prevalence of 2-3% in the general population, benign intraductal papillomas are a rare condition that typically affects women aged 30 to 55 (Aydiner et al., 2019). For benign tumors, a breast conservative treatment is usually used. There are a variety of benign breast diseases, such as mastalgia, nipple discharge, and breast inflammation, that will not be discussed here as it is not the scope of this thesis work.

On the contrary, in confirmed cases, patients are referred to perform a lumpectomy or mastectomy, both surgical procedures to remove cancerous or other abnormal breast tissues, which are also studied by pathologists. A lumptectomy is a breast conserving surgery, usually accompanied with radiation therapy. It is considered safe and preferential for early detected cancers, since it provides the same level of survival rates as mastectomy and much better cosmetic effect (Mansell et al., 2017). In this kind of treatment, a small amount of normal tissue surrounding the tumor, known as surgical margin, is also removed and evaluated through histology to perform a microscopic diagnosis and determine the presence of cancer between the tumor itself and the outer edge of the margin. The definition of the margin is highly debated, as its delineation is critical in breast-conserving surgery when assessing the risk of recurrence, and its delineation will determine the course of treatment while evaluating the risk of recurrences, and whether additional surgery may be recommended.

Clinical staging of a cancerous tumor employs a multidisciplinary approach, involving a combination of physical examinations and imaging findings to classify and determine tumor characteristics such as size, type, location among other parameters. The type of breast cancer is determined by the specific cells in the breast that become cancer. Carcinomas are classified as in situ or invasive. Most breast cancers are believed to arise from the TDLU. In situ carcinoma cells are limited to the ductal-lobular system of the breast, where the ductal epithelium is surrounded by a basement membrane. Invasion through this membrane distinguishes an invasive cancer from an insitu carcinoma. Invasive carcinoma cells spread outside this structure and can also spread, or metastasize, to other parts of the body. Additionally, calcifications may accompany benign or malignant lesions. Their identification and distribution is an important factor in characterizing calcifications as suspicious or benign (Wilkinson et al., 2017). Patients that show microcalcifications suggestive of malignant lesions will will undergo biopsy, whereas the calcifications indicating a low chance of malignancy, are usually recommended for observation, with follow-up breast imaging.

1.3 Conventional X-ray imaging techniques

The role of physics in medicine has been on the rise since the discovery of X-rays in the nineteenth century, and its application to reveal the internal structures of the body has become the foundation of diagnostic radiology. Breast imaging is a crucial part of the diagnosis of breast cancer and directs surgical and therapeutic options. The design of X-ray equipment needs to be optimized to deliver the minimum radiation dose to breast to achieve a proper subject contrast, implemented with an x-ray detector with a sufficient spatial resolution to detect breast lesions, and resolve between the different types of breast lesions and its associated microcalcifications. Breast imaging systems can be distinguished according to the type of detector and image-acquisition geometry that include flat-panel systems, scanning systems, and photostimulable phosphor (PSP) systems and most recently photon counting detectors. As a rule of thumb, the digital detector must image as much of the breast tissue as possible to avoid missing lesions and have sufficient spatial resolution to allow adequate visualization of the fine detail structures in the breast (less than 100 μm (Yaffe, 2006)). One of a number of essential elements in the production of an optimal diagnostic mammogram is the breast compression during image acquisition. The breast is mechanically compressed by placing it between a flat compression paddle and the breast support table. The full area compression paddle matches the size of the image receptor. There are several benefits to firm breast compression: it reduces breast thickness, which reduces scattered x-rays and lowers the absorbed dose to the breast; it separates tissue components, which lessens overlapping anatomy; and, lastly, it minimizes any potential unintended motion of the breast. Minimizing breast thickness through compression will maximize image quality, while increasing the possibility of small cancer detection (Poulos and McLean, 2004). However, numerous patients usually express their discomfort and pain during a mammogram (Rutter et al., 1992; de Groot et al., 2015). In some cases the pain can even discourage patients to participate in future screening programs (Papas and Klassen, 2005). Different breast imaging procedures (some with and some without breast compression) can be carried out to detect and diagnose breast cancer w, such as mammography, digital breast tomosynthesis (DBT), breast ultrasound (US), breast magnetic resonance imaging (MRI), and dedicated breast computed tomography (bCT). In this section, the main radiological breast procedures that are currently used in the clinics are discussed.
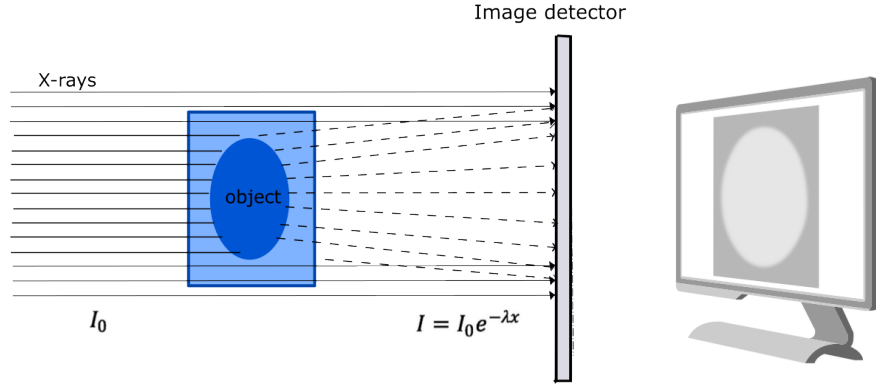
Figure 1.2: A schematic representation of x-ray interaction with an object, where I_0 is the incident x-ray beam, I is the attenuated x-ray beam emerging from the object. Artwork by the author.

1.3.1　Attenuating X-rays for medical imaging

Clinical radiological exams rely on the differential absorption of X-rays traversing the body, known as conventional attenuation-based (or absorption-based) x-ray imaging. The mathematical model of attenuation based x-ray imaging process considers a monochromatic x-ray source that emits photons I_0 parallel to the z direction that impinge an object whose image is recorded in the xy plane in a detector with a linear response, as seen in figure 1.2.

The behavior of x-ray traversing matter is varied, and it depends on different factors, such as the incident X-ray energies, the composition of the object they are traversing, and its thickness. How much primary x-rays can penetrate a volume of material is tied to the linear attenuation coefficient $\mu(x,y,z)$, that is dependent on density of the material, and to the thickness of the object dz. Medical imaging equipment typically operate in the range from 15-100 keV, where the interaction of x-rays with matter is dominated by the photoelectric interactions and scattering, that result in a variation of the impinging X-ray beam's intensity I_0. Photoelectric interactions are very sensitive to small atomic number (Z) differences in the 15-30 keV range, where the typical dependence of the photoelectric effect cross-section per atom, τ is $\propto Z^4$ (International Atomic Energy Agency, 2014). The transmitted X-ray intensity $I(x,y)$ that reaches the detector is converted to visualize the distribution of the absorbed energy as a brightness projection image. This image is a two-dimensional projection of the three-dimensional distribution of the X-ray attenuating properties of the tissues (Flower, 2012). The x-ray attenuation mathematical model is expressed by the Beer-Lambert law (Cunningham and Johns, 1983)):

$$I(x,y) = I_0 e^{-\int \mu(x,y,z)\,dz} \tag{1.1}$$

In practice, there is a large difference between the X-ray spectra before and after passage through the patient. Since the heterogeneous patient attenuates low-energy X-rays more effectively than high-energy ones, mostly due to photoelectric absorption (Attix, 1986), the transmitted beam becomes proportionately richer in high-energy photons, and hence more penetrating, or 'harder'. Furthermore, by spreading or 'blurring' the incident energy away from the initial interaction location, secondary radiation generated from the primary x-ray interactions has the potential to degrade the incident beam energy (Cunningham and Johns, 1983). Generally speaking, if the incident x-ray spectrum is too soft, then the transmission is very low, leading to few x-rays reaching the detector. Low-energy photons are more likely to be absorbed by the patient, contributing to a high dose on patient and not to image contrast. Yet, if the incident x-ray spectrum is too hard, the high transmission decreases image contrast. A compromise between the requirements of low dose and high image contrast must be achieved.
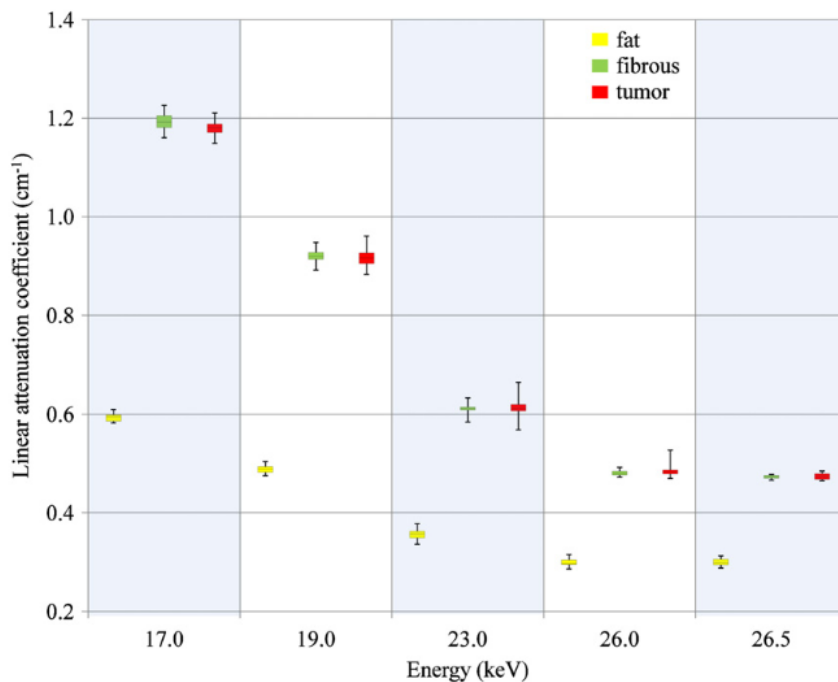
Figure 1.3: X-ray measured linear attenuation coefficients for breast tissues. The attenuation differences between normal fibroglandular breast tissue and an infiltrating ductal carcinoma are very small. (Taken from Chen et al. (2010))

This challenge is specifically difficult when using x-rays for soft-tissue imaging, as in the case of the breast cancer detection, for two main reasons:

- First, the linear attenuation coefficients in Figure 1.3 show that healthy (fibrous) and malignant breast tissues(carcinoma) differ very slightly, which translates into a poor contrast

amongst them (Johns and Yaffe, 1987; Chen et al., 2010), complicating the diagnosis that may lead to false-negative cases. Additionally, the graph shows a decrease in the coefficient values with increasing energy, thus, requiring the use of low energy X-ray spectra to emphasize the composition differences of breast tissues.

- And second, breast tissues are highly radio-sensible, which translates into an increased risk of cancer induction by low dose radiation exposure (National Research Council, 2006).

It is important to understand the magnitude of risk associated with the radiation dose delivered in x-ray breast imaging techniques, by quantifying the absorbed dose to the breast during x-ray based imaging using the Mean Glandular Dose (MGD), that will be further discussed in the following chapter.

1.3.2 Digital Mammography

Mammography is a low-cost, low-dose radiation procedure with the sensitivity to detect breast cancer in its early stages. In the past, direct exposure film was used for x-ray mammography, which resulted in images with weak contrast and inadequate diagnostic quality. The need to increase sensitivity and specificity in the identification of breast cancer served as the driving force behind the creation of 2D digital mammography (DM), which is the most used clinical tool for the early diagnosis of breast cancer in the present. Indicative breast cancer features that are visible in mammography include solid masses, particularly those with irregular margins or spiculations, architectural distortions of breast structures and clusters of microcalcifications. Breast Imaging Reporting and Data System (BIRADS) by the American College of Radiology standardizes the terminology used in mammography, as well as the breast density.

Screening mammography is carried out to detect breast cancer in the asymptomatic population, where usually two x-ray images of each breast, in the mediolateral oblique (MLO) and craniocaudal (CC) views, are acquired. Prior to the introduction of screening mammography, the majority of cases ductal carcinoma in situ (DCIS) went undetected until a palpable tumor developed. However, during the 1980s, the reported prevalence of DCIS has increased tenfold as a result of the screening mammography (DeSantis et al., 2014). On the contrary, diagnostic mammography acquisitions are performed to evaluate palpable lesions or assess suspicious results detected by screening mammography. The diagnostic mammographic examination may include additional x-ray projections, magnification views, and other breast imaging modalities such as ultrasound and magnetic resonance imaging with the aim of minimizing the need for

surgical procedures and, at the same time, minimizing the potentiality of missing a clinically relevant lesion.

1.3.2.1 Physical requirements

To achieve the different views of the breast, the mammography unit needs to be able to rotate, as well to adjust the elevation to accommodate patients of different heights. The breast is compressed through a transparent compression plate to provide more uniform attenuation. Previous findings suggest that excessive pressure during mammography may lower sensitivity. In contrast, if pressure is low, this may decrease specificity (Holland et al., 2017). Another factor to take into account during this procedure is based on research by Dustler et al. (2012) which suggests that poor breast positioning prevents proper compression of the breast in mammography, which in turn could lessen the benefits of the procedure and give rise to an undetected cancer (Bae et al., 2014). Therefore, it is important to apply a correct compression in an optimal breast position. Depending on the nature and thickness of the compressed breast tissue, the ideal effective energy for mammography may be achieved by tuning the spectrum through the selection of the rotating anode material (usually Molybdenum, Rhodium or Tungsten), the addition of filtration material, and kilovoltage (International Atomic Energy Agency, 2014). According to monoenergetic models, the ideal spectral energy range is from about 15 to 25 keV (see fig. 1.3), but since it is difficult to estimate the attenuation of the breast by visual inspection, digital mammography units are equipped with an Automatic Exposure Control system, which senses the compressed breast thickness and the transmitted exposure rate to employ an algorithm to choose the X-ray target/beam filter/tube voltage combinations automatically. Additionally, anti-scatter grids ought to be included as well to enhance subject contrast (Yaffe et al., 1995). The image-acquisition geometry and the detectors, which are the heart of the imaging systems, range from flat-panel systems to photostimulable phosphor (PSP) systems and most recently photon counting detectors. Currently, commercially available detectors have square detector elements (dels) with dimensions of 50, 70, 85, and 100 μm (Yaffe, 2006) to comply with the high-resolution needs of breast imaging.

1.3.3 Digital Breast Tomosynthesis

Digital breast tomosynthesis (DBT), is a semi-three-dimensional imaging approach that has been developed in the last ten years to reduce the masking effect of tissue overlap that is present in mammography. Most DBT systems consist of the same fundamental components as digital mammography with the exception that the DBT x-ray tube can rotate around the compressed

breast at a number of different x-ray source angles, ranging from 15-60°. The resulting projections are reconstructed into a series of thin high-resolution slices. Digital breast tomosynthesis has shown to offer some diagnostic improvements and screening accuracy resulting in fewer recalls and a quasi-3D lesion localization (McDonald et al., 2016). Current x-ray imaging modalities lack specificity for differentiating ILC from other invasive breast cancers, for which further details will be explained in 1.4, yet studies have shown that DBT improves the detection of invasive lobular carcinoma lesions by more clearly depicting architectural distortions and spiculations (Grubstein et al., 2016). Various studies (Patterson and Roubidoux, 2014; Lång et al., 2016; Phi et al., 2018) have shown that this method can address some of the limitations of conventional mammography and offer diagnostic advantages over DM, even for screening purposes. In spite of an increase by 20% in patient's radiation dose during a DBT examination, the cancer detection rate is also improved in about 15–30% and a recall rate decrease about 15–20% (Gilbert and Pinker-Domenig, 2019).

1.3.3.1   Physical requirements

For every acquisition, a series of 10–20 low dose exposures, each with a dose of 5–10% of a typical single-view mammography, are made. Since each exposure only requires a small amount of radiation, detectors for DBT must also possess additional qualities like high quantum efficiency, low noise, and a quick reading time to minimize the possibility of patient movement during the acquisition time, which could impair the visibility of tiny structures like microcalcifications (Smith, 2008). On the other hand, compression of the breast for tomosynthesis is similar to that of conventional mammography. However, since the issue of tissue overlap is improved by DBT, some reduction of compression is also possible, hence, improving patient's comfort (Förnvik et al., 2010).

Although there is evidence to support the use of DBT as a screening tool (Gilbert et al., 2016; Phi et al., 2018), there are still a number of concerns to be resolved about reading time, overdiagnosis, and cost efficiency. Although adding DBT to DM as an adjunct tool improves accuracy, the radiation dose is significantly increased, and a longer examination time is required (Lam et al., 2017). Nevertheless, the European Commission Initiative on Breast Cancer (on Breast Cancer, 2022) on breast cancer screening and diagnosis stating that for screening at ages 50-69 it is strongly recommended to use either DBT or DM and not using both DBT and DM. On the other hand, With the use of a synthetic mammogram (SM), that is a 2D image created from the same dataset the from which DBT slices are based on, the additional dose is-

sue could be substantially reduced. Additional studies with longer-term follow-up are needed. More details on breast tomosynthesis with an emphasis on its medical physics aspects can be read in the reviews by Sechopoulos (2013a,b) and in Butler et al. (2019).

1.3.4 Breast Computed Tomography

Breast computed tomography, a huge technological advancement, addresses many of the drawbacks of DM and DBT in a relatively new method to breast imaging. In general, to obtain a breast tomographic image, a certain number of radiographic images, or projections, at different angular positions of the breast must be acquired. The projections are subsequently incorporated into a reconstruction algorithm, which inverts the tomographic problem, creating a virtually reconstructed x-ray attenuation maps of the breast. This dedicated breast approach offers images that are entirely three-dimensional, enhanced for contrast, free of tissue overlap, and without breast compression. Rapid acquisition is made possible with a bCT system, decreasing anatomical noise and alleviating patient discomfort (Boone et al., 2001; Lindfors et al., 2008, 2010; O'Connell et al., 2010; Sechopoulos et al., 2010; Kalender et al., 2012). Breast computed tomography has been studied since the 1980s, but due to technical limitations, it had not been implemented in clinical practice. Actually, the first clinical studies comparing visibility in bCT with lesions found in screen-film mammography (Lindfors et al., 2008) were published more than 5 years after the first quantitative estimations of radiation dosage from a specialized bCT (Boone et al., 2001). The advantages of bCT over MG and DBT include high spatial resolution 3D images of the breast arising from isotropic voxels that represent X ray attenuation coefficients of the breast tissue. The findings of Lindfors et al. (2008) revealed that, although bCT was superior than screen-film mammography for the visualization of masses, it was inferior for the visualization of microcalcifications, which, it has already been stated previously in this chapter, is one of the requirements of breast imaging. Ongoing research is still motivated until today on how to optimize the imaging technology to match high spatial resolution requirements with a low dosage CT scan.

1.3.4.1 Physical requirements

. Many efforts and interest in the development of bCT scanners have been carried out by different groups of research creating the first bCT prototypes based on cone beam geometry (Sarno et al., 2015). To image a non-compressed breast means to increase the X-ray beam energy in order to have a sufficient transmission through the organ. Images are generally acquired at a tube voltage of 50-80 kV, contrarily to mammography (30 kV). As stated in sec. 1.3.1, the

relevant x-ray interaction processes in the breast imaging photon energy range are photoelectric absorption and scattering, specifically coherent scatter, and Compton scatter. The x-ray interactions in the energy range used in bCT are dominated by the Compton cross section τ_c, which is only proportional to Z in comparison to $\tau \propto Z^4$ in mammography International Atomic Energy Agency (2014). Increasing the energy comes with the cost of further reducing subject's contrast, thus requiring high contrast sensitivity to provide tissue differentiation. The clinical recognition of this practice has been achieved only in very recent times (Uhlig et al., 2019; Berger et al., 2019), and currently, there are only two bCT scanners available on the market Koning (2022) with an X-ray flat-panel detector and AB-CT (2022) with a photon-counting detector, but their use is not widespread and their status in diagnostic imagingis slowly gaining recognition. The mean glandular dose (MGD) the different bCT systems show some discrepancies, such as it is presented in the works of Boone et al. (2001); Sechopoulos et al. (2010); O'Connell et al. (2014) and Wienbeck et al. (2017) without contrast and Uhlig et al. (2019) with post-contrast enhancement. Therefore, there is a need to optimized protocols and technical advancements to reduce bCT radiation exposure. The European Reference Organisation for Quality Assured Breast Screening and Diagnostic Services (EUREF) limits the mean glandular dose to the breast to 5 mGy for a two-view screening DM in a normal-size breast , but a diagnostic exam generally requires more than two views, for which there is no recommendation for MGD limit. Even though the currently intended use for bCT is diagnostic, it is desirable to stay within the limit imposed for DM screening where we can safely assume the same high benefit-to-risk ratio (Zhu et al., 2022). Fan beams and photon-counting detectors are being implemented in the new generation of bCT systems (Longo et al., 2016; Kalender et al., 2017) amongst spiral beams and to overcome some of the limitations of the first generation bCT.

Since bCT is a three-dimensional imaging procedure without tissue overlap, no breast compression is needed for scanning. During acquisition, the patient is lying prone on a dedicated patient table with an opening where one breast can hang in a pendant geometry. To image the non-compressed breast, an increase in the X-ray beam energy is needed in order to have a sufficient transmission through the organ, and hence, an increase in the dose occurs as well. As it was already introduced in 1.3, women decline to undergo mammography examinations due to pain or discomfort, therefore, a great advantage of bCT is the lack of compression, which in turn might have the potential to increase the compliance rate of women in undergoing this methodology for screening. Studies have shown that during a bCT examination, women feel as

comfortable as or, more comfortable than in a mammography examination (O'Connell et al., 2010), with the major areas of discomfort being the neck, the shoulder, and the ribs (Boone et al., 2006) from the positioning on the patient table. Such issues can be improved by optimizing the design of the dedicated patient table (Rößler et al., 2015) . Another advantage of the lack of a compression system is shown by a recent study by O'Connell et al. (2018) where is found that contrast administration in uncompressed breasts is ideal, as it avoids the confounding effects of compression on contrast agent uptake and may facilitate quantitative evaluation in contrast enhancement bCT. Further aspects of bCT clinical systems, the advantages and limitations can be found in the related literature (Ning et al., 2007; Betancourt-Benitez et al., 2009; Benítez et al., 2009; Sechopoulos et al., 2010; Zhu et al., 2021).

1.3.5 Supportive diagnostic tools

Mammography is still the primary screening test with well-recognized limitations. However, other imaging modalities that work with non-ionizing radiation have been used as adjunct screening tools on women who may be at increased risk for the development of breast cancer (Lee et al., 2010), providing complementary information to health professionals that improves the accuracy of the diagnosis. A brief introduction of some of these modalities is presented next.

1.3.5.1 Ultrasound

In contrast to the images of the attenuation properties of tissues that are achieved in the previously mentioned examinations, ultrasound technology employs ultrasound energy and the body's acoustic characteristics to produce a real-time image from both stationary and moving tissues. Ultrasound (or ultrasonography) can be used to assess the morphology and orientation of internal structures, to distinguish cysts (typically benign) from solid masses (often cancerous), to determine the sonographic characteristics of solid masses and to evaluate palpable lumps in young women. In most cases benign and malignant lymph nodes cannot be distinguished from each other mammographically (Walsh et al., 1997) and ultrasound modality can provide further diagnosis. Recent improvements in ultrasound resolution and advances in colour Doppler technology have meant that benign and malignant lesions can be identified with some degree of confidence, particularly when used in conjunction with clinical and mammographic assessment . Moreover, The convenience to produce real-time images makes ultrasound a great tool for guidance for percutaneous biopsy and other interventional processes.

Ultrasound can also be used to evaluate the morphology and direction of internal struc-

tures, in addition to evaluating palpable lumps in young women, separate cysts from solid masses, which are frequently malignant, and determine the sonographic properties of solid masses. Most of the time, mammography cannot discriminate between benign and malignant lymph nodes (Walsh et al., 1997); however, ultrasonography technology can help with the diagnosis. Recent advancements in color Doppler technology and ultrasonic resolution have made it possible to distinguish between benign and malignant tumors with some degree of certainty, especially when used in conjunction with clinical and mammographic examination (Teh and Wilson, 1998; Watson, 2000). Additionally, ultrasonography is a great tool for guiding percutaneous biopsies and other interventional treatments due to its ease of producing real-time images.

1.3.5.2   Magnetic Resonance Imaging

MRI technique uses the magnetic properties of the hydrogen atoms in the tissues to produce images of the breast in a dedicated breast magnetic resonance imaging machine (bMRI), generating extensive information about the nature of breast lesions due to the strong tissue contrast sensitivity that the technique provides, allowing differentiation between benign and malignant tumors. There is a clear benefit of using bMRI on patients who exhibit clinical symptoms of breast disease, as a supplementary exam to traditional breast imaging, on women whose breasts are radiographically dense, and on people for whom additional testing has been requested as a result of an abnormal screening mammogram or as a follow-up to previous imaging findings (Bleicher and Morrow, 2007). During acquisition, the patient is lying prone on a padded patient table with a an opening where both breasts can hang in a pendant geometry. Radio waves and powerful magnets coming from the scanner are used to apply sequences of changing magnetic fields to the breast. Following application, the nuclei of the atoms in the breast realign into proper position, emitting radio signals. By measuring the signal variations in the protons' motion in fat and water the breast image can be created. The administration of a contrast dye, usually Gadolinium, is required to highlight the increase in signal intensity from Tumor-associated blood vessels, since cancer tends to have more vascularity than normal breast tissue (Slanetz et al., 2020). The exam typically lasts 30 to 45 minutes, which is far longer in comparison to the scanning time in DBT. Long scanning times make highly likable for the patient to move, generating artifacts in the image. The appearance of artifacts in the images creates confusion, which leads to a misinterpretation and false-positive diagnoses (Millet et al., 2012).

However, the high spatial resolution of bMRI images allows a breast lesion's morphology

to be examined in greater depth, which can turn into an increase in specificity for cancer staging. bMRI can also detect primary breast cancers and extra foci of malignancy that are occult to routine imaging (Enriquez and Listinsky, 2009). A variety of pathological parameters are used to assess prognosis and predict the therapeutic response of breast cancer patients, for which this technique is found to be useful to direct biopsies since the clear localization of the malignant lesions could optimize lumpectomy surgery and reduce the possibility for histologically positive margins (Harms, 1996).

Although MRI is not frequently used for breast cancer screening, patients at high risk for the disease, such as patients with dense breast or those who have been proven or believed to be carriers of the gene associated with breast cancer susceptibility (BRCA), may benefit from a screening breast MRI in addition to a yearly mammogram. Studies have revealed that 14.7 new incidences of cancer per 1000 patients were detected when bMRI was used as a supplemental technique in patients who have already undergone mammography and ultrasonography (Drukteinis et al., 2013). A challenge of breast MRI includes the expensive cost of the equipment, which makes a inaccessible method for different populations. A higher obstacle occurs for the detection of calcifications, as they are detectable in bMRI only by the application of phase derivative imaging using even more expensive ultra high-field scanners (De Leeuw et al., 2014). More information on the state-of-the-art for breast MRI modalities can be found in Mann et al. (2019).

For further reading about various breast imaging modalities and their advances, including the ones that are not mentioned in this work, can be found in the reviews by Karellas and Vedantham (2008); Wallis et al. (2007); Iranmakani et al. (2020) and Galati et al. (2022).

1.4 Limitations of conventional breast imaging

As already mentioned in section 1.3.1, an intrinsic limitation of any attenuation-based x-ray breast imaging techniques is the difficulty of discriminating soft tissues that feature a poor attenuation contrast. Breast carcinomas present similar density as their surrounding tissue, making even harder to detect. Moreover, the characteristics of certain types of cancer defy the radiological diagnosis, such as the case of invasive lobular carcinoma (ILC), because its invasive cells often preserve the architecture of the ducts and elude formation of palpable breast masses. This limits the sensitivity of detection (Helvie et al., 1993) and leading to higher false-negative rates (Lopez and Bassett, 2009).

For mammography imaging technique, studies have found an association between high

breast density and decreased sensitivity, being as low as 30%–48% according to (Kolb et al., 2002; Pisano et al., 2005), and specificity of mammography, which turns into larger and more advanced tumours at the time of detection. According to the results of Breast Cancer Surveillance Consortium (BCSC, 2022) from 2005-2010, the sensitivity of mammography is about 57% in women with dense breasts and it increases up to 93% in women with high adipose tissue sensitivity. Additionally, the inherent nature of the technique records a two-dimensional (2D) image of a three-dimensional (3D) structure, which may result in an overlap of the projections of normal fibroglandular tissue that can either mask underlying malignancy or show abnormalities resembling cancer. This poses a limitation in the diagnosis, leading to high rate of false positives implying additional imaging and/or unnecessary biopsies, often distressing the patient (Greenwood et al., 2018). A 3D breast imaging technique could provide a solution to this limitation.

In the case of DBT, which can surpass the overlap of projections issue that arises in mammography up to a certain degree, it can increase the patient's radiation dose by 20% during a DBT examination (Gilbert and Pinker-Domenig, 2019). Furthermore, the spatial resolution in the planes perpendicular to the detector is significantly reduced in comparison to the spatial resolution in the parallel direction of the detector due to the limited angle of the projection acquisitions. The low spatial resolution in the depth direction might reduce the sensitivity and specificity of DBT (Sechopoulos, 2013a). Moreover, two components of motion may limit the efficency of the technique: patient motion during the DBT acquisition may result in reduced sharpness in the reconstructed image, and continuous motion of the x-ray tube in some DBT systems results in blurring of the focal spot and lowers effective resolution. Strategies for motion prevention and compensation could provide high-quality images.

Regarding breast-CT, while it improves the visibility of the anatomical structures by providing 3D data without any overlaps, it pays the cost of an increased dose (Kalender et al., 2012; Sarno et al., 2015; O'Connell et al., 2010) and a loss in spatial resolution (Lindfors et al., 2008; O'Connell et al., 2010, 2014). Additionally, there are some limitations in breast coverage, such as including simultaneously medial and axillary elements of the breast during the scan and an adequate visualization of microcalcifications (Lindfors et al., 2008). Improved breast coverage can be potentially achieved through system design that might incorporate other breast components throughout the scan while using a novel table design, while the use of photo-counting detectors may improve the visualization of microcalcifications.

The limitations of conventional breast x-ray imaging call out for the development of tools and techniques that rely on other X-ray interactions to be able to increase the visibility of soft tissue components and breast cancers and that could potentially reduce false-negative cases that arise in the current conventional breast imaging techniques.

1.5 X-ray Phase Contrast imaging techniques

In order to increase the visibility and discernability between soft tissue components and breast cancers using digital technology that goes beyond the limitations of attenuation-based x-ray imaging, a more efficient x-ray-matter interaction mechanism must be considered. The behavior of X-rays traversing matter can also be interpreted as from an incoming X-ray wavefront, whose phase experience interactions, such as refraction, that cause a phase-shift in the X-ray wavefront. The experimental detection of these phase effects can be used for X-ray imaging using phase-sensitive techniques, such as propagation-based (PB) phase-contrast (PhC). Since PhC techniques are not intrinsically linked to X-ray attenuation in tissues, but rather to refraction, they have the potential to revolutionize X-ray imaging by removing its main limitation: poor image contrast due to low attenuation differences. X-ray phase contrast imaging applications have been proposed in a variety of fields, but medicine has consistently been considered the most important. This section explains the basic principles of image formation basis of PhC imaging technique, and the specific applications are described in a subsequent sections.

1.5.1 Refracting X-rays for medical imaging

To understand the phase-shift effects induced on X-rays traversing matter and to quantify how much the x-ray wave is affected when traversing a object, let's consider once again a parallel and monochromatic beam of wavelength λ (in cm) travelling in vacuum along the z axis. Let an object (made of a single material embedded into another homogeneous material) be impinged by an x-ray wave front as depicted schematically in 1.4. When X-rays pass through areas of varying optical density, such as when passing through a boundary surface between vacuum and solid or liquid matter, they are refracted.

Refraction can be described by the refractive index

$$n(x,y,z) = 1 - \delta + i\beta \tag{1.2}$$

where i is the imaginary unit, β the parameter linked to the absorption/attenuation properties of the medium, δ is responsible for the phase shift ϕ experienced by the X-ray wave
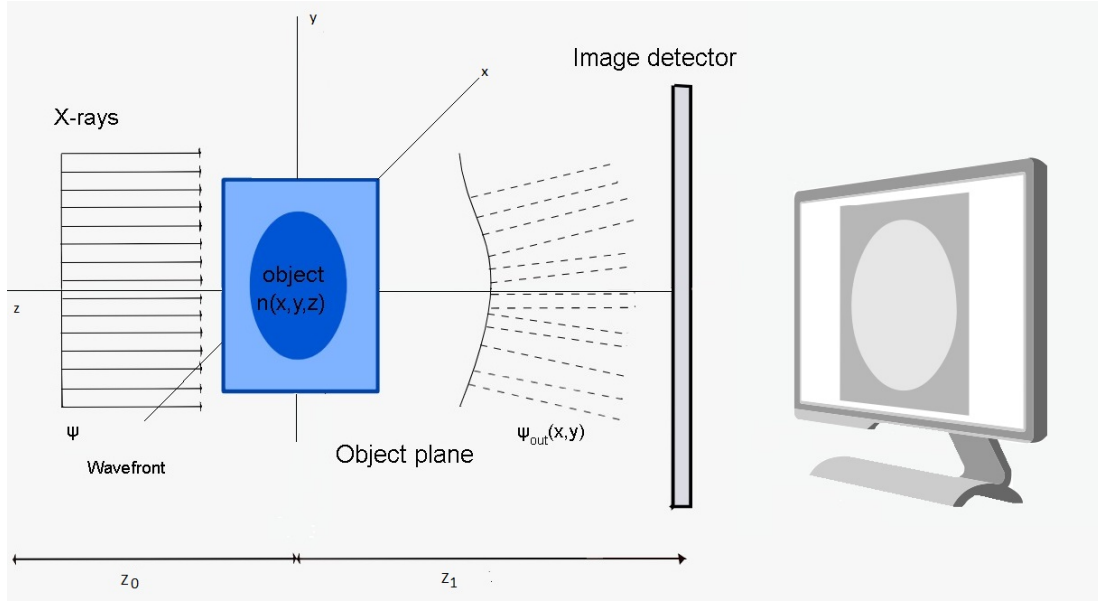
Figure 1.4: A schematic representation of x-ray wave interaction with an object, where ψ is a monochromatic plane wave with wave vector impinging on the sample, described by its refractive index distribution n(x, y,z). The wavefront emerging from the sample is $\psi_{out}(x,y)$. z0 and z1 are the source-to-sample and the sample-to-detector distances , respectively. Artwork by the author.

field when it transverses a given thickness of material. For X-rays with energies sufficiently higher than the absorption edges of the medium, δ and β can be expressed as functions of the electron density ρ (in g/cm^3) and the wavelength in the following expressions (Suortti and Thomlinson, 2003):

$$\delta \cong \rho_e \frac{r_e \lambda^2}{2\pi} \tag{1.3}$$

$$\beta = \mu \frac{\lambda}{4\pi} \tag{1.4}$$

where ρ_e is the classical electron radius. When the planar x-ray wave front traverses the object, as depicted in 1.4, the wave exiting the object plane is perturbed by the phase shift introduced by the object, and it will take at each point different directions. Therefore, the equation for refraction 1.2 can be described by a three-dimensional distribution of the refractive index as $n(x,y,z) = 1 - \delta(x,y,z) + i\beta(x,y,z)$. The exiting X-ray wave $\psi_{out}(x,y)$ at a given position in the object plane (x,y) is now the incident wave modulated by a complex transmission

factor $T(x,y)$ (Born and Wolf, 1999) described as:

$$\psi_{\text{out}}(x,y) = \psi T(x,y) = \psi_0 e^{ikz} T(x,y) \tag{1.5}$$

where $T(x,y)$ is function of the object refractive index distribution as

$$T(x,y) = e^{ik \int (n(x,y,z)-1)\,dz} = e^{-k \int \beta(x,y,z)\,dz} \, e^{-ik \int \delta(x,y,z)\,dz} \tag{1.6}$$

The latter equation implies that the object modulates the X-ray wave by reducing its amplitude, due to left term dependant on β as it accounts for the x-ray attenuation in a sample, which is equivalent to the Beer–Lambert law, given the relation 1.4. Alongside absorption, the introduced phase shift imparted by the object to the X-ray wave is then defined as:

$$\Phi(x,y) = -k \int \delta(x,y,z)\,dz \Phi(x,y) \cong -r_e \lambda \int \rho_e(x,y,z)\,dz \tag{1.7}$$

where 1.7 is obtained by recalling 1.3 and the integrals are performed along the entire length of the object along the z direction (Pelliccia and Morgan, 2018). The wave exiting the object plane is perturbed by the phase shift $\Phi(x,y)$ introduced by the object as a result of the interaction, and the wave will take different directions at each point. In other words, the wave leaving the object plane will deviate from the original direction z by a position-dependent refraction angle $\alpha(x,y)$ written as

$$\alpha(x,y) \simeq \frac{1}{k}\sqrt{\left(\frac{\partial}{\partial x}\Phi(x,y)\right)^2 + \left(\frac{\partial}{\partial x}\Phi(x,y)\right)^2} = \frac{1}{k}|\nabla_{xy}\Phi(x,y)| \tag{1.8}$$

where ∇_{xy} indicates the two-dimensional gradient operator in the object plane, yielding the two components of the refraction angle. Eqn (1.8) is the link between a detectable physical quantity, and eqn (1.7), the object-induced phase shift.

The refraction angle α induced by a biological sample is very small at x-ray energies typical of biomedical imaging (1–10 microradians) (Rigon, 2014). Because x-ray detectors are only sensitive to intensity, conventional x-ray imaging cannot detect the phase shift. First, the phase shift must first be converted into an intensity modulation in order to be used as an additional source of contrast in the x-ray image. Many phase-sensitive techniques then attempt to translate this refraction angle into intensity modulations on the detector, allowing these effects to be detected and interpreted. This can be accomplished, for example, by imaging with
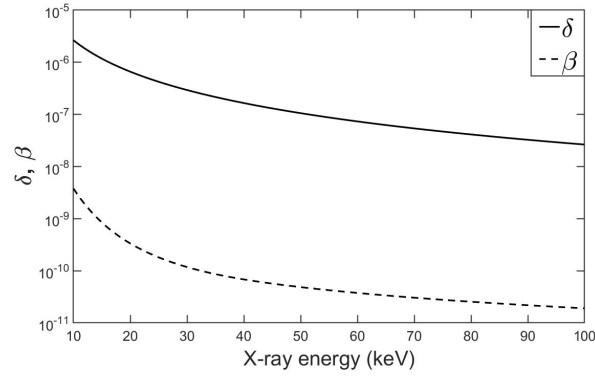
Figure 1.5: Values of δ and β for polymethyl methacrylate (PMMA), often used as a tissue equivalent material in phantoms, between 10 and 100 keV. The semi-logarithmic graph shows the large difference (2-3 orders of magnitude) between δ and β values, and their different dependence on X-ray energy. Image taken from (Brombal, 2020c).

coherent x-ray sources and revealing the contrast hidden in the phase shift term. Synchrotron radiation facilities are generally considered the gold standard for x-ray production thanks to their highly coherent x-ray sources.

Although the values of both δ and β are small, for soft tissues composed of light elements over the range of energies commonly used in X-ray imaging (greater than 10 keV) as it is shown in figure 1.5, the refractive index decrement δ is typically 1000 times larger than β (Rigon, 2014), therefore, playing a more important role in X-ray imaging Zhou and Brahme (2008). For example, at x-ray energies typical of mammography (15-25 keV), δ can be found in the range of $10^6 - 10^7$, while β is in the range of $10^8 - 10^10$ (Lewis, 2004; Zhou and Brahme, 2008). This means that, when used correctly, phase effects can result in a significant increase in image contrast (Olivo and Castelli, 2014; Rigon, 2014). Both parameters also show different dependencies with energy. β decreases approximately with $E^{-}4$ while δ approximately as $E^{-}6$ (Endrizzi, 2018; Zhou and Brahme, 2008). Summarized, the significant difference between δ and β is the reason why using phase-sensitive techniques can be advantageous over attenuation-based imaging.

Since PhC techniques are not intrinsically linked to X-ray attenuation in tissues, but rather to refraction, the radiation dose could potentially be reduced by using higher energy X-rays than are commonly used for attenuation contrast (Arfelli et al., 1998). As more energetic X-rays pass through the object without local energy deposition, this could be especially important for the development of novel X-ray imaging techniques with high contrast and low dose to patients (Zhou and Brahme, 2008). Further details on phase contrast imaging can be found

in the works by Bravin et al. (2012); Rigon (2014); Olivo and Castelli (2014); Pelliccia and Morgan (2018); Zhou and Brahme (2008).

This section outlined the general principles of PhC imaging on the basis that phase changes mechanisms can be exploited for medical imaging. Interferometry, analyzer-based imaging, grating-based imaging, edge illumination, and propagation- based techniques are some examples of the evolving x-ray phase-contrast imaging techniques that are mainly used with synchrotron radiation and, in some cases, conventional sources (Wilkins et al., 2014; Olivo and Castelli, 2014; Rigon, 2014; Bravin et al., 2012). In the next section, just one approach will be discussed, propagation-based PhC imaging technique, as it was the chosen modality to carry out the different experimental studies presented in this thesis due to its forward experimental set-ups.

1.5.2 Propagation-based phase-contrast technique

PB PhC imaging (also known as PPCI, in-line holography or free-space-propagation imaging) is the simplest non-interferometric phase-sensitive technique to implement, as phase effects can be observed without the use of any additional optical elements or multiple exposures. An interference pattern is formed when an x-ray wave passes through a refractive object in the *xy* plane, as it can be recalled in figure 1.4. The interference angle is so small, as stated in the previous section, that placing the detector directly behind the sample ($z_1 = 0$), as is typically performed in conventional radiology, makes it impossible to detect the interference patterns and only absorption contrast is obtained. Therefore, the detector is placed at a large sample-to-detector distance z_1 rather than directly in contact, to allow a phase-contrast image to be formed.

In terms of X-ray source characteristics, PB has stringent requirements, calling for high spatial coherence and a high detector spatial resolution. Synchrotron radiation (SR) facilities are widely regarded as the gold standard for X-ray production due to their highly coherent X-ray sources and high photon fluxes over a wide energy range, making them ideal sources for PB PhC imaging. The source size is on the order of a few hundred micrometers, and the emitted radiation is highly collimated, therefore, a very high degree of spatial coherence can be provided (Margaritondo, 1988). When such source is used for PB imaging techniques, by increasing z_1 in fig. 1.4, the perturbed wavefront is left to propagate freely in space, resulting in the formation of a phase-contrast image, proportional to the Laplacian of the phase shift. Phase contrast increases linearly with the propagation distance, as a result, strong interference
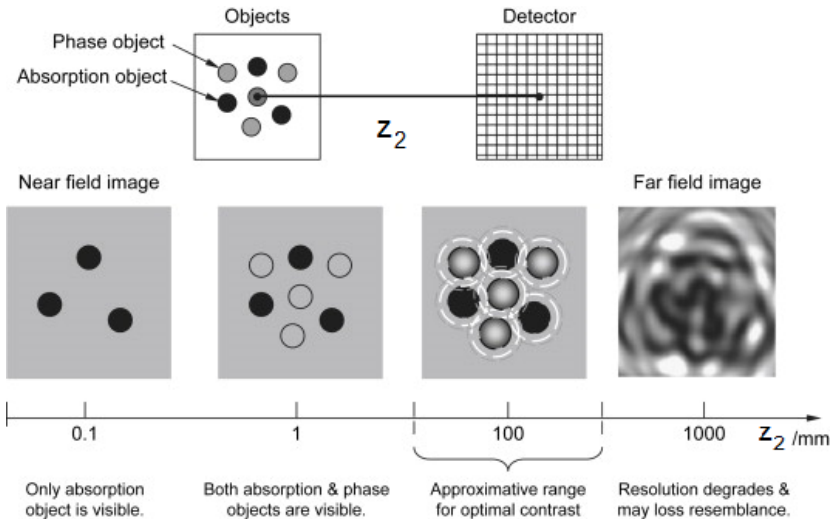
Figure 1.6: Dependence of in-line phase-contrast images on the distance between object and detector. The numerical data for z_2 are given for illustration purposes only as, in practice, it will depend on the specific system set-up. Illustration from (Zhou and Brahme, 2008).

patterns in the intensity are detected along the edges of the imaged object's details (Spanne et al., 1999). The phase-contrast image profile contains a typical profile with positive and negative peaks corresponding to such edges. The sharp interfaces of the refractive object, where the phase shift changes abruptly, provides a strong edge enhancement that can boost the identification of structures, especially when the absorption contrast alone is not sufficient. This edge enhancement effect, the most typical PB effect sought after in medical imaging, is consequent from the phase shift $\Phi(x,y)$ described in eqn. (1.7). Thin and small details that are normally invisible on absorption images will become detectable (Arfelli et al., 2000). In forming phase-contrast images, the required free space or propagation distance z_1 plays an important role and it needs to be optimized to maximize phase-contrast signal according to the detector spatial resolution and the experiment set-up. Figure 1.6 depicts how different details become detectable and how image contrast can vary depending on the propagation distance. An extended mathematical description on how the contrast is formed on the detector when using PB is found in Brombal (2020c).

1.5.3   The SYRMEP Beamline

The SYnchrotron Radiation for MEdical Physics (SYRMEP) beamline at the Italian synchrotron facility Elettra (Trieste) was established as a medical beamline dedicated to the imaging of biological and biomedical samples, foreseeing "in vivo" mammographic examinations. Elettra is a third generation synchrotron, that circulates electrons with energies of either 2.0
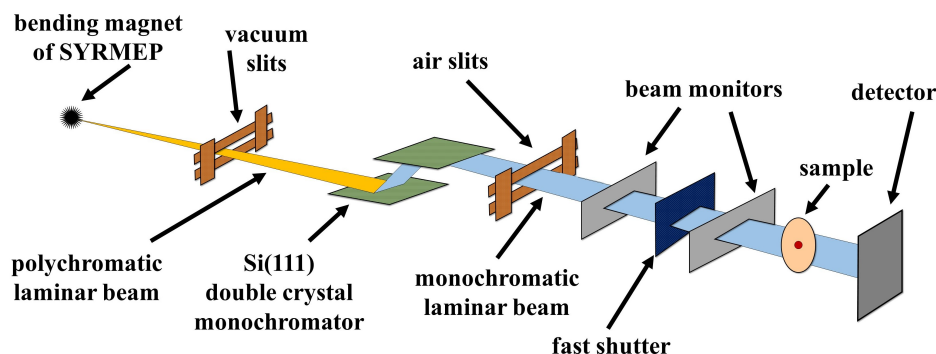
Figure 1.7: A schematic layout of the SYRMEP beamline, from the X-ray production by the bending magnet (left) to the sample and detector stages (right) as it appears in Brombal (2020a). Some additional elements present such as anti-scattering grids, are not reported in figure.

or 2.4 GeV in a 260-meters-long storage ring. Synchrotron radiation is collected from the accelerated electrons using a variety of insertion devices (bending magnets, ondulators, and wigglers), feeding 28 experimental beamlines that are tangentially positioned in relation to the storage ring. Each beamline is dedicated to a different technique, therefore, Elettra users have a wide range of possibilities to examine their samples, including spectroscopy, spectro-microscopy, diffraction, scattering, and lithography to name a few. The X-ray source from the beamlines is extremely stable as a result of the top-up operating mode of the synchrotron through frequent electron injections, thus compensating for the natural ring current decay and keeping the ring current constant (Dullin et al., 2021). SYRMEP bealine can be operated in a monochromatic or polychromatic (white) mode using the entire energy spectrum (from 10 to 50 keV). Two evaluating stations are available at the SYRMEP beamline, the experimental station for investigating small samples and small animals and the radiological station for patient applications. In view of the experimentation with patients on the clinical mammography system, the SYRMEP beamline has been modified from the original experiments that started in 1996 to comply with all the required safety regulations to operate in the radiological station with patients, with a dedicated mobile patient support, and a room for radiologists and radiographers. A description of the original beamline and the subsequent modifications can be found in Arfelli et al. (1998, 2000); Abrami et al. (2005); Arfelli et al. (2007); Tromba et al. (2010) and, more recently, in Dullin et al. (2021).

The overview of the current beamline is shown in Fig 1.7 as followed: the radiation source is one of the bending magnets of the Elettra storage ring, that provides a polychromatic (white) beam which is highly collimated (laminar) in the vertical direction (divergence of the order of 10^{-4} rad). A couple of orthogonal tungsten vacuum slits determine the cross section (horizontal

acceptance of 7 mrad) of the x-ray beam impinging on the sample. The beam can be optionally monochromatized by means of a double Si(1,1,1) crystal working in Bragg configuration, to tune the beam energy in the range 8 - 40 keV, with an effective energy resolution of $\Delta E/E = 2 \times 10^{-3}$. The monochromator insertion is automatized, allowing the user to switch from white to monochromatic beam configurations in a more convenient manner, taking just a few minutes. The available monochromatic flux is heavily influenced by the chosen energy and synchrotron operation mode. Another set of tungsten slits adjusts the monochromatic beam before reaching the air ionization chambers (beam monitors) that are simultaneously read. In the event of a discrepancy between the readings of the two ionization chambers, the beam is quickly stopped by a fast shutter system that operates in 15 ms (Longo et al., 2007). Finally, the beam reaches the sample and, after placing a defined propagation distance according to the experiment set-up, it reaches the detector. At 32 keV, this arrangement produces a laminar beam with a useful cross section of about 220 (horizontal)$\times$3.5 mm^2 (vertical, Gaussian shape, FWHM) and a source distance of 30 m, where the patient support is located. SYRMEP beamline was the site of all experimental PB PhC breast imaging studies described in this thesis, making use of both, the experimental and radiological stations.

1.5.4   Clinical mammography trials

Technological advancements have led to potential medical applications of phase-contrast X-ray imaging techniques for imaging techniques that challenge traditional X-ray imaging methods such as mammography and angiography (which visualizes blood vessels and their associated structures). Breast imaging has been on of the main interesting case studies for PB PhC at SYRMEP beamline, as "in vivo" mammographic examinations were forseen ever since the creation of the beamline in 1996. Only two clinical mammographic studies employing phase-contrast techniques have been carried out far due to the strict requirements on the source coherence of phase-contrast techniques and the typical constraints of the low radiation dose for breast imaging. Both studies take advantage of the PB configuration with quite different results.

The first investigation is based on traditional X-ray tubes (Tanaka et al., 2005), and it was discovered that the disadvantages of the conventional X-ray system outweighed the benefits of the phase contrast technique. No statistically significant difference in memory rates and cancer detection rates was discovered after a clinical trial involving 3835 exams when compared to traditional film-screening mammography (Morita et al., 2008). On the contrary, the mammographic examinations at the SYRMEP beamline (Castelli et al., 2007) were carried out using

an SR X-ray beam in the energy range 8-35 keV with a photon flux of about 10^8 $ph/(mm^2 s)$ and dimensions of 21 cm x 3.5 mm at the compressed breast. The images were obtained by scanning the patient in prone position in front of the stationary laminar beam for approximately 10 seconds. The patient support can be rotated in the horizontal plane to acquire the two views of the mammographic exam. As a detector, a screen-film system was placed at approximately 2 meters from the breast. It is important to point out that the source is fixed in the geometrical setup of SR mammography while the breast and the screen-film detector are simultaneously scanned in the vertical direction, whereas in conventional clinical mammography, the compressed breast and detector are fixed and the screen-film cassette is practically in contact with the breast. Breast thickness and glandularity, as in conventional mammography, determined the optimal beam energy for each examination. The quality of the resulting *in vivo* images matched the quality of previous *in vitro* SR mammography studies (Arfelli et al., 1998). Furthermore, the diagnostic quality of the SR radiological images was higher than that of conventional mammography images, without increasing the patient's delivered dose.

The preliminary experience of mammography with synchrotron radiation (MSR) that produced high-quality images of the breast in both, surgical breast specimens and humans, served to clinically validate its imaging protocol. Moreover, it helped to determine the needs to optimize the quality of radiological examinations towards using a digital detection system and later to breast tomography. The MSR trial that encompassed more than 70 patients (Castelli et al., 2011; Longo et al., 2014) proved the potential for an increased ability of mammography with synchrotron radiation to diagnose true-negative imaging findings by evaluating the diagnostic images in patients with questionable or suspicious breast abnormalities identified at combined DM and US. The image quality of MSR was investigated by allowing two experienced radiologists, specialized in mammography, to assess the visibility of breast abnormalities and of breast glandular structures, by comparing and grading the DM images and MSR images. An example of the difference in image quality between conventional and SR PhC mammography is shown in fig. 1.8.

A targeted strategy is required in order to confront the limitations in sensitivity in conventional DM, and reduce the significant number of false positives in adjunctive screening/diagnostic examinations that are performed after an initial mammography. The results from the clinical PB PhC mammography study suggest that the methodology could be used to clarify cases of questionable or suspicious breast abnormalities identified at previous digital mammog-
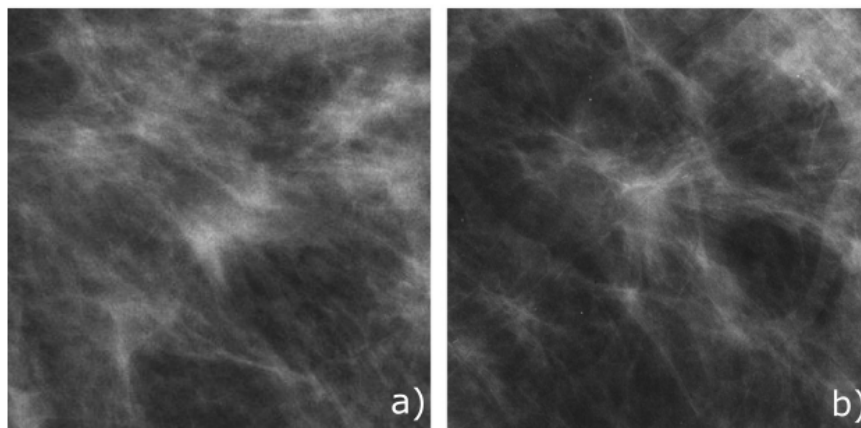
Figure 1.8: Images of left breast in 62-year-old woman with suspicious mass identified at DM. (a) A digital zoom of the mediolateral oblique DM image showing a suspicious mass with speculated margins (BI-RADS category 4) in retroareolar region. (b) Corresponding digital zoom of the synchrotron radiation mammographic image confirming and better depicting the spiculated mass (BI-RADS category 5). Reproduced from Castelli et al. (2011).

raphy exams. The images demonstrated that PhC mammography depicts normal structures and abnormal findings with higher image quality than with conventional mammography (Longo et al., 2014), lower dose, and greater diagnostic power with respect to digital mammography (Fedon et al., 2018a). The latter compared and assessed the MGD and entrance surface air kerma (ESAK) of SR PhC mammography to DM. Using a monoenergetic beam resulted in a significant reduction in MGD by 43% on average and ESAK was reduced by more than 50%. These results are obtained using energy selection and exposure optimized for screen-film system. Additionally, the diagnostic performance was evaluated in this study by using receiver operating characteristic curves to compare the area under the curve (AUC). Two on-site radiologists rated the images in accordance with the BIRADS assessment categories, which were after statistically correlated with the final diagnoses using generalized linear models (GLMs). AUC analysis confirmed that for SR PhC mammography, GLM had a higher diagnostic accuracy, particularly in terms of specificity. Altogether, the use of synchrotron radiation with the phase-contrast technique for mammography resulted in a significant dose reduction and higher diagnostic accuracy when compared to DM.

These findings have encouraged more research into the dose reduction of the clinical application of x-ray phase-contrast breast imaging using digital detectors and higher energy beams, which would allow the introduction of breast CT. With 3D imaging of the breast being the frontier of the breast imaging in the clinical practice, a new collaboration called SYRMA-3D (Synchrotron Radiation Mammography-3D) involving the INFN (Italian Institute of Nuclear

Physics), Elettra Laboratory and the University Hospital of Trieste was created aiming at overcome the limitations of planar techniques with the development of a 3D mammographic system using PB PhC techniques in conjunction with CT using monochromatic radiation, which will be the main topic of chapters 3 and 4.

1.5.5 Additional synchrotron medical applications

In virtue of the inherent limitations of conventional attenuation-based contrast radiology, certain diseases may only be detected in an advanced stage. As a result, other medical applications can benefit from using phase-contrast x-ray imaging techniques to detect early stages of disease, such as degenerative joint disease or osteoarthritis. It is now possible to visualize cartilage, detect early degenerative changes, and visualize better contrast and spatial resolution of trabecular bone, small fractures, bone-marrow tissue, and cartilage using phase-contrast X-ray imaging (Mori et al., 2002). By means of the excellent contrast for soft tissue imaging that PhC imaging techniques offer, phase shift X-ray interferometry can be used for coronary angiography to produce detailed high-resolution images of the blood vessels (Takeda et al., 2002), although contrast agents may still be required. Another advantage for detecting disease at an early stage can be used for lung diseases. A lung x-ray radiograph can appear completely normal in advanced stages of some lung diseases, such as interstitial lung disease. It is possible to make use of the phase-contrast imaging techniques to image lungs, due to the air–tissue interfaces, and show the hidden disease. Along with breast imaging, phase-contrast application to lung imaging has been attracting an increasing interest (Kitchen et al., 2005; Lewis et al., 2005; Kitchen et al., 2017), and encouraging results on human-scale samples have recently appeared in the scientific literature (Wagner et al., 2018). Aside from phase-contrast imaging, the K-edge subtraction technique can be used in angiography and/or lung imaging, and it has been one of the most extensively researched medical applications of synchrotron over the years at various facilities around the world, including the Stanford Synchrotron Radiation Laboratory (SSRL), the National Synchrotron Light Source (NSLS), the Hamburg Synchrotronstrahlungslabor (HASYLAB), the Photon Factory (PF), the Budker Institute of Nuclear Physics, and the European Synchrotron Radiation Facility (ESRF) (Thomlinson et al., 2018). The works of Suortti and Thomlinson (2003); Bravin et al. (2012); Brahme (2014) provide an in-depth examination of synchrotron imaging applications such as bronchography and x-ray microscopy, imaging by scattering and therapy applications such as microbeam radiation therapy. A discussion on the investigations and development of innovative techniques for medical

imaging in the dedicated SYRMEP beamline can be found in Abrami et al. (2005) and a more recent review on multiscale biomedical imaging at the Elettra is available from Dullin et al. (2021).

1.6 Closing remarks

Clinical judgement and interdisciplinary cooperation are necessary to promote the best outcome for the patient. This can be achieved by understanding the characteristics of breast cancer and important features at multiple spatial and/or temporal scales with an integrated collaboration involving different health professionals, such as oncologists, surgeons, nurses, pathologists, radiologists and medical physicists. The descriptions made in this chapter show the critical role that breast imaging plays in the diagnosis of breast cancer and in the direction of treatment decisions. It has also discussed the challenges and limitations that constrain attenuation-based x-ray imaging modalities, and the high patient dose requirements that makes of breast imaging one of the most challenging medical imaging techniques to achieve.

One way to overcome these problems is with implementing phase-contrast imaging techniques with synchrotron radiation, that can offer great advantages over conventional X-ray imaging but, at the same time, have specific requirements to attain high-quality images. The desire to boost image quality using a dedicated breast imaging system that offers entirely three-dimensional images, free of tissue overlap, enhanced for soft tissue contrast and without the need of breast compression, has led to the development of dedicated breast CT systems using monochromatic synchrotron radiation at the Italian and Australian synchrotron facilities. In this context, I have contributed to experimental investigations during the doctoral studies that address some of the challenges of breast imaging, such as optimizing the PhC bCT acquisition, processing and tomographic reconstruction techniques, as well as working on strategies for patient motion prevention and compensation, which are presented in the next chapters of the thesis. I also carried out a Monte Carlo simulation dose study that emphasizes on the importance of properly quantifying the absorbed dose to the breast during x-ray examinations to better understand the radiation-associated risk derived from the imaging practices, which is discussed in the next chapter.

Finally, PB PhC imaging approach employing a polychromatic synchrotron beam by using a different imaging equipment is discussed in the next two chapters. This technique has the potential to help with the evaluation of breast lesions at a micrometer resolution. The experimental results that are provided in these chapters demonstrate the benefits of PB PhC imaging

for diagnostic purposes. The multiscale PB PhC tomography approach for breast imaging is presented in this thesis as a possible solution than can offer high-resolution and overall high-quality images which could be applied in a clinical environment for the multidisciplinary fight against breast cancer.

Chapter 2

Dosimetry in x-ray breast imaging

Large published literature has demonstrated the value of mammography screening for the early diagnosis of breast cancer, as introduced in ch. 1. Medical physicists follow international protocols to ensure that the mammographic equipment in a diagnostic facility provides high-quality mammograms at the lowest exposure to patients and personnel. These protocols highlight the importance of dose assessment, low-contrast detection, spatial resolution and noise. It is essential to quantify the absorbed dose to the breast during x-ray based imaging using the MGD in order to fully understand the radiation-associated risk from breast x-ray imaging exams, as recommended by the International Commission of Radiological Protection (ICRP) and the International Commission on Radiation Units an Measurements (ICRU). The estimation accuracy of MGD is directly related to risk calculation and it is also necessary for quality control methods for breast imaging systems. However, direct measurements of MGD are not feasible, therefore, conversion factors that relate incident air kerma to the average dose absorbed by glandular tissue are achievable through Monte Carlo (MC) calculations (Wu et al., 1994; Dance et al., 2000). This chapter includes a review of the fundamentals of breast dosimetry using the currently employed homogeneous breast models with their limitations, with a discussion on the issue that the present models tend to overestimate patient breast dose (Dance et al., 2005a; Sechopoulos et al., 2012). This has served as motivation for many researchers to work on a proposal of developing a new breast model that could overcome the drawbacks of the homogeneous models currently in use. This is one of the main goals of Task Group No. 282 (TG-282) of the American Association of Physicist in Medicine (AAPM, 2022) and the European Federation of Organization for Medical Physics (EFOMP), that is working towards the development of a new universal dosimetry protocol. This chapter includes the developments of a study that was carried out within the framework of TG-282, where I performed Monte

Carlo simulations to estimate the MGD on computational models with different fibroglandular tissue distributions. I presented the results of the the study discussed in this chapter, in the 15th International Workshop on Breast Imaging (IWBI2020). The proceedings publication can be found in Arana Peña et al. (2020).

2.1   Current breast dosimetry models
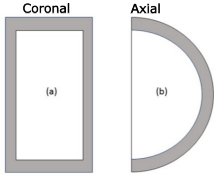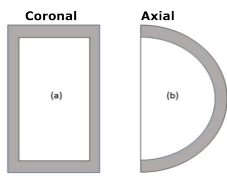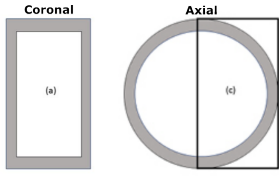
As radiation interacts with atoms of the material, its energy is imparted while causing a physical or chemical change in the material properties, many of which are proportional to the absorbed dose, such as the biological effects. Therefore, it is critical to understand the magnitude of risk associated with the radiation dose delivered in mammography. The Biological Effects of Ionizing Radiation (BEIR) VII report (National Research Council, 2006) critically examined data on doses and increased cancer incidence from several studied groups and allowed development of a radiation risk model for breast cancer. Their studies have shown that a complete mammography imaging induces approximately 1–3 mGy dose into the breast tissue itself, which can increase the risk of cancer in the individual. Since its proposal by Hammerstein et al. (1979), the estimation of the mean glandular dose (also known as the average glandular dose, AGD) has been the basis of international breast dosimetry protocols, initially formulated for mammography. The different approaches use conversion factors that are based on different simple geometrical models that simulate the shape of the breast under compression proposed by Dance (1990); Dance et al. (2000) and Wu et al. (1991, 1994), with the MGD as the worldwide recognized quantity for determining the dose delivered to the breast. The different formalisms of MGD for conventional mammography can be expressed in a general expression:

$$D = AK \cdot CF \tag{2.1}$$

where AK is the measured incident air kerma (mGy) and CF are the appropriate conversion factors or coefficients (mGy/mGy), that depend on the geometrical setup and breast anatomy, according to the formalism used. The conversion factors were obtained using MC simulations and are affected by breast anatomy, scanner geometry, and X-ray spectra characteristics. The current models for breast dosimetry assume an internal breast volume composed of a uniform mixture of fibroglandular and adipose tissue, that is homogeneously distributed throughout the breast parenchyma, with an outer layer of skin or adipose tissue.

Table 2.1 compares the basic principles of the different breast models used in breast

dosimetry to present day. The formalism proposed by Dance (1990) is used generally in Europe with the protocols of IAEA and EUREF, while the formalism by Wu et al. (1991) is used mainly in the United States with the ACR protocol. Both models emulate the shape of letter "D" of a compressed breast. On the contrary, the model by Boone (1999) uses a complete cylindric breast shape instead of a semicircular D-shaped breast shape, like the other two models. The latter was used to investigate breast CT imaging assuming that the MGD of the uncompressed pendant breast is similar to that of the compressed breast, but compressed and uncompressed breast shapes in a pendant geometry differ, which could lead to different dosimetry.

	Dance (1990)	**Wu et. al (1991)**	**Boone (1999)**
Composition glandularity	50%/50%	0%, 100%, 50%/50%	0%, 100%, 50%/50%
Outer layer	Adipose tissue 5 mm	Skin 4 mm	Skin 4 - 5 mm
Thickness (mm)	20 - 110	30 - 80	20 - 80
Cross section	Semi-circular	Semi-elliptical	Circular

Table 2.1: Comparison of the currently used geometrical models for breast dosimetry. In the Boone model, only half of the cylinder is irradiated (denoted by the black line) while the other half serves to model the chest wall. Cross section figures from Dance and Sechopoulos (2016b)

Although estimating the MGD for patient exposures is critical, estimating the MGD using test objects (phantoms) simulating the breast under standard image acquisition conditions also ensures the safe use of the breast imaging unit. The measurements performed by a medical physicist using breast-simulating test phantoms, are extremely useful for quality control (QC) and inter-system comparison (Dance and Sechopoulos, 2016b; Pernicka and McLean, 2007; Perry et al., 2008; Berns et al., 2016).

2.1.1 Limitations

Since current dosimetry models assume a homogeneous mixture of fibroglandular and adipose tissue, they ignore the heterogeneous distribution of such tissues in the breast. The position of the glandular tissue within the breast has a strong influence on MGD, specially in the vertical

direction, between the x-ray source and the detector (Boone, 1999). Boone investigated the impact of vertical location, discovering that varying the vertical position of a slab of 5 mm of glandular tissue inside an adipose breast model can result in a variation in MGD of up to 84%. Other numerous studies (Boone, 2002; Sechopoulos et al., 2007; Dance et al., 2010) using mammography and DBT have investigated the dependence of the mean glandular dose with other parameters, such as breast size, thickness, and glandular fractions. Dance et al. (2005b) used an anthropomorphic breast phantom to compare conversion coefficients for breast glandularity, observing a breast dose overestimation of 10%-43% due the uniformity of the homogeneous model of breasts.

Thanks to the development of bCT, which allows for a true three-dimensional depiction of breast anatomy as mentioned in 1.3.4, it has been possible to comprehensively assess the inner structure of the breast, hence, the distribution of glandular tissue in patient's breasts has been better understood. The work by Sechopoulos et al. (2012) confirmed the previous findings of Dance et al. (2005a) pointing to a ~30% overestimation of the normalized glandular dose in mammography when the homogeneous tissue mixture approximation to an heterogeneous tissue distribution. Hernandez et al. (2015) used bCT data to characterize the statistical distribution of glandular tissue in the breast and investigate the effect of bCT-derived heterogeneous glandular distributions on dosimetry in mammography. It was concluded that a homogeneous distribution does indeed overestimate the amount of glandular tissue near the entrant surface of the breast, resulting in a 30% excess dose than with an heterogeneous compressed breast model.

The investigation of patient specific breast models based has been addressed by different studies (Boone, 2002; Huang et al., 2011; Wang et al., 2017; Baneva et al., 2017; Fedon et al., 2018b, 2021) confirming that using a simplified homogeneous breast model neglects the large variability in the glandular tissue texture. Moreover, dose estimates on homogeneous distributions are larger than those on patient specific structured models derived from clinical bCT scans Sarno et al. (2018); Hernandez et al. (2019).

2.2   Monte Carlo dose evaluation study

As mentioned previously in this chapter, direct measurements of MGD are not feasible and appropriate conversion factors (CF) obtained through Monte Carlo calculations can relate the measured quantity (IAK) to the immeasurable organ dose (MGD) as in eq. 2.1. As CF are estimated through a computational tool, it allows to model a large variety of scenarios using

computational phantoms in radiation imaging. Taking into account the limitation that current dosimetry models assume a homogenous mixture of breast tissue and the versatility of MC modelling, a study to estimate the MGD on computational models with different fibroglandular tissue distributions was carried out, where I performed MC simulations and the following dose calculations. This MC study follows the methodology of a previous MC study (Fedon et al., 2019) on the optimal breast voxel resolution for dosimetry in digital breast tomosynthesis. The study design is summarized in Figure 2.1. Specific details related to each step are provided in the next paragraphs.
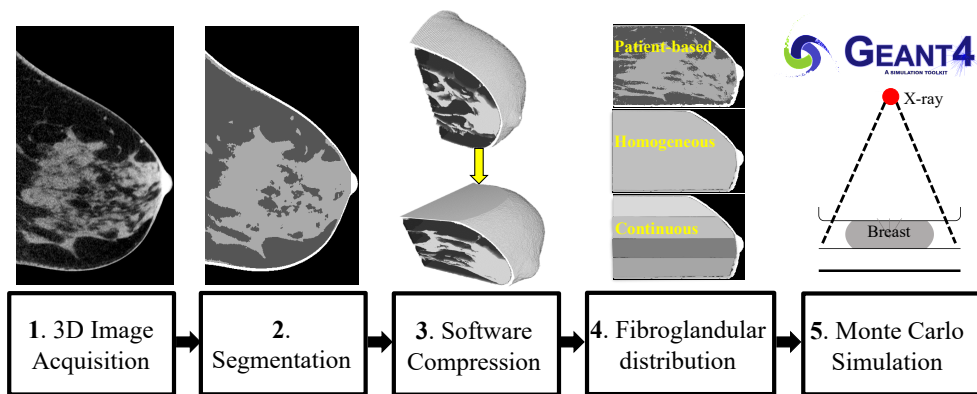
Figure 2.1: Flowchart of the methodology to estimate the mean glandular dose on the different fibroglandular tissue distributions of the compressed breast models.

2.2.1 Methodology

2.2.1.1 3D Image Acquisition

The computational phantoms were developed from realistic breast shapes from real bCT data that underwent a simulated mechanical compression to be able to simulate standard mammography conditions. Three models with different fibroglandular tissue distributions were derived from the bCT data: a patient-derived fibroglandular tissue distribution model, a homogeneous mixture model (currently used model) and a novel heterogeneous model, obtained using probability functions. In this investigation, ninety 3D-bCT images were acquired from 90 patients as part of an ongoing ethics board-approved study. Informed consent to use the images for further research was obtained from all patients. All bCT images were acquired using a dedicated bCT clinical prototype (Koning Corp., West Henrietta, NY) installed at Radboud University Medical Centre (Nijmegen, The Netherlands). The system is equipped with a flat panel digital x-ray detector (4030CB, Varian Medical Systems, Palo Alto, CA). 300 projections of an

uncompressed breast were acquired over a range of 360° , using a W/Al spectrum at a fixed voltage of 49 kV and at a suitable tube current automatically set for each patient. The images were reconstructed using filtered back projection (FBP), with isotropic cubic voxels of 0.273 mm in size. Further details on the optimization of the voxel size for breast dose estimation can be found in Fedon et al. (2019).

2.2.1.2   Segmentation

The reconstructed patient bCT images were automatically classified into all major tissue types within the breast using an automatic algorithm developed by Caballo et al. (2018a). The proposed algorithm identified and segmented the voxels, slice-by-slice, with no prior training or threshold setting, into four categories: air, skin, adipose, and fibroglandular tissue. The total mass of glandular and adipose tissue included in the bCT images for each patient was calculated by counting the number of voxels classified as glandular and adipose tissue, and multiplying them by the given voxel size and tissue density. The breast glandularity (g), defined as the ratio between the mass of fibroglandular tissue and the total breast mass (without the skin), was calculated for each patient according to Fedon et al. (2019) as:

$$g = \frac{n_g \cdot \rho_g}{(n_g \cdot \rho_g + n_a \cdot \rho_a)} \tag{2.2}$$

where n_g and n_a are the number of voxels classified as fibroglandular and adipose tissue respectively, ρ_g and ρ_a are the corresponding densities for fibroglandular tissue and adipose tissue (0.93 and 1.04 g/cm^3 Hammerstein et al. (1979)).

2.2.1.3   Software compression

Classified bCT images were converted into a finite element biomechanical model in order to simulate the mechanical breast compression in the CC projection experienced during the mammographic procedure. The breast models were compressed between two rigid planes corresponding to the compression paddle and breast support. The compression was performed using the open source package NiftySim (Johnsen et al., 2015). Different elastic properties (e.g. Young's modulus) were applied to adipose, glandular and skin tissue, as described by Wellman (1999). For each classified bCT image, the corresponding CC mammographic view was also available. In this way, each simulated compressed breast thickness matched the real thickness of the mamographic CC view of that breast (recorded in the DICOM header). This work

considered only the CC projection, thus, not accounting for possible differences in the MLO field of view. More details on using realistic compressed breast phantoms for medical physics applications is found in the work by García et al. (2020).
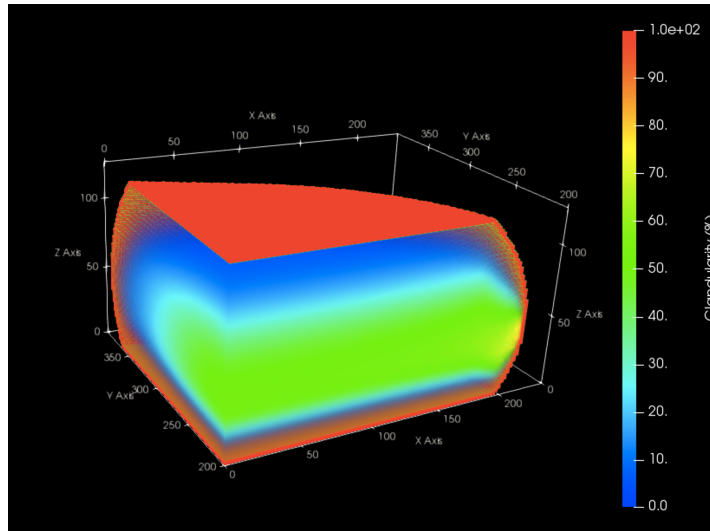
Figure 2.2: This image shows a central section cut of one of the patient's compressed breasts. The color gradient in image represents the glandularity percentage. It is observed that the glandular tissue is not equally distributed, with the highest density being located below the centerline of the breast, towards the nipple (bright colors). Original image.

2.2.2 Fibroglandular tissue distributions

2.2.2.1 Patient-based distribution

The input volumes were the ninety segmented compressed breasts, that reflected the real fibroglandular tissue distribution from patients. This model was considered as the gold standard. Figure 2.3 a) shows how the fibroglandular tissue (in light grey) is distributed heterogeneously along the breast on an adipose tissue background. The adipose tissue voxels, were considered with a glandularity $g = 0$. In order to provide an objective dosimetric evaluation of the computational models during typical mammographic examinations, the shapes of the patient-based phantoms and the skin thickness were used to generate the other two versions of the fibroglandular tissue distributions phantoms.

2.2.2.2 Homogeneous distribution

The breast tissue voxels that were previously labeled as either fibroglandular or adipose tissue were replaced with voxels containing a mixture of both materials with the corresponding original patient glandularity, evaluated with eq. 2.2. This homogeneous distribution , as seen in figure 2.3 b) is the currently used model, where it assumes fibroblandular tissue, that takes in

radiation dose, in positions where usually adipose tissue is found. A preliminary visual comparison between images 2.3 a) and b) suggest that this model estimates a high absorbed dose (high glandularity) in regions where the glandularity is, in fact, low.

2.2.2.3 Novel continuous (heterogeneous) distribution

The voxels in the proposed heterogeneous model were filled with an adipose/fibroglandular tissue mixture according to three continuous probability functions, g_x, g_y and g_z, to match patient's heterogenous model. Figure 2.3 c) depicts a grey color-gradient that matches the glandularity probability functions $g = g_x, y, z$ in the three planes.
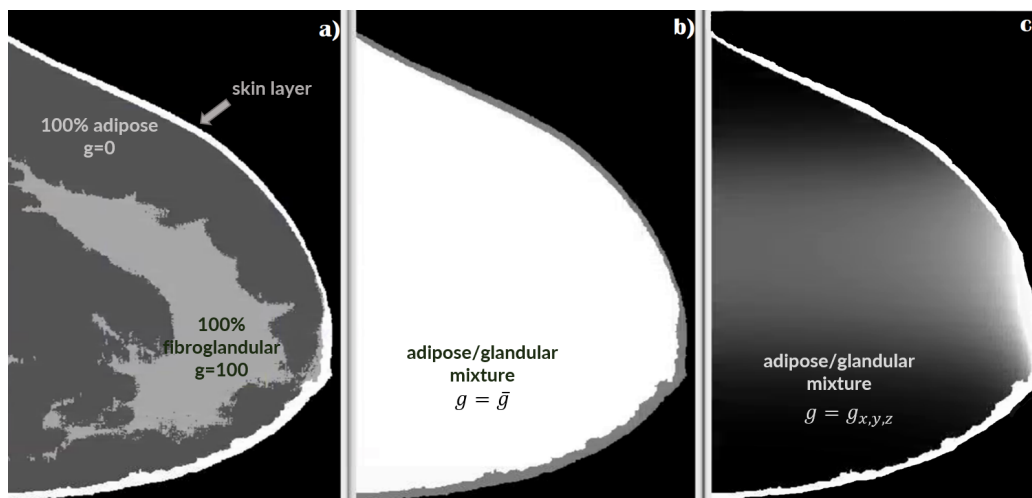
Figure 2.3: The three types of computational phantoms with their corresponding fibroglandular distributions. a) The patient-based distribution: original fibroglandular tissue distribution obtained from the segmented bCT. There is a clear distinction between voxels of 100% adipose and 100% glandular tissue.b) Homogeneous distribution: a mixture of adipose and fibroglandular tissue, where all voxels have the same glandularity that matches the original patient glandularity. c) Novel continuous distribution: each voxel has a different glandularity, according to 3 probability functions gx, gy, gz to match the patients' heterogeneous pattern. For visualization purposes, the models are uncompressed. Original image.

Each resulting compressed breast volume was divided into 70 regions in each of the three orthogonal directions (i.e., axial, coronal, and sagittal as seen in the blue insets of 2.4) to derive the three continuous distribution of fibroglandular tissue in the breast along the anatomical planes, i.e. coronal, (gx) axial (gy), and sagittal (gz). The relative glandular fraction (i.e., the ratio of the number of glandular voxels in a sub-region of the breast volume to the total number of voxels in that specific sub-region) from each of the 90 classified-compressed bCT volumes was evaluated as proposed by Fedon et al. (2018c). The median, 25th, and 75th percentiles were calculated in each sub-region.
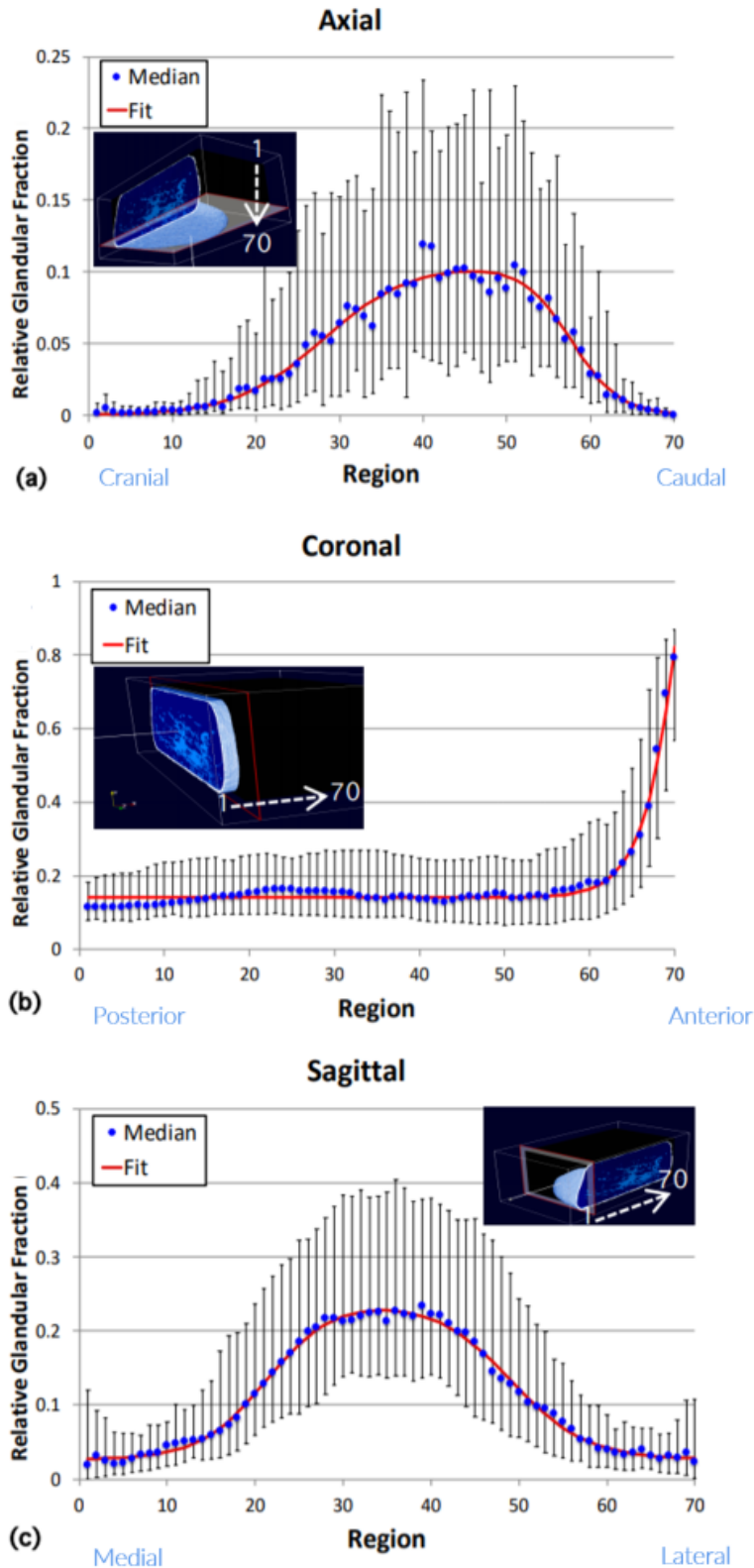
Figure 2.4: Relative glandular fractions for (a) axial, (b) coronal and (c) sagittal view. The glandular tissue is not equally distributed, mainly in the axial and coronal planes. In each graph the blue dots represent the median value, the bars represent the 25th and 75th percentile and the red line the fit to the distribution. The insets show the orientation of the 70 slices in each view.

The fibroglandular distribution in the breast data set was determined using the best-fitting function for the median distribution in each orthogonal direction. In all the three sets the thickness of the outer skin layer was kept unchanged. Figure 2.4 shows the relative glandular fractions for (a) axial, (b) coronal and (c) sagittal anatomical planes. The fibroglandular tissue distribution tends to be concentrated in the caudal direction of the breast, meaning towards the bottom of the breast, in the axial plane. On the coronal view the distribution is drawn towards the anterior directions, towards the nipple. Lastly, in the sagittal plane, a medial-lateral symmetry is observed.

2.2.3 Monte Carlo simulations

Once the compressed breast models derived from the three fibroglandular tissue distributions were ready, I modified the previously experimentally validated MC code (Fedon et al., 2019) for breast dosimetry, based on the Geant4 toolkit (Agostinelli et al., 2003) (release 10.05, December 2018) to match the characteristics of mammography system, Mammomat Inspiration (Siemens Healthcare, Forcheim, Germany), located At Radboud University Medical Centre in Nijmgen, The Netherlands. I carried out the customized MC simulations (90 patients, 3 models each) conforming to the technique used for each patient's real mammogram, resulting from the breast compressed thickness, as seen in table 2.2. This section describes the parameters used to run the simulations.

2.2.3.1 Geometry

The simulation consisted of an isotropic x-ray point source emitting 10^7 collimated x-rays on each run towards a 240×300 mm detector located 655.5 mm below the source. This number of histories allowed a statistical uncertainty below 0.1% for the total energy deposited at the lowest depth (Sempau et al.). The compression and support paddles were a 3 mm-thick layer of polyethylene terephtalate (PET) and a 1.7 mm-thick layer of carbon fiber, respectively. The voxelized breast volume was placed between the support and compression plates, laterally centered in the chest wall direction. A large cuboid of water simulated the patient's body. All the materials were obtained from NIST material definitions according to Hammerstein et al. (1979). Figure 2.5 depicts a cross section of the geometry used in the simulations.

2.2.3.2 Particle source

The x-ray spectra used (W/Rh 26 - 32 kV) were calculated using the TASMICS$_{\text{M-T}}$ model (Hernandez and Boone, 2014) and adjusted to match the previously-measured half value layer (HVL). The different x-ray spectra used in each simulation matched the technique used for
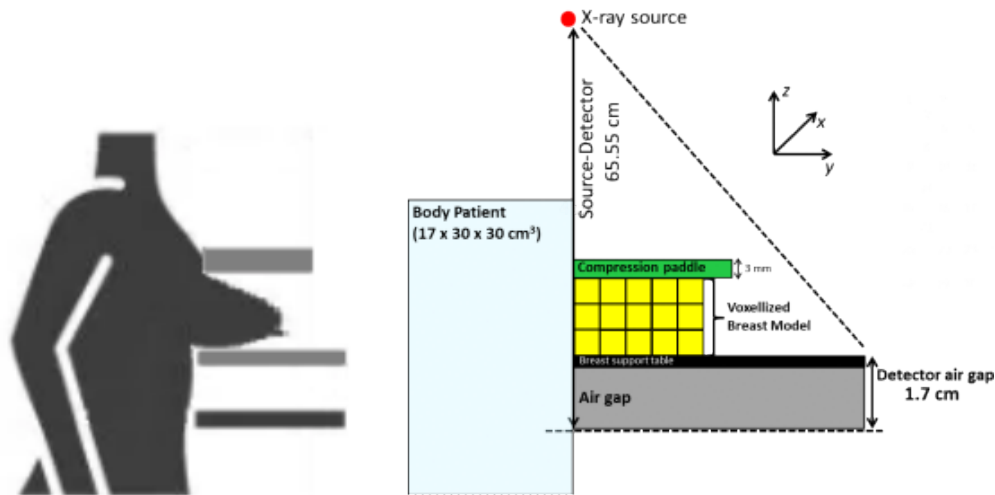
Figure 2.5: On the left, an illustration of a patient undergoing the mammography examination, with a compressed breast underneath the paddles. On the right, a diagram of the irradiation geometry used in the MC simulation. Original artwork, not to scale.

each patient's real mammogram according to the breast compressed thickness, as seen in table 2.2.

Compressed Breast Thickness (mm)	W/Rh Tube voltage (kV)	1st HVL (mm Al)
20-29	26	0.439
30-39	27	0.446
40-49	28	0.455
50-59	29	0.464
60-69	30	0.471
70-79	31	0.479
80-89	32	0.486

Table 2.2: W/Rh Tube voltage and corresponding half value layer (in mm of Al) used in the Monte Carlo simulations as a function of the simulated compressed breast thickness

The simulation of the physics interaction processes was performed using Geant4 electromagnetic Physics List Option 4. Photoelectric interactions, coherent and incoherent scattering were modeled using the EPDL97 library. This simulation did not include the heel effect and no backscatter effect form the patient's body was included in the simulation.

2.2.4 Dose evaluation

Photons were followed until they were completely absorbed of left the simulation volume. Each energy deposition event by means of photoelectric or incoherent scattering that occurred in a breast voxel marked as glandular tissue was recorded. Incident air Kerma was registered

as well. For the *patient-distribution*, patient phantoms set, with segmented discretized voxel values, only energy deposition events that occurred in the breast voxels marked as glandular tissue were recorded. If a particle hit an adipose tissue voxel, where g=0, the energy deposition was not recorded, but when the particle hit a glandular tissue voxel, the energy deposition was counted by the simulation. After all energy deposits were registered, the MGD was obtained. Regarding the *homogeneous and continuous* simulation sets, since all voxels have a certain percentage of fibroglandular tissue, there is always an energy deposition event that is recorded. In this case, the mean glandular radiation dose was estimated by weighting each energy deposition by the ratio of the mass energy absorption coefficients for the corresponding specific glandularity, as described in (Sechopoulos et al., 2012).

For each patient, once the mean glandular dose was obtained from the simulation, it was normalized by the IAK to obtain the normalized glandular dose DgN as in the equation:

$$DgN = \frac{MGD}{IAK} \tag{2.3}$$

The incident IAK was calculated within a 3 cm × 3 cm surface placed in contact with the phantom, 6 cm from the chest wall, laterally centered, with the compression paddle in place. I compared the average DgN for the continuous and homogeneous fibroglandular tissue distribution to the DgN of the phantoms with actual patient-based tissue distribution. The dose evaluation results of the proposed model are comparable to those obtained with an heterogeneous model, to say the patient-based distribution. Not only they were comparable, but the results also showed that the use of the patient-derived and the continuous models lead to a dose reduction by median factors of 30% and 27%, respectively. Fibroglandular tissue tends to be concentrated in the caudal direction of the breast, as explained in sec. 2.2.2, which reduces the amount of glandular tissue in the cranial part of the breast facing the x-ray source in the CC view. Consequently, the results imply that the estimated DgN is lower than the DgN obtained with the homogeneous approximation, as there is less dose-absorbing tissue present.

On the other hand, the results I obtained from the MC dose evaluation successfully address the dose overestimation that occurs from the use of the existing homogeneous model, as can be seen in the left box-plot in figure 2.6. The homogeneous model significantly overestimated the DgN by a factor of 1.43. Moreover, when the homogeneous model is compared to the continuous models it leads to a MGD overestimation by a factors of 1.39, as it is visible in the right whisker-plot. The adoption of an homogeneous distribution leads to an overesti-

mation of the D_gN in agreement with the previous studies (Dance and Sechopoulos, 2016a; **?**; Hernandez et al., 2015). Furthermore, the middle box plot demonstrates that the continuous model overestimates the DgN of the patient model by factor of 1.04. This finding suggests that, although preliminary, incorporating the spatial variation of the fibroglandular tissue can lead to improvements in delivered radiation dose estimates, potentially helping in the development of accurate dose models that better account for the breast anatomy as seen in breast CT.
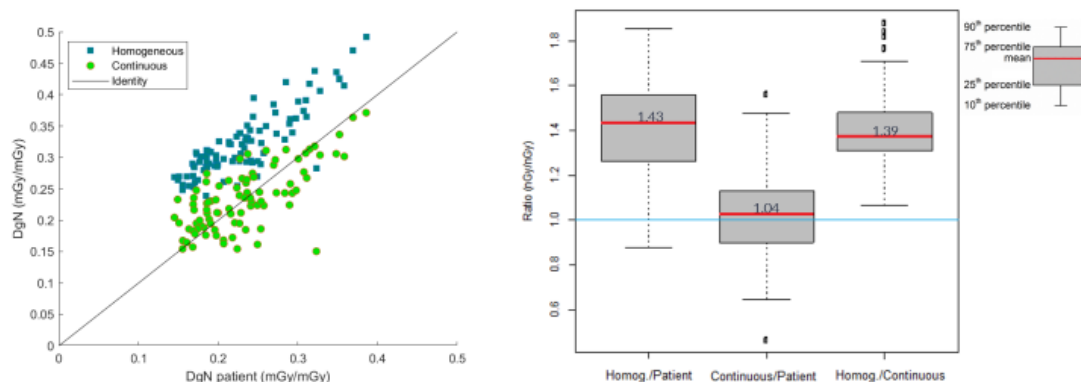
Figure 2.6: Left, comparison of the estimated DgN values for the homogeneous and continuous models to the corresponding DgN of the patient-based bCT model. The continuous model (green) fits closely to the patient based model. Right, Box–whisker graphic of the ratios between the three simulation sets under study. The continuous model more accurately mimics the patient-based approach. Original graphs.

2.3 Significance of the study

The use of a true 3D representation of the breast anatomy allowed for a thorough assessment of the 3D distribution of glandular tissue in patient's breasts. This assessment revealed that fibroglandular tissue has a tendency to be concentrated in the CC direction of the breast, which lowers the amount of glandular tissue and, consequently, the dose, in the cranial part of the breast facing the x-ray source in such direction. This work suggests using a continuous fibroglandular tissue distribution for a new breast dosimetry model that can accurately replicate a heterogeneous distribution and that accounts for the current dose overestimation caused by the homogeneous tissue approximation of the current breast models.

This work has been part of the investigations in the framework of the joint Task Group 282 that has just finished working on a proposal for a new breast dosimetry model. The results of this work have also been implemented as one of the steps for the development and validation of a method (Caballo et al., 2022) to generate patient-derived, heterogeneous digital breast phantoms for breast dosimetry in mammography and DBT that can reflect the average

heterogeneous distribution of the fibroglandular tissue in the compressed breast.

Chapter 3

Phase-contrast Breast Computed Tomography

The SYRMEP beamline at Elettra in Trieste has dedicated years of research to develop a clinical 3D mammographic system using PB PhC techniques in the SYRMA-3D (Synchrotron Radiation Mammography-3D) project. This project is a joint effort between health and research institutions in Trieste, and aims to provide high-resolution images of breast tissue with improved contrast and sensitivity. The major objectives of this chapter within such context are to outline the conditions for carrying out PB PhC breast CT, from the tomographic imaging configuration for data acquisition to image processing steps and quality evaluation. Among the contributions I made with this thesis was the implementation of the post-processing method for removing ring artifacts from the CT images, which is an important step in ensuring the high-quality data. Therefore, the ring-artifact removal process is developed with finer detail than other sections as I was majorly involved in it. Finally, the dosimetry system used to ensure patient safety during the imaging process is described.

3.1 The SYRMA-3D project

The Italian National Institute of Nuclear Physics (INFN) founded the project in collaboration with Elettra and the University Hospital of Trieste, with the goal of achieving the first clinical application of propagation-based phase-contrast breast computed tomography (PB-bCT or PhC-bCT) (Longo et al., 2016; Delogu et al., 2017b; Brombal et al., 2018c; Longo et al., 2019) using an upgrade of the PhC synchrotron radiation mammographic (Castelli et al., 2011) imaging setup available at the SYRMEP beamline.

The experimental set-up, which is based on the free-space propagation modality, is the most straightfoward to use of the phase-sensitive approaches. With a sufficiently coherent source, it only calls for a single exposure and an increase in object-to-detector distance over the conventional absorption configuration. As a result of the interference of the refracted X-rays,

as explained in 1, the PhC image will show an enhanced edge contrast (i.e. edge enhancement), resulting in increased visibility of the interfaces between different structures. There are some distinctions between PhC mammography and PB-bCT methodologies, such as the application of a phase-retrieval procedure to the projections prior to CT reconstruction (Cloetens et al., 1997), the use of a single photon counting detector, and state-of-the-art CT reconstruction algorithms for PB-bCT. The SYRMA-3D collaboration's activity covers different aspects of clinical study implementation (Longo et al., 2019), from Monte Carlo simulation software for dose evaluation (Fedon et al., 2015) to the development of a dedicated image quality assessment procedures (Brombal et al., 2019). However, SYRMA-3D is not the only synchrotron radiation-based BCT program: at the Imaging and Medical Beamline (IMBL) at the Australian Synchrotron ANSTO (Melbourne, Australia) a project with similar goals and methodologies is currently underway IMP (2023), with a longstanding collaboration between the Italian and Australian synchrotron laboratories (Gureyev et al., 2019).

3.2   Tomographic imaging set-up

The details of the experimental set-up used for the PB-bCT experiments carried out in the framework of this thesis are presented in this section. Following the description of the monochromatization and filtering of the SR X-ray beam 1.5.3, the monochromatic laminar X-ray beam passes through the experimental room and enters the radiological room, where a specifically developed patient support, which will be further described in the next section, allows rotation around the breast axis is positioned in the beam propagation direction. A custom-built ionization chamber is used to determine the exposure on the breast, and hence, to calculate the delivered dose. The CdTe photo-counting detector, capable of fully exploiting the peculiar characteristics of the SR source, is mounted on a motorized stage that allows positioning at different propagation distances in the plane perpendicular to the X-ray beam direction as shown in Fig. 3.1. Acquisitions are made at different propagation distances, where at 1.6 m is already enough to identify phase-contrast effects and prevent scattering contribution without the need for anti-scattering grids or specific scattering removal algorithms (Brombal et al., 2018c).

3.2.1   Patient support

As the X-ray source is stationary in a synchrotron facility, as opposed to a hospital setting, it is required that the patient lies in prone position on an an ergonomic tabletop that can rotate around the vertical breast axis. The breast (or breast mastectomy sample) is positioned in a

pendent geometry. The patient support enables for many centimeter-long horizontal and vertical translations with a precision better than 100 μm, while ensuring a consistent rotation speed, which is essential for CT acquisitions. A single scan is performed when a 180 °continuous rotation is completed, in contrast to a 360 °scan of clinical bCT systems. For most of the tomographic images presented in this work, the acquisition is accomplished in 40 s by setting the rotation speed to 4.5 deg/s. However, a multi-scan acquisition, typically made up of 10-15 vertical steps of the patient's support, is necessary due to the beam's laminar nature in order to scan a sizable amount of the breast, leading to an overall scan time of 7 to 10 min.

Unlike the clinical mammography with synchrotron radiation setup, the design for this bCT system does not require breast compression, which improves patient comfort. Since there are no compression paddles to hold the breast in place, bCT images are more susceptible to artifacts from patient movements, both voluntary and involuntary (e.g., breathing), due to the increased scan duration and decreasing rotation speed . Furthermore, the superior spatial resolution of this synchrotron bCT system, which is up to 7 lp/mm at 10% of the modulation transfer function or $\sim 0.1mm$ at full width at half maximum (FWHM) (Brombal et al., 2019), makes it vulnerable to small displacements. A further discussion on the the effect of patients' motions on the quality of PB-bCT images, as well as the strategies to prevent and compensate such issue are detailed in section 4.1.

3.2.2 Detector and data pre-processing

A high efficiency and high spatial resolution detector is required to detect phase effects in order to produce low dose phase-contrast images. Photon-counting detectors offer remarkable advantages over conventional indirect detection and charge integration systems, as they show minimum electronic noise and high detective efficiency (Takahashi and Watanabe, 2001; Ballabriga et al., 2016) and the spatial resolution is mainly limited by the pixel size (Taguchi and Iwanczyk, 2013). However, to obtain a large field of view, the detector's architecture must employ arrays or matrices of sensors (Delogu et al., 2017b; Mozzanica et al., 2016).The alignment of the sensors in such modular detectors can be critical, possibly leading to image distortions, as well as the energy threshold equalization among the modules (Brombal, 2020c).

The SYRMA-3D experimental setup employs the PIXIRAD-8 detection system, produced by PIXIRAD Imaging counters s.r.l., a spin-off company of INFN (Bellazzini et al., 2013; Vincenzi et al., 2015). The imaging device, which is depicted in figure 3.2, is a high-efficiency photon-counting detector with a linear response at 2×10^5 photons per pixel per second and a
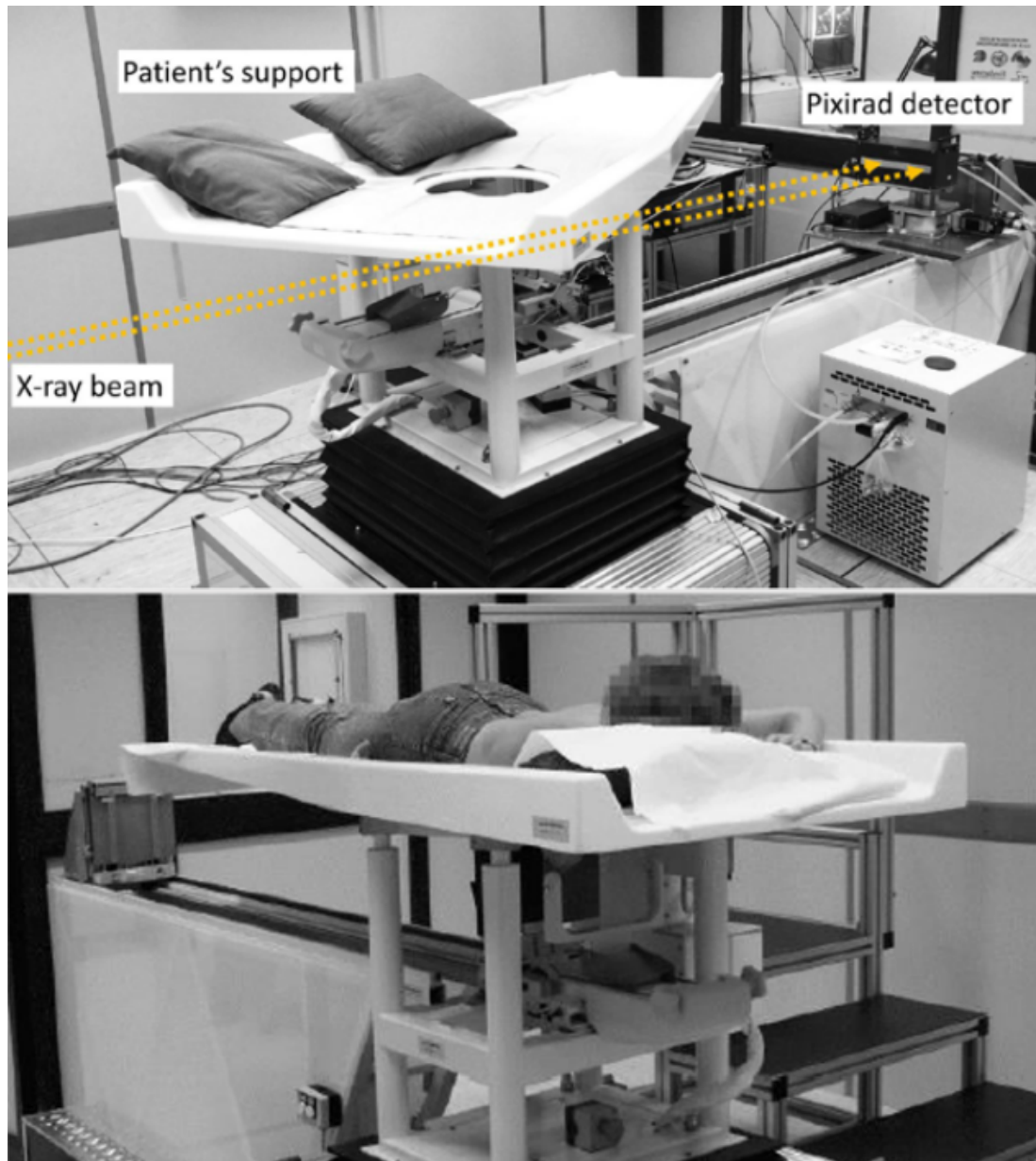
Figure 3.1: Images of the experimental setup in the radiological station. On the top, the rotating patient support with the ergonomically designed hole at the center and a lateral view of the Pixirad-8 detector. On the right, a prone-positioned patient with the breast in a pendant geometry.

global active area of $246{\times}25$ mm^2 that fits with the beam cross-section 21 cm$\times$ 5 mm. Pixirad-8 is made of a 650μ thick crystalline CdTe sensor, with an array of 8 modules tiled together, with a dead space of 180 μm between two adjacent modules. Each module has an active area of $30.7{\times}24.8$ mm^2, allows high direct detection efficiency and minimizes the loss of spatial resolution due to blurring of light in scintillator-based systems. The detector features 4096×476 pixels in a honeycomb matrix pixel arrangement with a pitch of 60 μm in the horizontal

direction and 52 μm in the vertical directions (Delogu et al., 2017a). Each pixel is associated with two independent 15-bit counters, which can be used either in spectral or in dead-time-free mode. The spectral mode allows to set two different energy thresholds, thus, enabling spectral imaging (Brun et al., 2019). In this work, the thresholds of both counters are set to the same value, and one counter is filled while the other is read, thus performing continuous irradiation of the samples without losing counts or requiring a synchronized shutter. The global energy detector threshold was set to 3 keV during acquisitions to safely remove electronic noise while preserving detection efficiency (Di Trapani et al., 2020). The detector is always run at the highest frame rate of 30 fps, in order to maintain scan times as brief as feasible, which results in 1200 evenly-spaced projections over the course of 40 s long rotation. More information on detector performance (e.g., spatial resolution, noise, operation modes) is provided by Delogu et al. (2016).
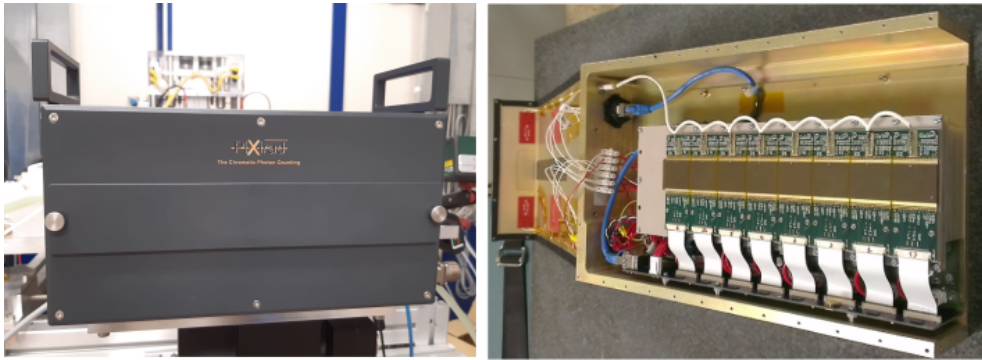
Figure 3.2: View of the Pixirad-8 detector placed in the experimental room (left). On the right, the interior of the CdTe detector system. Picture on the left was taken by the author, image on the right was taken from . Longo et al. (2016).

Photon-counting detectors usually suffer from local charge-trapping effects due to impurities in the sensor crystalline structure, that are dependent on the polarization time and on the exposure (Knoll, 2010; Astromskas et al., 2016; Park et al., 2014; Pennicard and Graafsma, 2011). In CT applications, the scan duration may be in the order of several seconds or more (Delogu et al., 2017a) where a single tomographic image requires hundreds of projections continuously acquired in several seconds. In absence of a dedicated pre-processing procedure, these effects can lead to severe ring artifacts which alter significantly the image quality, possibly impairing its scientific or diagnostic significance. For the SYRMA-3D experiment, an *ad-hoc* pre-processing procedure (Brombal et al., 2018a) has been developed for the Pixirad8 CdTe detector raw data to compensate for detector-related artifacts, and yielding a set of corrected projections ready to be phase-retrieved and reconstructed. The dedicated pre-processing

code comprises dynamic flat-fielding, gap seaming, dynamic ring removal, projection despeck-ling and around-gap equalization. A typical experimental dataset comprises 1200 16-bit raw projections, with a dimension of 2300×70 pixels each, and requires about 4 minutes on a 8 cores Intel Core i7-6700 CPU @ 3.40 GHz, including loading and saving operations Brombal (2020c). This procedure allows the effective removal of time-dependent artifacts, preserving the main image features, including phase effects.

3.2.3   Propagation distance

In order to detect the interference pattern in Pb-bCT and maximize the phase-contrast signal, the required free-space or propagation distance z_1 must be optimized for the detector's spatial resolution and the experimental design as explained in sec.   1.5.2.   This optimal distance will also depend on the specific characteristics of the object being imaged. In this context, a further study by Brombal et al. (2018b) evaluated the effect of changing the object-to-detector distances on the SNR gain, contrast and spatial resolution on images with and without the application of PhR. This experimental study, carried out prior to the author's doctoral program, is further detailed because it directly affects how the investigations conducted for this thesis were developed.

The effect of the propagation distance on the image quality was investigated by Brombal et al. (2018b) based on the scans at 30 keV of total mastectomy specimens acquired with the previously described experimental setup. Each scan was constituted by 1200 projections that underwent the previously described *ad-hoc* pre-processing procedure (Brombal et al., 2018c), and were subsequently phase-retrieved considering a glandular/adipose interface $(\delta_1 - \delta_2)/(\beta_1 - \beta_2) = 795$. The reconstructions were performed using a graphics processing unit (GPU) with well-known filtered-back-projection with a Shepp–Logan filtering (Brun et al., 2015).

Firstly, the images on fig.3.3 show that if no PhR is used (a-c), there is no significant variation in signal and noise when the propagation distance is varied. The edge-enhancement effect at the interfaces between the two different tissues is amplified at increasing propagation distances. Secondly, after the application of the PhR algorithm, increasing the propagation distance results in significant variation in signal and noise (d-f), giving rise to phase-retrieved reconstructions with no loss of spatial resolution. However, when the PhR is applied, the edge appearance does not change when the propagation distance is varied, and the edge enhancement is no longer present.
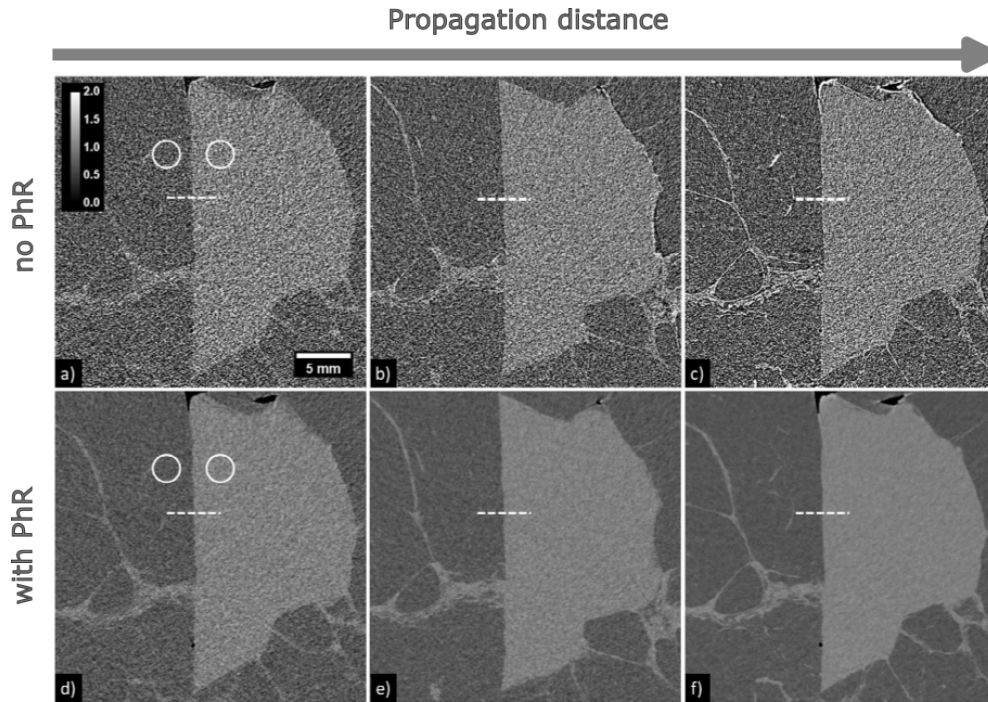
Figure 3.3: Zoom of a reconstructed slice of a sharp adipose/tumor interface produced by a surgical cut is displayed. Images were acquired without (a-c) and with (d-f) phase retrieval at increasing propagation distances. One of the five pairs of circular ROI is displayed in images a,d, as an example of the ROIs that were used to determine contrast and SNR. The dashed line was used determine a line profile for the spatial resolution measurement. Image adjusted from Ref. Brombal et al. (2018b)

Fig.3.4 shows a graph that presents the quantitative evaluation of the different parameters in the phase-retrieved images (blue points) and the theoretical predictions (red lines) (Gureyev et al., 2017) plotted as a function of the propagation distance (R').

The outcome of the qualitative analysis of the phase-retrieved images, as presented in 3.4 can be summarized as follows:

- *Spatial Resolution:* propagation causes the edge-enhancement effect, which boosts the image's high spatial frequency component and thus improves spatial resolution. Following the propagation process, the phase-retrieval algorithm is used as a special low-pass filter, as described in Section 3.3.1, which reduces noise but degrades spatial resolution. Thus, combining propagation and phase retrieval has no effect on spatial resolution.

- *SNR:* when the PhR algorithm is used, changing the object-to-detector distance improves the signal-to-noise ratio. The propagation distance scales approximately linearly with the gain factor. There is a four-fold gain in SNR when the PhR is applied, implying that phase retrieval has a significant impact on image quality.
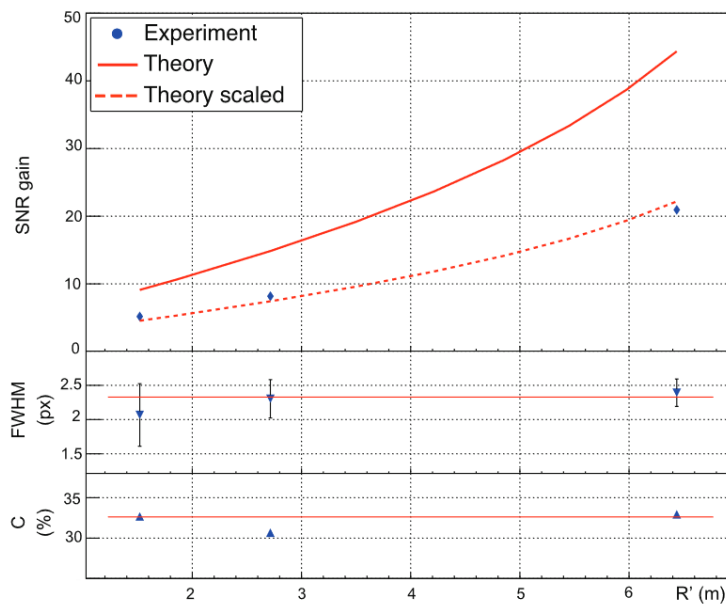
Figure 3.4: Comparison between experimental results (blue points) and theoretical predictions (red lines) as a function of the propagation distance from the study by from Ref. Brombal et al. (2018b). Some error bars are smaller than points.

- *Contrast:* Since phase retrieval affects image noise, while propagation distance affects spatial resolution, the contrast does not change either when the phase retrieval algorithm is used, or when the propagation distance is changed.

This model is valid within the near-field propagation description which means that SNR gain cannot arbitrarily increase, implying that there is a limit in the maximum achievable SNR gain. Moreover, this study on a surgical breast specimen indicates that by combining the free-space propagation phase-contrast technique and the phase-retrieval algorithm, it is possible to obtain a major SNR improvement with respect to conventional imaging, at a constant spatial resolution, which is beneficial for improving the visibility of low contrast features in soft tissues like in the breast.

These results are of great importance within the context of the SYRMA-3D project to better exploit the advantages of the free-space propagation technique in breast CT clinical applications. It is worth clarifying that the imaging set-up for the PB PhC CT acquisitions of whole breast (explained in ch. 4) are carried out at different propagation distances than for the acquisitions of paraffin-embedded tissue samples (presented in ch. 5). Since major contrast variations are not observed neither changing propagation distance nor applying the phase-retrieval, the image appearance will look 'familiar' to a clinician's eye, who will not need

a specific training to read the images. This has propelled further investigations in collaboration with the ANSTO synchrotron, specifically in a radiological assessment through a visual grading analysis study between IMBL images(using flat-panel detectors) and SYRMEP images (using photo-counting detectors), discussed in the next chapter.

3.3 Tomographic image processing

3.3.1 Phase-Retrieval

In conventional tomography the reconstructed images are obtained by the application of conventional FBP algorithm and represent maps of the X-ray attenuation coefficients of the sample. Differently, with the PB PhC approach, the application of the reconstruction procedure produces images containing a mixture of contributions from absorption and phase shifts occurring in the sample. Other experimental parameters, such as X-ray energy, geometrical magnification, radiation coherence, and system resolution, influence intensity modulation at the detector (Endrizzi, 2018). Other practical applications benefit when phase-shift information is extracted separately from absorption information from the wave originating from the object (Pelliccia and Morgan, 2018), which is not the case here. To improve the image contrast and reduce the image noise in the PB PhC reconstruction images, a pre-processing algorithm called Phase retrieval is used. This filter, applied prior to the conventional reconstruction algorithm, exploits the edge enhancement effects of the PB PhC technique to improve the identification of the different sample details/ components. In general, phase retrieval algorithms allow to retrieve phase from absorption properties of the samples needed for the acquisition of images at different propagation distances. However, the most used one, proposed by Paganin et al. (2002), makes an approximation valid for an homogeneous object, composed by a single material, and both δ and β (or their ratio) are known, and it is applicable on a single distance. The intensity and phase terms can be expressed as a function of the same variable $t(x,y)$, thus reducing the number of unknowns in the Transport-of-intensity equation TIE. The phase and intensity on the object plane can be written as

$$I(x,y;z=0) = I_0 e^{-2k\beta t(x,y)} \text{ and } \Phi(x,y;z=0) = -k\delta t(x,y) \tag{3.1}$$

where the only unknown term is t(x;y), hence the TIE-HOM (TIE for a homogeneous object) equation and can be solved. The solution provided by Paganin et al. (2002) makes use of the Fourier derivative theorem, deriving a bell-shaped PhR filter in Fourier domain, that can

be written as:

$$\tilde{H} = \left(1 + \frac{z_1 \delta}{2k\beta}|\mathbf{v}|^2\right)^{-1} \tag{3.2}$$

The effect that different parameters, such as PhR, noise and propagation distance can have in the final image appearance has been previously studied. The work by Nesterets and Gureyev (2014) investigates the effect of phase-retrieval algorithms on the variance of noise in the reconstructed projection images, showing that using PhR allows for significant improvements in image quality by increasing the signal-to-noise ratio (SNR) at low radiation doses to the patient. Gureyev et al. (2017) performed another analysis on the effect of this filter, which similar to a numerical convolution with a low-pass filter: to reduce the image noise without sacrificing spatial resolution. This study also confirmed that the combined effect of free-space propagation and the application of PhR increases the SNR, while preserving spatial resolution and contrast in areas far from sharp interfaces where edge-enhancement is present.

For the case of PB-bCT, the object is the breast or breast sample, which is composed by two (homogeneous) materials of interest, mainly glandular and adipose tissues. The PhR filter is modified to:

$$\tilde{H}_{2\mathrm{mat}} = \left(1 + \frac{z_1}{2k}\frac{\delta_1 - \delta_2}{\beta_1 - \beta_2}|\mathbf{v}|^2\right)^{-1} \tag{3.3}$$

where the δ/β term has been replaced by $(\delta_1 - \delta_2)/(\beta_1 - \beta_2)$, also known as γ, and the subscripts refer to the two materials of interest (Burvall et al., 2011). For breast imaging at energies around 30 keV, δ/β is of the order of 2×10^3 in the single-material PhR, while $(\delta_1 - \delta_2)/(\beta_1 - \beta_2)$ is of the order of 1×10^3 for glandular/adipose interfaces in the two-materials PhR (Brombal, 2020c).

For the tomographic images acquired during this thesis investigations, the phase retrieval filter was applied to the projections prior to the actual reconstruction, whether a PhR single-material or a two-material filter. In terms of signal processing, using single-material PhR would result in a smoother image (i.e. less noise and more blur) than using two-material PhR (Brombal et al., 2018c). The phase-retrieved projections were normalized to the same average intensity as the projections without phase retrieval, denoting that they are maps of linear attenuation coefficients, which is the method used in traditional X-ray tomography (Piai et al., 2019). A comprehensive discussion on the phase-retrieval filter used for PB-bCT images, including experimental results obtained by the SYRMA-3D collaboration, is found in the works of Brombal et al. (2018c) and Donato et al. (2019b).

3.3.2 Image Reconstruction

A tomographic acquisition requires several planar 'views' of the sample, or projections, obtained by exposing the object to the X-ray beam at different angles. Each projection, collected at a certain angle, will be the line integral through the sample of a given object spatial distribution function. To reconstruct a tomographic image means to invert the Radon transform of acquired parallel beam projection data. This can be accomplished by acquiring the projection images over 360 °for divergent beams and 180 °for parallel beams, and by applying an algorithm, which is responsible for taking the raw data of the 2D projections and converting them to images into a 3D volume. There are many different algorithms used for CT image reconstruction, such as Iterative algorithms (IR) and FBP, being the latter the typical gold standard to assess the performance against other reconstruction algorithm, but may result in artifacts and reduced image quality (Buzug, 2011). In the case of PB-bCT, the tomographic reconstruction requires applying a GPU-based FBP with a Shepp-Logan filtering to a large number of phase-retrieved projections (i.e. 1200) via (Brun et al., 2017). The image contrast is found to be proportional to the (conventional) attenuation image $\mu_{(x, y, z)}$ in the reconstructed image, meaning that the image contrast is equal to the attenuation contrast. As a result, tomographic images that have been rebuilt using the PhR method, as mentioned in the previous section, can be calibrated using linear attenuation coefficients, as in conventional CT (Piai et al., 2019). It is important to note that the reconstructed voxel size is 57 μm$\times$ 57 μm$\times$ 50 μm due to the honeycomb structure of the pixels and the minor beam magnification (Longo et al., 2019).

On the other hand, IR is a more complex algorithm that requires more computational power, but with the ability to produce higher quality images with reduced noise and artifacts. Several promising outcomes in the field of PB-bCT have been reported in Donato et al. (2019b). A further investigation on a viable reconstruction algorithm substitute for FBP in PB-bCT images is explained in sec. 4.4, where I collaborated in comparing a customized SART algorithm against other reconstruction algorithms.

3.3.3 Post-processing correction: Ring-artifacts

The dedicated pre-processing code described in 3.2.2 comprises a dynamic ring removal algorithm to remove ring artifacts produced by gain inhomogeneities at the pixel level by making use of the alpha-trimmed filter, which is a hybrid of the mean and median filters (Bednar and Watt, 1984). The equalization factor *alpha* varies with the projection index, allowing to cope with non-constant ring artifacts.

However, the PIXIRAD-8 detector's architecture employs an array of 8 modules tiled together, with 3-pixel-wide gap between adjacent modules. Therefore, an around-gap fixing equalization factor, that also depends on the projection index, is applied as part of the pre-processing procedure to compensate for slow gain variations of close-to-gap pixels. Due to the demanding requests on high contrast resolution and low dose, images in breast CT are particularly sensitive to small imperfections of the dynamic flat field correction of the pre-processing procedure (Delogu et al., 2017a). Great care was taken in the design of the software and filter optimization in order to preserve phase effects, which are of paramount importance in a synchrotron-radiation-based experiment. In PIXIRAD-8 detector, there are some inhomogeneities that show a time dependent gain and are systematically reproducible with the exception of the pixels on the sensors edges. The small imperfections have a dependence on the polarization time of the sensor (i.e., how long the detector is on) and time-dependence of CT hardware systems will result in time-dependent ring artifacts (Yang et al., 2020) with a non-constant intensity. Moreover, CdTe photon-counting detectors usually suffer from the local charge trap effects, which usually depend on the polarization time and the exposure time (Brombal et al., 2018a). Time-dependent ring artifacts are visible as stripe artifacts in the polar coordinate system in the sinograms. A typical profile of a full stripe exhibits intensities that are offset at all angles compared with that of a neighboring good pixel (see figure 3.5). After reconstruction, the stripe in the sinogram gives rise to a ring artifact, in this case a half-ring due to the 180° sampling, in the reconstructed image. According to the work of Brombal et al. (2018a) and Yang et al. (2020), for a photon counting CT system, the actual time-dependent stripe artifacts are discontinuous in the polar angle direction, for which the gray value is not constant.

Pre-processing correction methods work on the raw projections, and it is difficult to intuitively select parameters, which limits the applicability of these methods. Furthermore, removing the stripe artifacts in the raw projection sinograms through simple low-pass filters cause a decline in high-frequency details and deteriorates image quality(Kowalski, 1978). In the case of commercial CT systems, they often go with the manufacture's reconstruction software, which may only output reconstructed images to end-users. This greatly limits the application of pre-processing methods (Yang et al., 2020). Post-processing methods have better adaptability and flexibility as they operate directly on the reconstructed images. In this frame of reference, an *ad-hoc* ring removal software that uses a method combining raw projections and reconstructed

images was developed by Bruno Golosio, of the Department of Physics, University of Cagliari and INFN Division of Cagliari, Italy.
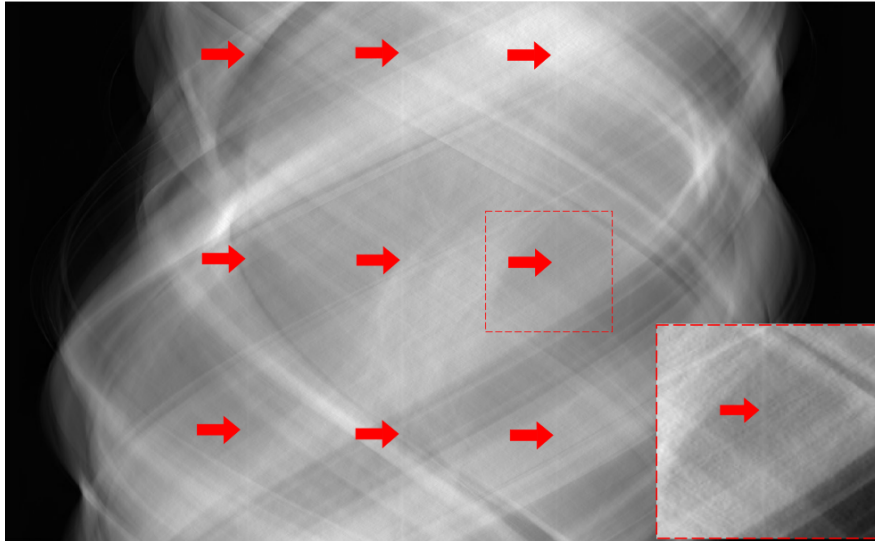
Figure 3.5: Demonstration of the full stripes artifacts along a sinogram (arrowed). To the right, an enhanced view of part of a stripe artifact. Original image by the author.

3.3.3.1 *Ad-hoc* ring removal methodology

The *ad-hoc* software (Dering 1.0.1 beta, 2013) features a graphical user interface that allows users to manually select an arc region of interest to remove important ring artifacts on a reconstructed image, yet the correction method is applied to the sinogram space corresponding to the selected region. According to the assumption that the gray-value characteristics of the ring artifacts are local extrema (Kyriakou et al., 2009), the user can select and threshold the region where the local depression is located. The selection of parameters is, however, very important to the resulting corrected image, as changing them directly influences the final display.

Some important properties of the methodology are :

- *Selection of the affected areas in a reconstructed image:* the sinogram of the artifact-affected image is used to yield its reconstruction, which is performed by the software using direct Fourier method (DFM) based on the projection theorem (Stark et al., 1981). This quick reconstruction, that implements an interpolation algorithm to convert discrete polar data to Cartesian data, is made just so that the user can carefully review the visible ring artifacts 3.6. A small homogeneous arc area within the half-ring artifact is selected for the equalization of the artifact correction, whereas a larger area can be selected to perform the correction that will be applied to the sinogram.
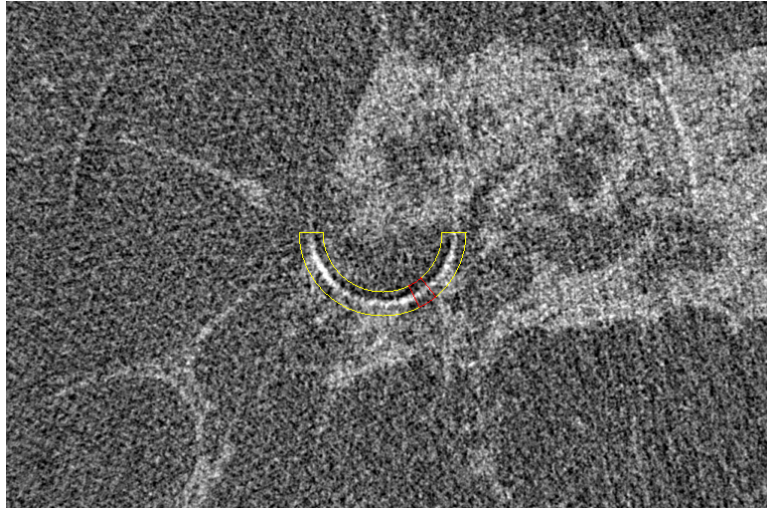
Figure 3.6: User selected regions for: equalization (in red) and the ring artifact correction (in yellow). Original screenshot of the author's work when using Dering (1.0.1 beta, 2013) software.

- *Intensity profile correction:* The region can be thresholded according to where the local depression is located, as artifacts differ from location and intensity. A example of a graph of the intensity profile of the sinogram, in correspondence to the selected equalization region, is displayed in fig. 3.7. The red graph corresponds to the uncorrected sinogram's intensity profile, and it shows a depression related to the artifact. The blue graph represents the correction to be applied with using a simple linear interpolation between two points.
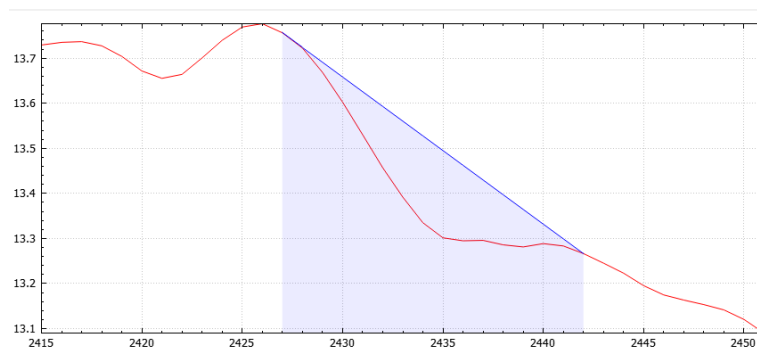
Figure 3.7: Graph of an intensity profile in the sinogram. The red graph represents the profile in the uncorrected sinogram. The blue graph represents the user selected region for the linear interpolation correction to be applied. Original screenshot of the author's work when using Dering (1.0.1 beta, 2013) software.

I employed the methods outlined in fig. 3.8 to reduce the (possibly) time-dependant detector ring artifacts in the PB PhC images acquired for the research detailed in this thesis. It is crucial to keep in mind that the manual selection of the region of interest determines the
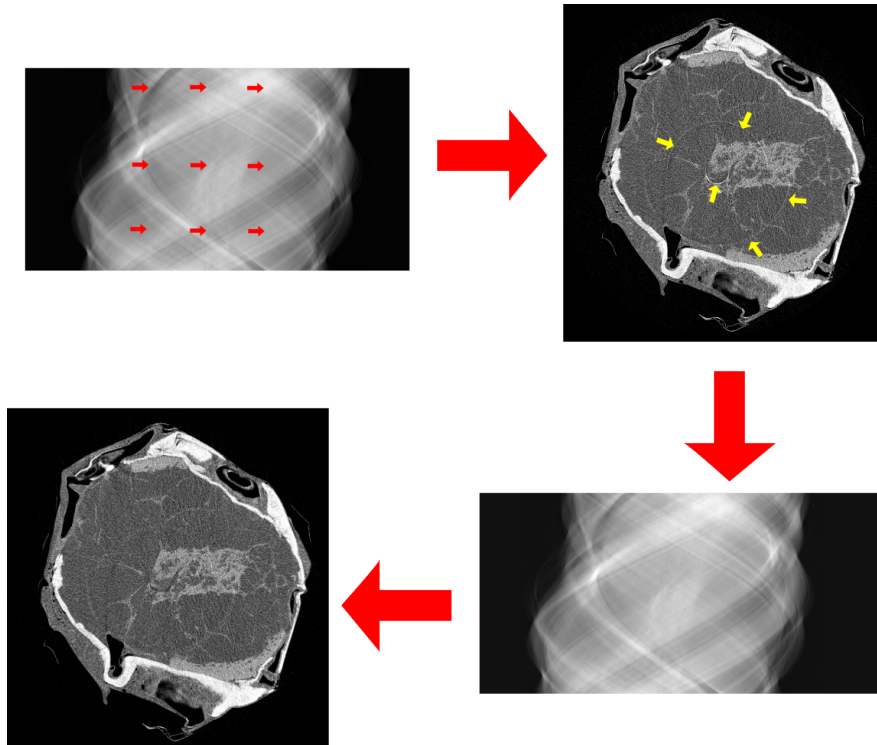
Figure 3.8: Images of the ring removal procedure. Upper left: the sinogram with visible stripe artifacts (red arrows). Upper right: the reconstructed image showing the half-ring artifacts. Lower right: sinogram after applying the correction software. Lower left: final reconstructed image with a reduction of the presence of ring artifacts, showing no apparent negative effects with respect to anatomical information. Original image by the author.

correction in the final reconstruction image, and such selection has a considerable impact on the appearance of the final corrected image. Therefore, the method may result in some remaining ring artifacts or the introduction of other ring artifacts and the procedure might need to be repeated. Although it is time-consuming to manually correct the time-dependant ring artifacts, with the proper choice of parameters, the use of this *ad-hoc* software successfully removes such artifacts, while preserving the image details.

An example of the visible ring artifacts that emerge in the reconstructed tomographic images is shown in fig. 3.9. Images of three different breast mastectomy samples acquired at 25 keV and a propagation distance of 3.7 m are shown. I made a simple evaluation on the the ring intensities using a line profile (red) in the same position for each sample. The methodology was extended to the positions of other artifacts in the three samples. An inset of the line profile of the middle ring, the most evident ring artifact, is displayed on the top left for each sample. The inset shows that the trend of the gray values is not constant, as a spike is observed in the position of the ring artifacts. The small inhomogeneities within PIXIRAD-8

result in a dependence on the polarization time of the sensor that cause time-dependent ring artifacts, leading to the visible variations in intensity of the ring artifacts in specific positions, as described by (Brombal et al., 2018a), therefore, the originating effect is not random. I also observed that these artifacts were also visible in the orthogonal views of the scanned sample (along the volume), evidencing that they represent a three-dimensional problem that requires an additional post-processing ring-artifact correction.
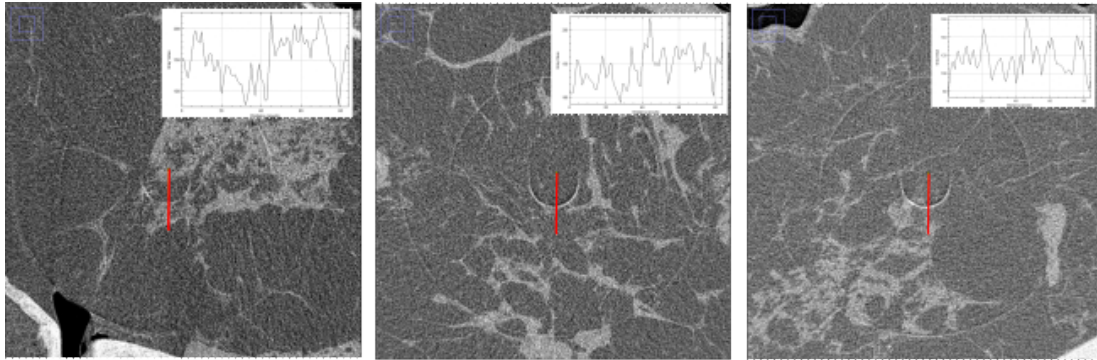
Figure 3.9: Visible ring artifacts in the images of three different breast mastectomy samples. A line profile (red) was used to assess the intensity of the artifacts. The insets correspond to each line profile graphs respectively. Images were acquired at a propagation distance of 3.7 m while operating at 25 keV. Original image by the author.

3.4   Dosimetry system

Any clinical mammographic imaging equipment needs a quality control protocol to ensure high image quality and the highest patient saftey, with a proper dose assessment and overall image quality assesment that includes metrics on low-contrast detection, spatial resolution and noise, as already introduced in 1. The SYRMA-3D PB-bCT program is no exception. To ensure that image acquisitions from PB-bCT are performed at acceptable radiation dose levels, the custom dosimetric system previously developed for the mammography program is employed. Two custom-made high-precision ionization chambers (beam monitors) are positioned about 3 meters upstream from the breast (or breast sample), see Fig. 1.7. The ionization chambers have been calibrated against the standard air kerma chamber for low-energy X-rays over a wide energy range (9-40 keV) (fig. 3.10). The entrance radiation dose is measured in terms of absolute air kerma, which is used to define exposure parameters in the chambers. The radiation flux can be finely tuned by filtering the beam with electro-actuated aluminum sheets of thicknesses ranging from 0.125 to 7.875 mm to match a given dosimetric quantity. The air ionization are simultaneously read. In the event of any accidental event or a discrepancy

between the readings of the two ionization chambers, the safety system quickly stops the beam by a fast shutter system that operates in 15 ms (Longo et al., 2007).

Figure 3.10: An image of one of the two custom-made ionization chambers to monitor the beam placed ahead from the breast sample. Original photo taken by the author.

The MGD in a mammogram is calculated under the assumption that the entire breast will be subjected to X-rays (Hammerstein et al., 1979), but in the studies of SYRMA-3D, just a partial part of the breast will be exposed to radiation. Therefore, when only a partial scan of the breast is needed, the glandular absorbed dose in the irradiated volume (MGDv) is an appropriate dosimetric measure. The MGDv is calculated by multyplying the air kerma value at the breast position (scanner isocentre) by a conversion factor that takes into account breast size and glandular fraction. This conversion factor was obtained from an *ad-hoc* Monte Carlo simulation developed for SYRMA-3D studies (Mettivier et al., 2015) based on a GEANT4 code optimized for breast dosimetry (Fedon et al., 2015). The dose reference value for the clinical exams in the SYRMA-3D project has been of 5 mGy (Mettivier et al., 2015), which is lower than (or comparable to) the existing BCT systems but slightly higher than a standard two-view mammography. However, The EUREF limits the mean glandular dose to the breast to 5 mGy for a two-view screening DM in a normal-size breast.

Due to the unique nature of the SYRMA-3D examination set up, a dedicated image quality assessment procedure was developed (Contillo et al., 2018), taking into account the coherent and monochromatic nature of the imaging beam while complying with the quality control requirements of both mammography and CT protocols. For this purpose, a custom-made QC
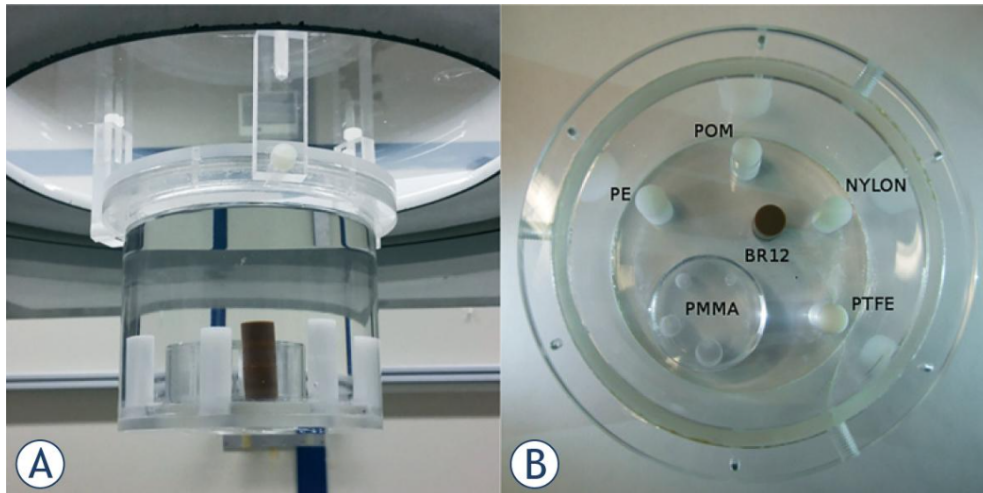
Figure 3.11: (A) The QC phantom (diameter 12 cm, height 10 cm) fixed at the pendant breast position on the SYRMA-3D patient support. The upper portion is uniformly filled with water, while the radiographic details are visible in the lower portion. (B) Arrangement of the details (rods of 1.2 cm in diameter) at the bottom of the QC phantom. The low contrast resolution structure made of PMMA is also shown. Image taken from Contillo et al. (2018).

phantom was designed and built by the SYRMA-3D collaboration at the laboratories of the University of Ferrara, Italy.

The phantom in fig. 3.11 is composed by several rods of different tissue-like materials, namely a polymethyl methacrylate (PMMA) cylindrical container filled with demineralized water and a set of five plastic rods made of polyethylene (PE), nylon, polyoxymethylene (POM), polytetrafluoroethylene (PTFE) and BR12 breast-tissue equivalent material, respectively. These materials were chosen to mimic the attenuation and contrast of breast tissues. A structure for low contrast resolution tests include a PMMA insert exhibiting five holes of varying diameter. The custom-made phantom allows to perform absolute image calibration in terms of attenuation coefficients, and to perform different quality tests, such as evaluating the accuracy and reproducibility and testing image uniformity, noise fluctuations and low contrast resolution (Piai et al., 2019). This phantom was later used for CNR and spatial resolution measurements for the optimization of a customized simultaneous algebraic reconstruction technique algorithm for phase-contrast breast computed tomography, which will be presented in ch. 4.

Chapter 4

Experimental PB-bCT developments

Soft tissue contrast sensitivity has the potential to be dramatically improved by propagation based X-ray phase-contrast imaging, which requires a spatially coherent source and a sufficient object-to-detector distance. By using a propagation distance and a PhR algorithm, the transition from absorption reconstructed CT images to phase retrieved images can be achieved, with a significant reduction in image noise at the same contrast and spatial resolution levels, which is especially important for improving the visibility of low contrast features in soft tissues like the breast. PB-bCT has already shown its capability of providing fully-3D images with high contrast-to-noise ratio at clinically compatible radiation dose levels (Longo et al., 2016; Pacilè et al., 2019), yet the scanning parameters and hardware necessary to produce the highest quality diagnostic images are still being investigated in preparation for the clinical trials that are foreseen in the upcoming years (Longo et al., 2019; Taba et al., 2021). The SYRMA-3D collaboration has been working in the last years to evaluate, quantify and optimize the main parameters of the PB-bCT imaging technique in terms of x-ray energy (Delogu et al., 2019; Oliva et al., 2020), sample-to-detector distance (Brombal et al., 2018c; Brombal, 2020b), strategies for CT scans and reconstruction workflow (Longo et al., 2019; Brombal et al., 2021). The studies by Brombal et al. (2018b,c) analyze the effects of propagation distance and detector pixel size on image noise and signal-to-noise ratio in the context of the SYRMA-3D project, with direct implications on the experiments carried out in this thesis.

This chapter provides an overview of the research results from the experiments within the SYRMA-3D project during my doctoral program. In addition to the demanding specifications for breast imaging modalities, attempts to guarantee high-quality images should consider patient motion and potential compensatory procedures. Therefore, in this thesis I evaluated two alternative approaches to address the issue of patient movements: first, to lessen breast move-

ment that might result in motion artifacts by developing a breast immobilization device, which is described with finer detail than other sections as it was entirely my own project. Second, to assess patient breathing motion and establish a corrective mechanism to compensate such motions. Amongst the demanding specifications for breast imaging, the choice of the algorithm used for CT image reconstruction is essential for producing accurate and reliable CT images that can aid in the diagnosis and treatment of medical conditions. In this context, an optimization of a dedicated reconstruction method developed for PB-bCT and a collaborative radiological assessment study with the Australian Synchrotron were carried out, where I participated in the reconstruction and post-processing of the acquired images in both studies. The results presented in this chapter proactively support the ambitious goal of establishing a future clinical development of the PB-bCT program at SYRMEP beamline at Elettra synchrotron facility in Trieste.

4.1   The effect of patient motion

The presence of patients' motion-related artifacts and their impact on the diagnostic significance of the examination is still an open issue in breast CT. Due to the high resolution required for breast imaging, strategies for motion prevention and compensation are necessary to ensure high-quality bCT images. Patient's breathing motion and their possible effects in synchrotron-based PB-bCT imaging needs to be taken in consideration. However, it's also important to take into account potential motion artifacts brought on by the patient rotating around the vertical breast axis during CT acquisition. These motions can result in various artifacts in tomographic images, such as blurring and streaks.

In bCT, there are no compression paddles which constrain the breast in a fixed position, as in DM, making bCT images more prone to artifacts due to patient movements, either voluntary and involuntary (e.g., breathing). These effects are more critical in synchrotron-based PB-bCT than in hospital-based bCT setups for some reasons:

- the scan duration is generally longer at synchrotrons (from tens of seconds to few minutes) as the patient must be rotated instead of the x-ray source, thus limiting the rotation speed .

- synchrotron's bCT laminar x-ray beam features a cross-section at the sample of 150 mm (horizontal) $\times$ 5 mm (vertical), therefore, the field-of-view (FOV) for each scan is much smaller than the whole organ, causing the scan to be take longer to image the whole

breast.

- the spatial resolution of the synchrotron bCT systems (at SYRMEP) allows for a reconstructed voxel size of $57 \times 57 \times 50 \mu m^3$, in contrast to an isotropic cubic voxel of 273 μm^3 of a clinical bCT system (Koning, 2022), making synchrotron-based PB-bCT more sensitive to small displacements.

- the lack of compression paddles to hold the breast in place, make bCT images (either synchrotron-based or conventional) to be more susceptible to artifacts from patient movements, both voluntary and involuntary (e.g., breathing)

Tacking into account that patient motion may create artifacts that potentially impact on the diagnostic accuracy of the examination, I evaluated different approaches in the framework of studying the effects of patient's motion and compensation methods were carried out within the SYRMA-3D project that are explained in the next sections.

4.2 Breast Immobilization system

According to Rößler et al. (2015), tissue coverage in prone breast CT is highly dependent on patient table design and an immobilization device included in the tabletop may be advantageous to avoid motion during image acquisition. Moreover, their study stated that an immobilization device using underpressure may also be useful to pull more breast tissue into the field of view. As a result of their encouraging findings with the underpressure system, and the need for a strategy to prevent motion during pendant bCT acquisitions, I developed a scheming of a breast immobilization device for PB-bC with an underpressure system.. The challenge arose in designing a breast holder that could adapt to the natural forms and sizes of breasts in a pendant geometry, had a straightforward construction, was radiotransparent, and that it could be used for phase contrast imaging with synchrotron radiation. This section addresses the design and fabrication of a thermoplastic breast immobilizer that I made from 3D-printed solid breast phantoms. This breast support is designed to be utilized in the patient table of the SYRMA-3D project at Elettra in order to potentially increase breast coverage while preventing patient movements during image acquisition.

4.2.1 Pendant breast geometry

In chapter 2 the simple geometrical models that simulate the shape of the breast under compression proposed by Dance (1990),Wu et al. (1991) and Boone (1999) for breast CT were

explained. Compressed and uncompressed breast shapes in a pendant geometry differ, and as the volume of the breast increases, so does its shape. In Monte Carlo breast dosimetry reports for bCT (Sechopoulos et al., 2010) the pendant breast is simulated as a semiellipsoid, which is more indicative of the pendant breast shape, however still model-driven.An investigation by Hernandez and Boone (2017) developed realistic breast-shaped phantoms for pendant-geometry in a different range of volumes and shapes using breast shape and size information of real dedicated bCT images. 6 diverse models, ranging from V1 to V6 according to breast volume, were developed as depicted in figure 4.1.
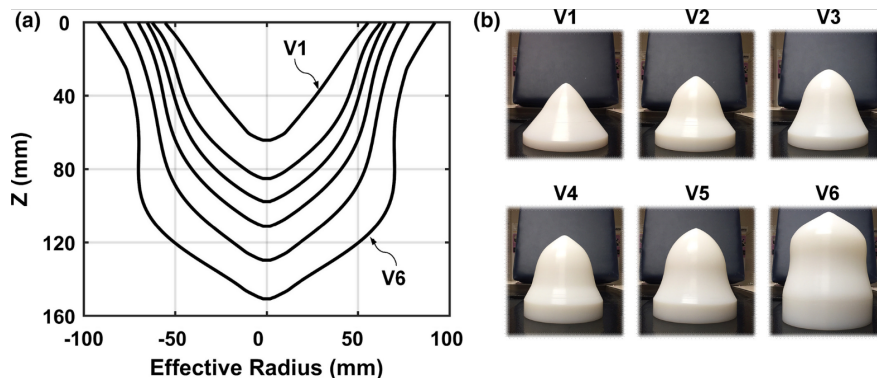
Figure 4.1: bCT data-derived physical phantoms of the study by Hernandez and Boone (2017).(a) Measured effective radius profiles for the VI–V6 phantoms. (b) Photographs of the V1–V6 phantoms fabricated with UHMW.

The phantoms of the study were also used as molds for the fabrication of thermoplastic immobilizers that could potentially help conform the breast to be centered in the field-of-view. Given the minimal thickness, low attenuation properties, and high porosity of the thermoplastic material, it is unlikely that the immobilizers will affect dose (Hernandez and Boone, 2017). The anatomical metrics and the corresponding radius profiles of the six breast phantoms created in this study were available to anyone interested in recreating these phantoms, therefore, they were used of my study.

4.2.2   3D printed breast models

My project proposal for the fabrication of thermoplastic breast immobilizer for PB-bCT was submitted to ICTP's Scientific fabrication laboratory FabLab (2023), an infrastructure devoted to creativity and research with special focus on possible applications of benefit for the society. After the acceptance of my breast immobilization project, I created the 3D models and their printing process was performed at ICTP's FabLab, which is detailed in the next paragraphs.

The software OpenSCAD (free software under the General Public License version 2) was

used for creating solid 3D CAD breast models, using the volume-classified breast data sets. The program Cura 3.0 (Ultimaker B.V, Utrecht, NL) was used as 3D printing software and a Robot-Factory 3DLPrinter was used to 3D-printing of the breast molds. The initial printed models were made with an semiellipsoid shape (Sechopoulos et al., 2010), with different heights and radius and a small cylinder on the center-bottom of the mold. The resulting models were too big (see 4.1) and the breast shape was model-driven, thus, not representative of a realistic pendant-geometry of the breast as seen in Fig. 4.2 (a). Therefore, following the work of Hernandez and Boone (2017), the volume-classified breast data sets in a pendant geometry was extracted for the creation of new 3D printed breast models. Specifically, the data of volumes 2 and 4 were used to create sample 3D printed models. The 3D printed breast molds were realistic for the pendant-geometry of the breast, however, as the data was based on U.S. population, the molds were too big (see fig. 4.2 (b)). A new batch, adjusted to smaller shapes and sizes from V1-V4 (Hernandez and Boone, 2017) models, was created (c). They were subsequently used for the creation of the second iteration of breast molds and thermoplastic immobilizers, that will be further explained in the next section. (d) shows the third iteration models that were created as a variation of volumes 1 and 2 of the second iteration. Table 4.1 shows the average metrics used for the printed breast molds. According to the breast mold size, the 3D printing times ranged from 6-16 hours per model.

4.2.3 Thermoplastic breast cups and immobilizing system

The thermoplastic immobilizer was fabricated using the 3D FORMING system by Robot Factory (see fig. 4.3), which was also available at ICTP's FabLab. Using a thermoforming technique, I created a breast holder (or breast cup) by pressing a heated 0.5-mm-thick sheet of thermoplastic material PETG (Polyethylene Terephthalate modified with Glycol) onto the 3D printed breast shaped mold. The air between the mold and the sheet is removed with an incorporated vacuum pump to perfectly adjust the sheet to the mold's shape. The result is seen in figure 4.3. On the left, an image of the 3D FORMING system is displayed while on the right, the finished thermoplastic breast cup with a small tube-form insertion placed on the center of the breast cup to accommodate the insertion of a connecting plastic tube. The transparent PETG sheet is protected by a removable blue film, that was left on for illustration purposes. The heat-malleable sheet is certified for the contact with food, therefore, was considered also safe to use in contact with the skin as well.

Therefore, the PETG breast cup was connected to small manual pump to create a vacuum
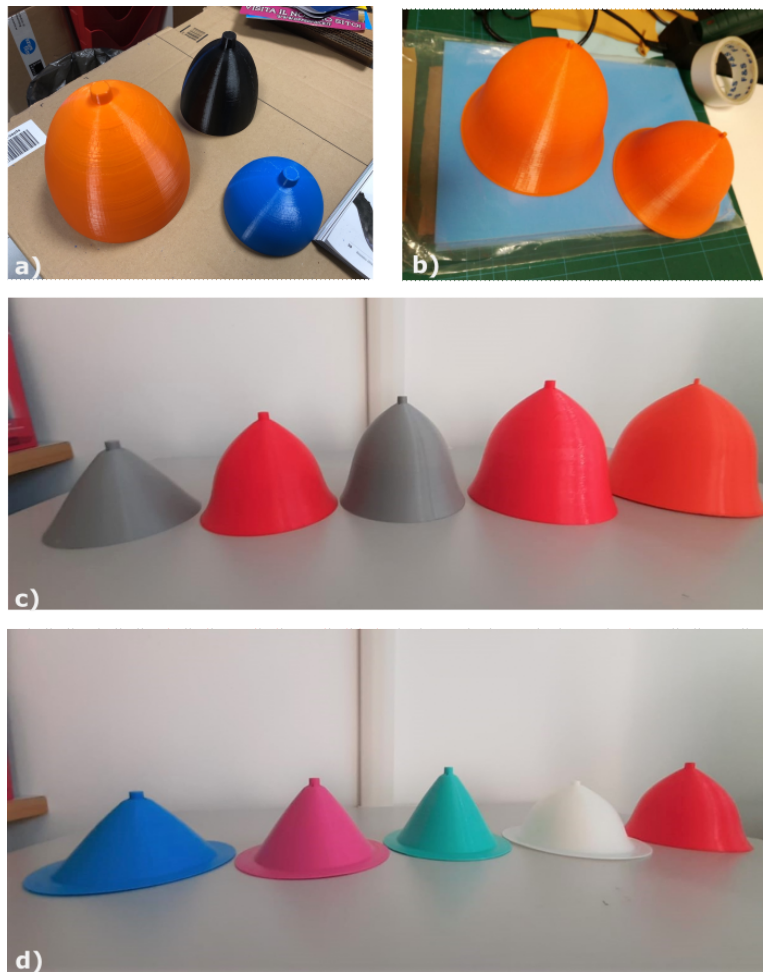
Figure 4.2: Examples of the different 3D printed breast shaped models. (a-b) initial printed models, (c) second and third iteration and (d) fourth iteration of breast models to use as molds for the thermoplastic immobilizers.
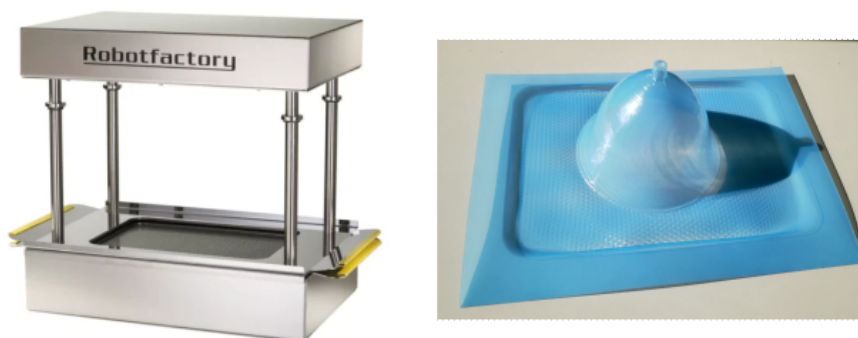
Figure 4.3: An image of the 3D FORMING system is displayed while on the right, the finished thermoplastic breast cup

between the breast holder and the breast, to potentially hold the breast in place. Figure 4.4 shows an image of the first breast immobilizer prototype.

	Length (mm)	$R_c w$ (mm)
1st iteration		
V1	70	50
V2	80	65
V3	110	50
V4	130	62.5
V5	140	75
2nd and 3rd iteration		
V1	64.3	51.7
V2	85.2	59.0
V3	64.3	62.7
V4	85.2	67.6
V5	85.2	75.2
Fourth iteration		
V1	65.8	47.5
V2	65.8	55.7
V3	65.8	62.3
V4	85.0	45.9
V5	85.0	61.2

Table 4.1: Anatomical metrics for the iterations of 3D printed breast-shaped molds. $R_c w$ is the average radius within the first 1 cm of the breast from the posterior edge.
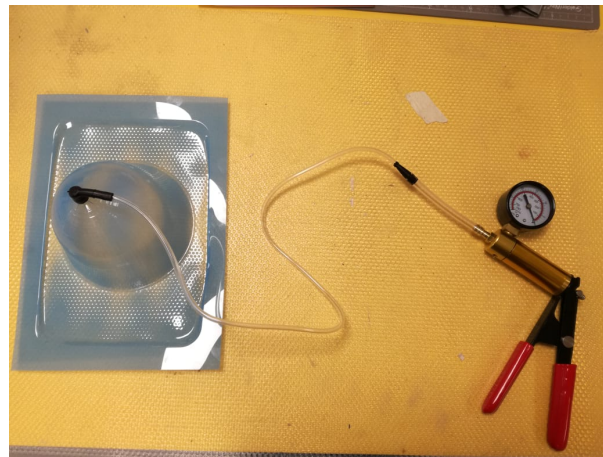
Figure 4.4: A photography of the finished thermoplastic breast immobilizer prototype. The blue protective film of the breast cup was kept for illustration purposes.

4.2.4 Prototype testing

I tested the breast immobilizer prototype system on 4 female volunteers to understand the strength and weaknesses of the system and determine the changes to perform in subsequent iterations. Subjects lied prone on the patient's tabletop, with a breast placed in the ergonomically designed aperture of the table, and the arms and head were positioned as in a clinical

examination setup. The breast cup closest to anatomical size of the participants was chosen. Under-pressure was generated using the manual pump either by creating the under-pressure by the examiner or by themselves. Pumping was stopped when discomfort was reported by the women. The testing was performed mainly: a) to determine the strength of the thermoplastic cups and evaluate any physical deformations caused by the under-pressure system; b) to verify the fixation of the device and evaluate the use of a sealing ring to ensure a fixation of the im-mobilization device to the skin; c) to identify how well the thermoplastic molded breast shapes adjusted to the volunteers and d) to rate the comfort of subjects while having the immobilizer and prevent pain while being subject to an under-pressure system for long times.

Results of the breast immobilizer prototype testing

First Iteration	
Strengths	**Weaknesses**
PETG keeps the mold's shape even after releasing the manual action of the pump Variety of cup holder sizes Low production cost PETG allows for robust cleaning	Some molds are too big for thermoforming PETG sheet's size Unrealistic ellipsoid shape
Actions	
Create new 3D printed models that are more representative of a realistic pendant-geometry.	

Second Iteration	
Strengths	**Weaknesses**
Underpressure held breast held in place Slow manual air-suction for patient's comfort Visibility of the positioning of the breast, even with the removable blue film on (see fig. 4.5) Cups can be disposable without having to undergo sterilization for re-use, thanks to its low production cost	Some volumes were still too big Holder deforms when the cup is larger than the breast size (fig.4.5). Suction causes discomfort around the nipple. Holder does not easily attach to skin Leakages around at the lateral chest and/or the sternum New pump users tend to squeeze the handle too strong, causing pain
Actions	
Change the of thermoplastic material to High Impact Polystyrene (HIPS), with sheets of 0.5 . mm and 1 mm thickness to avoid plastic deformation. New breast holders should be created with the 3D printed models of the 2nd iteration	
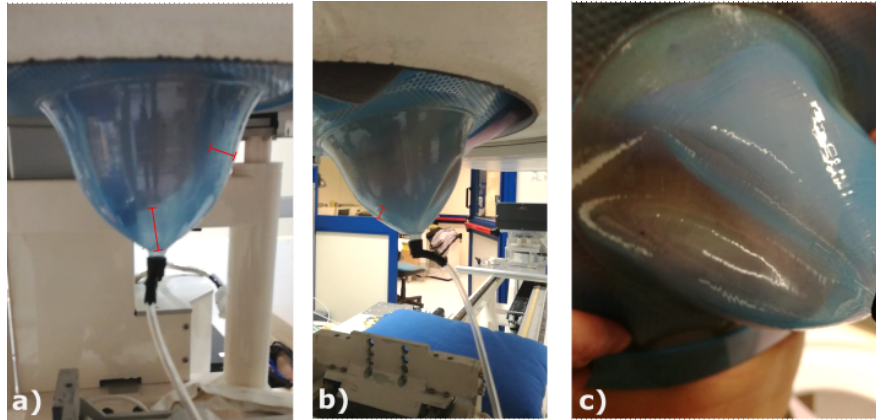
Figure 4.5: Deformation of thermoplastic breast cups when the breast is smaller than the breast holder. (a) shows slight/no deformation, (b) some deformation and (c) pronounced deformation. As more under-pressure needed to be applied to hold the cup in place due to the breast's smaller size, the more deformation that was produced (increasing from a-c). Red markers show and indication of the empty space within the breast cup.

Third Iteration	
Strengths	**Weaknesses**
Underpressure held breast held in place even after ending pumping	Holder deformation still persistant
	HIPS is not transparent (see fig. 4.6 (a).)
HIPS sheet of 1 mm are stronger, than PETG. No deformation of any cup.	Proper positioning undetermined due to the lack of visibility.
Under-pressure is better kept using 1 mm HIPS cups than with PETG cups	When using 0.5 mm sheets, the suction was still felt around nipple area, causing
The suction is more uniform when using 1 mm sheets, causing less discomfort	discomfort or pain.
HIPS sheets of 0.5 mm can substitute	Patient needs to hold the immobilizer with her hands for fixation.
PETG, if is not available.	Cups continue to be larger in size
Overall good comfort	than the tested breasts.

Actions

Create smaller 3D breast shaped molds modified to introduce a flange to the cups, to increase the area of fixation between the chest and the holder. Create thermoplastic cups using 0.5-mm-thick PETG and HIPS sheets. Adjust the size by cutting the sheet to the perimeter of the flange. Introduce the use of a syringe pump, instead of the manual pump to compare and contrast the underpressure fixation capacity.

Fourth Iteration

Five smaller 3D breast shaped molds and the PETG and HIPS breast holders were created a seen in fig. 4.6 (b). The use of a syringe pump, was introduced.
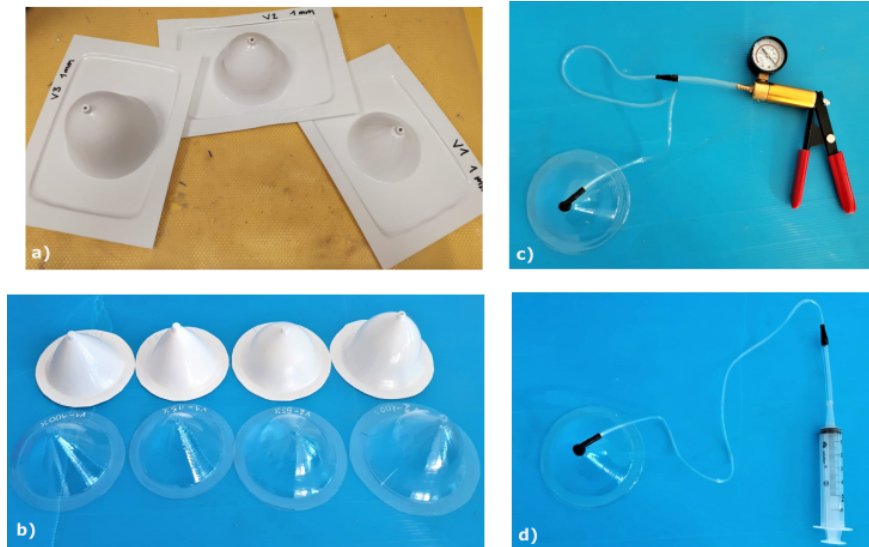
Figure 4.6: a)Third iteration 1-mm-thick HIPS breast cups and b) 0.5-mm-thick PETG and HIPS breast holders for the fourth iteration.

Due to the pandemic time, and the restrictions following it, the prototype of the fourth iteration could not been tested. Moreover, Elettra synchrotron is currently through a phase of updating their X-ray source to give rise to Elettra 2.0, for which the SYRMA-3D activities are temporarily suspended. It is, however, envisioned to continue with further projects and also with testing of this system, towards the clinical implementation of the PB-bCT in the new Elettra 2.0's SYRMEP beamline.

4.2.5   Italian-Australian collaboration

There is a long standing collaboration with the PB-bCT group at IMBL (IMP, 2023) in ANSTO Synchrotron in Australia. Both groups, at IMBL and SYRMEP beamlines respectively, are optimizing their imaging setups and technologies independently to ensure the best possible image quality towards the clinical applications of PB-bCT. At either synchrotron facility, imaging requires the patient to lie in prone position upon a dedicated imaging table see fig.4.7 while being rotated through the beam. Therefore, at IMBL, just at SYRMA-3D collaboration, the patient's motion issue was also of concern and the introduction of a breast immobilisation was given consideration after the SYRMA-3D's breast immobilizer initial results. Efforts from both research groups were joined to compare and contrast the prototypes developed in each group. The study was presented in the 15th International Workshop on Breast Imaging (IWBI 2020) and published in the proccedings found in Lewis et al. (2020).
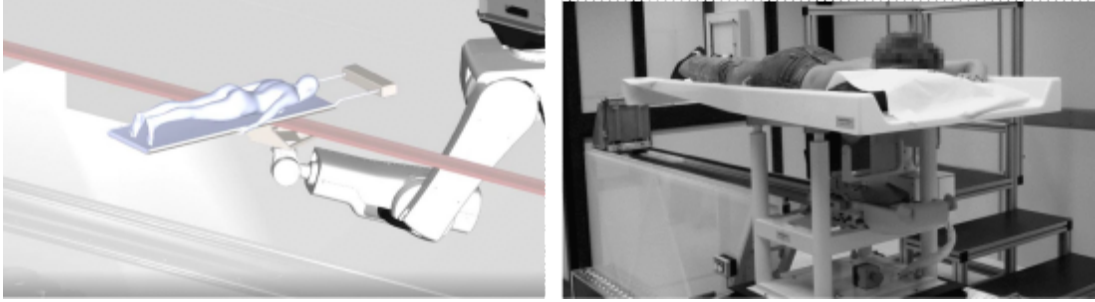
Figure 4.7: On the left, a simulation of the patient on the table movement during PCT. On the right, the patient support at the Italian synchrotron Image from Lewis et al. (2020).

4.2.5.1 Proposed designs

A number of proposed immobilization designs by both groups were carried out. A single-cup approach was adopted by both groups, while a double-cup was also developed by the Australian group.

Single Cup:

- A 1-mm thin commercial grade existing silicone cup, where a mastectomy sample was placed inside.

- 3D Breast Molds (3DBM): A designed PETG breast cup prototype (see fig. 4.4 that was created by a thermoplastic 3D forming system and tested on female participants at the Italian group (corresponding to the second iteration of the previously explained breast immobilizers 4.2.4. An relevant result from the testing was the importance of a close fit to the breast holder to prevent air gaps and distortion of the plastic when the breast did not fill the volume and suction was applied.

Double Cup:

- Double-Cup-Spot (DCS) immobilization system made of 3D-printed PETG cups that include multiple holes around the circumference of the breast to allow symmetrical distribution of the suction force from the pump and outer cup (see image 4.8). The modular design of double cups should allow for switching components for custom sizing and replacing components as needed. The testing on females with this prototype had not been carried out at the study date in 2020, as it was not yet manufactured due to the pandemic. However, it was recently created and tested, and the results can be found in Dimmock et al. (2022).
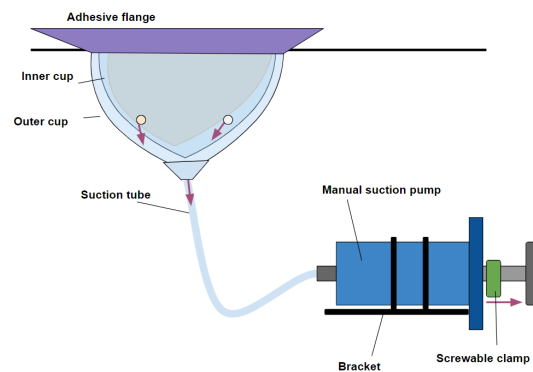
Figure 4.8: The Double Cup-Spot (DCS) design specifications. Image from Lewis et al. (2020).

4.2.5.2   PB-bCT imaging

PB-bCT imaging was carried out for each single-cup design in their corresponding synchrotron facilities at their proposed clinical protocols. The 1-mm thick silicone cup was imaged at IMBL with a mastectomy sample at 32 keV with fig. 4.9(a) a rubber holder and (b) without the rubber holder. The PETG cup was acquired at Elettra at 35 keV with a surgical glove containing water as tissue-equivalent material.
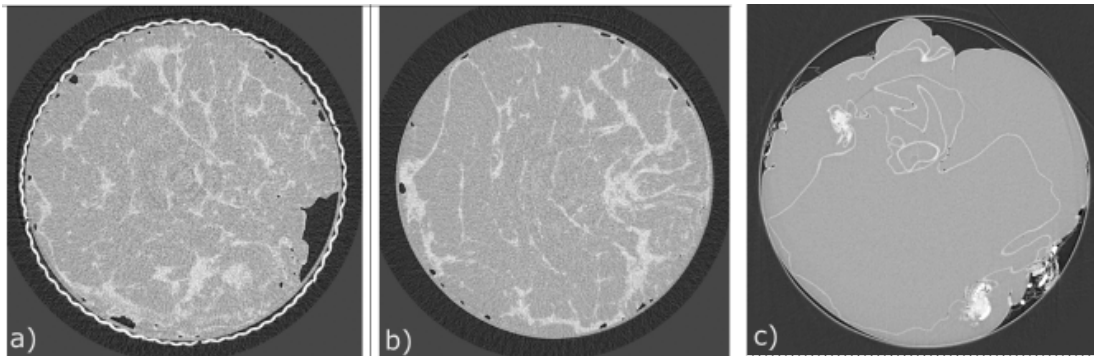
Figure 4.9: PB-bCT images of the immobilization prototype designs. (a) Silicone cup with a mastectomy sample acquired at 32 keV with (a) a rubber holder, (b) without the rubber holder. c) PETG cup with a surgical glove with water imaged at 32 keV. Images adapted from Lewis et al. (2020)

Even though no quantitative assessment was carried out, the visual assessment of the images show that the PETG cup has a negligible impact on either the beam attenuation or phase retrieval. Moreover, the implementation of a PET cup holder does not create image artifacts either. These are significant findings because they provide image quality benchmarks for future breast support device modifications. The use of a breast support device should not jeopardize the health and safety of the patients, such as causing significant discomfort or causing injuries due to the application of excessive suction or ill-fitting holders to the breast. This joint study

showed that further modifications for a better development of a breast support should also consider quantitative parameters, such as the measurement of an acceptable SNR at a dose comparable with standard DM. The implementation of a breast immobilization device with PETG cup holders in an underpressure system shows promising benefits. To prevent breast motions during image acquisition, breast imaging facilities that use a free breast pendant geometry could benefit from the adoption of a breast immobilization device with PETG cup holders in an underpressure system. However, more research on the impact of patient motion —whether voluntary or involuntary— on reconstructed tomographic images is needed. Therefore, a research to examine the impacts of patient motion and a correction method was developed within the SYRMA-3D collaboration; its specifics are described in the next section.

4.3 Motion artifact assessment and correction

Motion artifacts are a common issue in medical imaging that can lead to degraded image quality and inaccurate diagnosis, which can be particularly challenging due to the rotation motion of the pendant breast and the breathing of the patient during PB-bCT imaging. The need to investigate the impact and to compensate the possible artifacts risen from such motions on reconstructed PB-bCT images lead to an investigation in the framework of SYRMA-3D collaboration. The investigation, which was published by Brombal et al. (2021) and I am a co-author of the work, was developed for three main purposes: first, to develop a simple model for the respiratory motion by evaluating real breathing displacements on seven volunteers with an optical tracking method. Second, to evaluate the effect of such modeled motion on reconstructed tomographic images of a breast phantom and a surgical specimen. Third, to introduce a correction method using an external optical motion tracking method to compensate for the resulting artifacts. In addition to taking part in the development of the experimental set-up, carrying out tomographic acquisitions, and post-processing of the images, my own contribution included the development of motion correction algorithms. As the study encompassed three inter-connected purposes, each section was carried out with different methodologies, for which each will be explained separately.

4.3.1 Intrinsic motion correction algorithms

Initial attempts to correct intrinsic motion compensation without the aid of any external motion measurements were carried out using image registration algorithms with MATLAB codes developed by the author. A motion-affected virtual dataset was simulated by randomly shift-

ing motion-free images in order to test different algorithm to attempt compensating the motion without the aid of a tracking/gating device. The correction algorithms involved using the first projection as reference "static" image, and the subsequent slice as the "moving" image. One of the proposed algorithms used the cross-correlation method to compensate for motions in the virtual dataset. The methodology located the maximum value in each image (static and moving). Then, to estimate the distance between the "moving" image peak and the reference peak, the cross-correlation function between the two images was applied. By knowing this distance, a shift corresponding to the previous distance was applied through an image registration and the motion was compensated. The same procedure was applied to the following images. However, the corrected image was based on the position of a reference image, but the next image was corrected on the shifts form the precedent corrected image as well. Therefore, the information in the dataset slowly shifted, and at a certain point the corrections method was shifted in a way that was not true to the expected compensation method. Other similar methods were also applied with similar results. The approach of not incorporating external motion measurements revealed certain issues:

- the motion was estimated from an arbitrary reference image, which was not clearly established as a static image, or a true motion-less image, to be classified as a reference.

- the algorithm considered a previously corrected slice, as the new reference value for the following motion compensation, therefore, any miscorrected image affected the complete dataset.

- the peaks can be affected by noisy data, which in turn, affect the accuracy of the registration.

- the method did not take account the periodicity of the respiratory movements

The definition of the motion estimation step along the complete dataset seemed the main difficulty for an intrinsic motion compensation method.

Within the context of analyzing the effect of breathing in breast imaging in a prone position, a previous patient study by Roessler et al. (2015) demonstrated the significance of proper patient placement and the considerable impact of patient breathing on breast coverage. It demonstrated using an optical measurement system that the breast volume can significantly increase during exhalation in a pendant geometry (by a 4%), in comparison with normal breathing, potentially leading to motion distortions in the reconstructed images that can affect the

diagnostic accuracy. Within this context and my preliminary results on the intrinsic motion correction algorithms, the investigation was set to incorporate an approach using external motion measurement instead of an intrinsic motion compensation method, for which an external optical motion tracking technique was used.

4.3.2 Development of a respiratory motion model

A preliminary assessment was performed on seven female volunteers who were not exposed to x-rays and were simply asked to lie prone on the ergonomically designed, high-precision support in the patient's position and place their left breast in the central aperture in a pendant geometry to evaluate the patient's real breathing motion. The patient table previously used for the SR PhC mammography trial and compatibile with the bCT, as mentioned in section 3.2.1, can rotate around the vertical axis as well as translate horizontally and vertically (see figure 3.1.

The left breast was chosen because it was thought to be more directly affected by involuntary heartbeat movements. To help track the patient's movements, a fiducial mark with a fine pen black dot was applied on a white band, that was placed on the pendant breast of each volunteer. Images of this fiducial mark were taken with an optical camera (Basler acA1920-155um equipped with a Kowa LM25HC 25 mm lens with an F 1.4-16 iris range) placed at the same height as the fiducial mark and about 50 cm away from the sample. 400 frames of the fiducial mark were recorded in 40 seconds (10 Hz frame rate), which corresponds to the expect duration of a single bCT scan at SYRMEP. The volunteers were told to breathe normally. For each frame in the images, a mask corresponding to the fiducial mark was obtained, and its position was determined by calculating the center of mass (CoM) coordinates of the masked pixels. A reference image was used to perform a millimetric unit calibration. The fiducial mark movements were assumed to yield a rough estimate of a typical patient's breast movement. According to the seven participants' recorded motions, average oscillations were found between 0.2 and 0.5 millimeters in the horizontal direction and between 0.4 and 1.0 millimeters in the vertical direction with a frequency ranging from 9 to 18 cycles/minute. These preliminary results were used to model the respiratory motion during a PB-bCT tomographic acquisition. As vertical oscillations dominated over horizontal ones, only a vertical motion breathing model was developed.

4.3.3 Respiratory motion simulation

The respiratory motion was modelled as a periodic oscillatory vertical motion with a constant speed, an amplitude of 1 mm, and a frequency of 12 cycles/minute. For the experimental set-up, samples need to be mounted on a high-precision rotator (Micos UPR-160 Air), mounted on a programmable six-degree-of-freedom hexapod positioning stage (Physik Instrumente H-840.G2) visible in figure 4.10 and fig. 4.11. Therefore, the respiratory model was programmed on the hexapod positioning stage and superimposed upon the sample rotation to simulate breathing-induced oscillations. In this way, at the moment of tomographic acquisitions, the breast samples would follow a breathing pattern, as do patients, and the effect of such modeled motion on reconstructed tomographic could be studied. To monitor the modelled motion, motor positions were logged at a rate of 30 Hz, ensuring a good match with the sampling of tomographic projections.
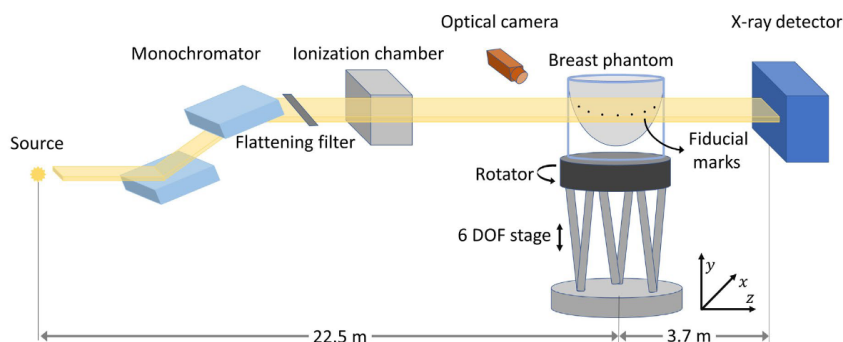
Figure 4.10: Sketch of the experimental setup carried out in this study. From Brombal et al. (2021).

4.3.4 Tomographic imaging

The standard experimental Pb-bCT SYRMA-3D setup at the SYRMEP beamline was used. In this study, a surgical breast specimen with a moderate grade ductal infiltrating carcinoma and a multi-modality breast phantom (CIRS model 073) were scanned at 28 keV at an entrance air kerma of 10 mGy, corresponding to an MGD of 5 mGy, values comparable to those used in clinical practice. The samples were mounted on the rotator that spins at 4.5 degrees per second, mounted on the hexapod stage programmed with the vertical respiratory motion model4.10. PIXIRAD-8 detector was set at a distance of to 3.7 m away from the sample. 1200 evenly spaced projections over 180° were acquired in continuous rotation at a rate of 30 Hz. Images followed the usual pre-processing procedure (Brombal et al., 2018a) and phase-retrieval (Brombal et al., 2018c).

The scanned breast sample was formalin-fixed and sealed in a vacuum bag. The sam-

ple was handled following the Directive 2004/23/EC of the European Parliament and of the Council of 31 March 2004 on setting standards of quality and safety for the donation, procurement, testing, processing, preservation, storage, and distribution of human tissues. Imaging was performed within the framework of the operative protocol of the Breast Unit of the Trieste University Hospital. The scanned phantom mimics a breast with the presence of cystic dense lesions embedded in a homogeneous background and contains several microcalcifications with diameters ranging between 100 and 300 μm. To simulate a PB-bCT examination, the phantom was imaged in a pendant geometry, as seen in figure 4.11, where equally spaced fiducial marks were applied on the surface of the breast phantom.
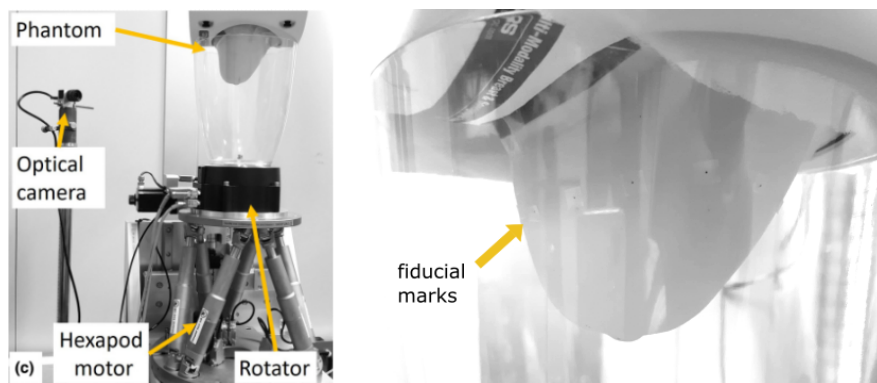
Figure 4.11: Setup for the optical tracking method, showing the rotator and the hexapod sample stage, as well as the camera used for tracking the fiducial marks on the breast phantom. On the left, a zoom of the breast phantom with the fiducial marks. Image adapted from Brombal et al. (2021).

4.3.5 Optical tracking method

To monitor the displacement brought on by the rotating stage's vertical respiratory model, fiducial markers were placed only on the pendent breast phantom. For the breast specimen sample, no optical tracking procedure was implemented due to its rather unrealistic surface shape and volume, and to the presence of the vacuum bag wrapping the specimen. The earlier mentioned optical camera setup, that was employed with the seven participants, was used to image the fiducial marks during the tomographic acquisition (see 4.11. Here, the optical camera was positioned 50 cm away from the sample and perpendicular to the direction of x-ray propagation (z), at the same height as the fiducial markers. The frame rate of the camera was set to 30 Hz to match the x-ray detector's frame rate, while its gain was optimized to ensure the best visibility of the fiducial marks used for tracking. As opposed to the volunteers' preliminary motion estimation, the displacements were measured by following a series of consecutive fiducial

markings on the breast during rotation. Using a calibration factor, the tracked displacements were then converted from pixels to millimeters. This distance would later be used to apply the in correction method.

4.3.6   Motion correction and reconstruction

Prior reconstruction, phase-retrieved projections needed to be corrected for the modelled vertical breathing motion, as not doing so would result in the appearance of motion artifacts in the reconstructed images that can compromise their diagnostic quality. The motion correction method was performed using MATLAB (The MathWorks, Inc., Natick, MA, United States) codes (some that were developed during this thesis work). The correction was performed by a linear registration based on translations to align the moved projection to the corresponding static position. The translation vector was defined slightly different for the breast specimen than for the breast phantom

- *Breast specimen*: projections were corrected based on the actual motor position tracks. As motor positions were logged, the displacements, corresponding to the translation vector to be applied, were known.

- *Breast phantom:* phantom projections were corrected according to the positions from the tracked displacements using the optical tracking method. The positions were converted to distances through the calibration factors and were later used for the translation vector

Once the projections were translated to compensate for the vertical motion imposed during the acquisition, each dataset was finally reconstructed via a GPU-based FBP and Shepp-Logan filtering (Brun et al., 2017).

4.3.7   Impact of motions on bCT images

To investigate the impact of motion artifacts on reconstructed images, datasets with varying displacements were virtually simulated by leaving certain residual motion from translation vector in the motion correction step. The virtual simulation kept vertical displacements of 0.05, 0.1, 0.2, 0.5, and 1 mm. Figure 4.12 depicts a single detail with a spiculated fibroglandular tissue component (bright) embedded in an adipose background (dark) and a sharp interface between tissue and air (black) that is reconstructed with different virtual displacements as shown in the insets. In panel (a), the image is precisely reconstructed while compensating for the known motor movements; thus, the motion is completely corrected and the virtual displacement is 0.0 mm. On the other hand, reconstructions in panels (b) to (e) include a virtual displacement of

0.05, 0.1, 0.2, and 0.5 mm, respectively, whereas in panel (f), no motion compensation is used and the displacement of 1 mm corresponds to the breathing motion model. When no motion correction is applied, the fibroglandular component is severely blurred and the visibility of connections is almost entirely lost (see image f). Furthermore, artifacts at the sample's boundary (red arrow) impair visibility of the surrounding region and, more importantly, propagate within the tissue, lowering overall image quality. Similar considerations apply to the 0.5 mm motion amplitude, and ad 0.2 mm the artifacts become much less severe but still visible.

For residual displacements of 0.1 and 0.05 mm, the differences with respect to the fully corrected image are almost negligible as the amount of residual motion is smaller than, or comparable to, the system's spatial resolution (i.e., $\sim$0.1 mm at FWHM of the point spread function), suggesting that these motions can be tolerated as they do not affect image quality. On the other hand, for motions larger than 0.2 mm, the motion artifacts are critical and impact on image quality.

Figure 4.13 shows a detail of the breast phantom with one of the simulated cystic lesions embedded in a breast tissue equivalent background. The lesion contains several microcalcifications, and an air cavity can be seen in its periphery. Despite the fact that the latter feature is not present in a real breast, it is useful in determining the quality of the optical tracking correction because high-contrast interfaces (e.g., air/tissue) are sensitive to small displacements. Panels (a) through (d) depict the reconstruction as corrected using various methodologies. The reconstruction in panel a) is the static reference dataset, the image in panel b) was corrected with the actual motor positions, the image in panel c) was corrected with the optical tracking method, and the image in panel d) was not corrected.

To determine how far the optical tracking is from the ideal motion-compensated dataset, a correction based on motor positions—which is obviously not practical in a clinical setting when the patient is moving freely—was done. The figures show that the visibility of the microcalcifications is compromised if no motion correction is used (d) due to the degree of blurring created in the final reconstruction. In contrast, the optical tracking method (c) produces an image that is comparable to the perfectly adjusted displacement (b), restoring both the sharpness of the interfaces and the visibility of the calcification. The line profiles measured across a microcalcification (indicated by the arrows) in panels (e) to (h) further illustrate this. In particular, it is demonstrated that the optical tracking greatly aids in the recovery of the microcalcification signal while its sharpness, as measured by Gaussian fitting ($0.20 \pm 0.02mm$ at FWHM),
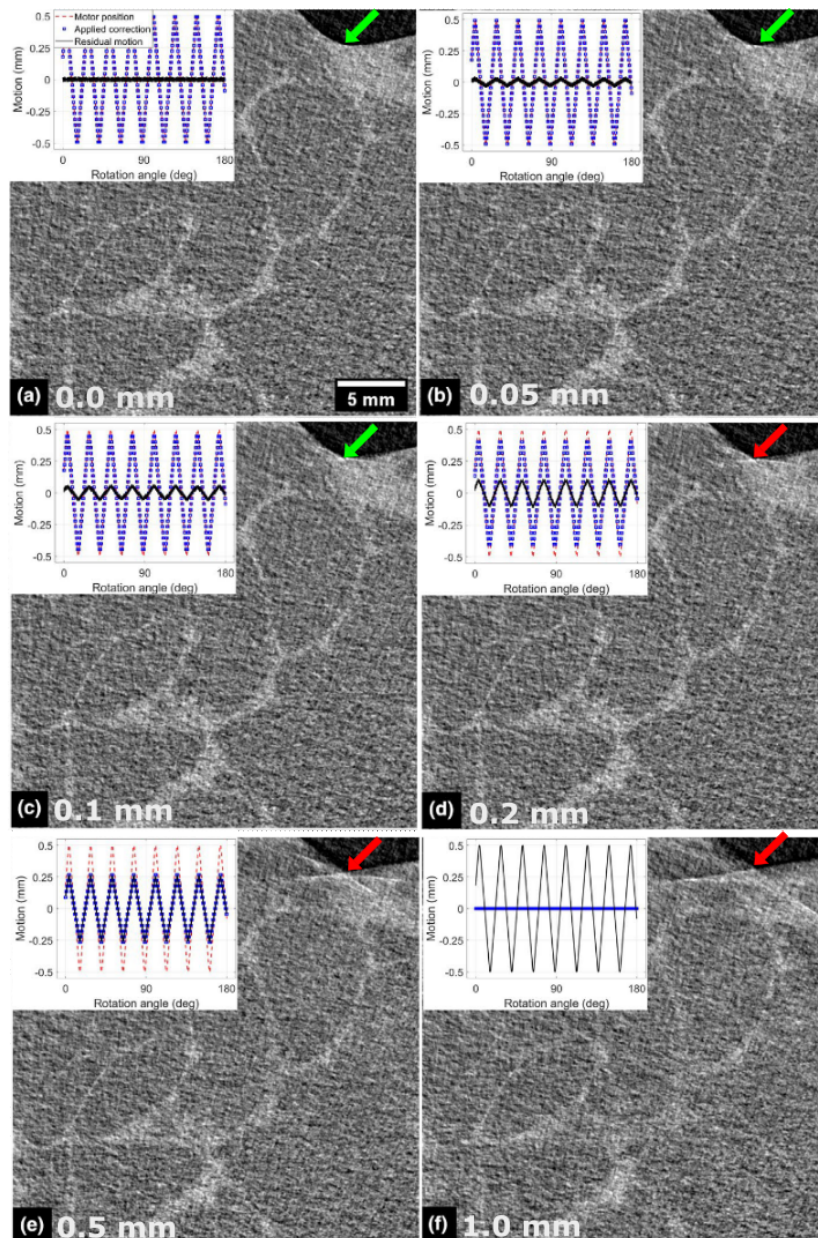
Figure 4.12: Detail of the breast specimen sample reconstructed and corrected for the vertical motion. The inset in each panel shows the actual motor positions (red dashed line), the applied correction for each projection (blue points), and the residual motion (solid black line). The residual motion corresponds to the virtual simulated displacement in a) 0.0 mm b)0.05 mm, c)0.1 mm d) 0.2 mm e)0.5 mm f)1 mm. The arrows correspond to motion artifacts (green when is negligible, red when is severe). Image adapted from Brombal et al. (2021).

is comparable to both the motor corrected and the reference static cases. If the image is not compensated, on the other hand, the microcalcification signal is similar to image noise.

The results show that characteristics such as spiculations and microcalcifications, which are critical in the clinical interpretation of bCT images, become significantly less visible at vertical respiration displacements in the mm range. In particular, oscillations with a realistic
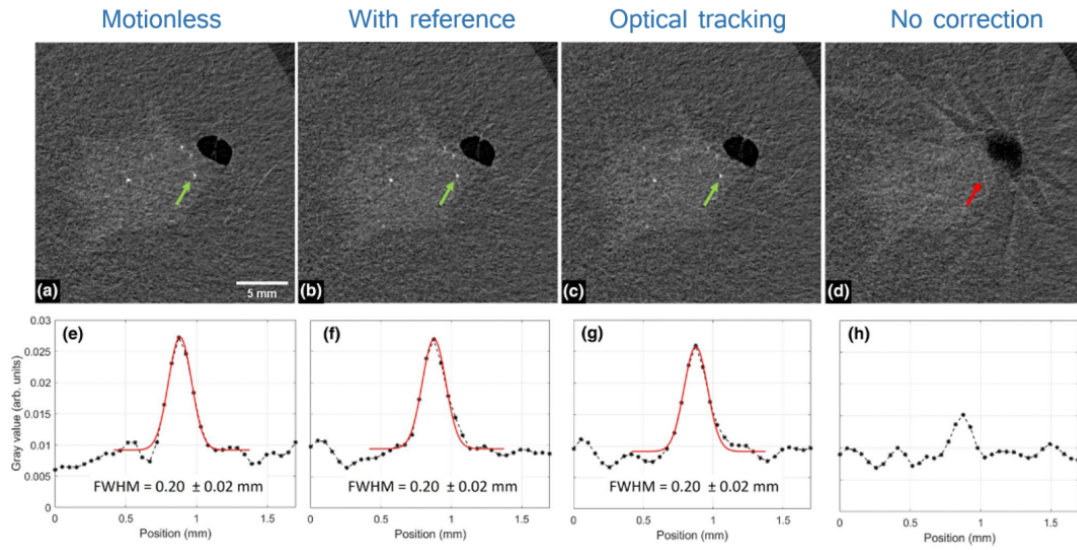
Figure 4.13: Reconstructed image of the breast phantom with a microcalcification indicated with the arrow (green when visible and red when not visible). Corrections for the vertical motions were performed with: a) a reference motionless dataset (b), the actual motor positions (c), the optical tracking procedure (d), no correction (d). In panels (e) to (h), the line profiles (black dots) and Gaussian fit (red line) across the microcalcification showing its visibility, are displayed. Image adapted from Brombal et al. (2021).

amplitude of 1 mm degrade image quality by hiding the microcalcifications, distorting the fibroglandular texture, and causing significant blurring. One to three respiratory cycles can be captured by a standard 10 s long scan, which is roughly the length of a traditional bCT examination. As a result, it may be argued that hospital-bCT systems are also susceptible to motion artifacts brought on by unintentional patient's movement, which could result in a loss of features' visibility that would otherwise be resolved.

For synchrotron-based settings, the employment of techniques to prevent, such as the introduction of a breast immobilizer, and to correct for involuntary motion, such as the present methodology, appears to be required. Novel functional breast imaging techniques in hospital-bCT settings, such as 4D bCT, which has a longer duration scans than conventional bCT (Uhlig et al., 2019; Caballo et al., 2019), might also benefit from the for motion prevention and reduction proposed techniques of this thesis work.

4.4 Optimization of a customized Reconstruction algorithm

Another important step to ensure the best possible image quality towards the clinical application of PB-bCT is the optimization of the currently used reconstruction algorithm. IR algorithms combined with edge-preserving filters are attracting the interest of researchers in the

field of biomedical X-ray imaging (Löve et al., 2013; Nishiyama et al., 2016). When compared to FBP, the use of such algorithms often results in better reconstruction quality . Iterative reconstruction algorithms commonly involve reducing image noise or, more accurately, increasing the contrast-to-noise ratio while preserving image detail (Gervaise et al., 2012; Willemink et al., 2013; Greffier et al., 2015). They, on the other hand, change the shape of the noise power spectrum, resulting in a shift towards lower spatial frequencies with respect to FBP. As a result, the reconstructed images have a "patchy" or "waxy" appearance. This type of image texture influences the radiologists' perception of image quality, which may influence their willingness to use an iterative algorithm in clinical practice.

Simultaneous algebraic reconstruction techniques (SART) (Kak et al., 2002) generally ensure fast convergence and flexibility, when compared to other iterative algorithms, allowing for the implementation of custom modifications. It is easily parallelizable on GPU and is typically associated with noise reduction while preserving the sharpness of edges and interfaces. Consequently, the SYRMA-3D collaboration developed a dedicated SART algorithm making use of a 3D bilateral regularization filter during the iterative process (Golosio et al., 2004; Oliva et al., 2017). Initial results from the study by Donato et al. (2019a) show that the implementation of such dedicated SART in the specific application on breast specimens, combined with the bilateral filter, can be tuned to preserve the noise texture and spatial resolution observed in FBP reconstructions, while improving contrast-to-noise ratio up to 30%. In this context, a custom-made GPU-based simultaneous algebraic reconstruction technique (cSART) in conjunction with a 3D bilateral regularization filter, to be tuned to yield optimal performance for clinical image visualization and tissues segmentation, was investigated. The effect of tuning of three independent parameters on NPS, spatial resolution, and contrast-to-noise ratio (CNR) is discussed here, and the optimal combinations of parameters preserving image texture for the PhC-bCT system are identified . Some of the contents presented in the following sections have been published in Donato et al. (2019b) and in Donato et al. (2022b), where I was co-author of the paper and participated in the reconstruction and post-processing of the acquired images in both studieI was a co-author..

4.4.1   Experimental design

Two cases were used for the optimization study: a breast mastectomy with a differentiated infiltrating ductal carcinoma fixed in formalin and sealed in a vacuum bag, and a bCT dedicated test object (Contillo et al., 2018) with materials that mimic the attenuation and contrast of breast

tissues. The test object's design allows imaging the plastic rods, for CNR and spatial resolution measurements, and the uniform water background, located at a different vertical position, for NPS evaluation.

The scans were carried out at the SYRMEP beamline according to the previously discussed SYRMA-3D PB-bCT setup (ch. 3). In this experiment, PIXIRAD-8 detector was set at a distance of to 1.6 m away from the sample. 1200 evenly spaced projections over 180° were acquired in continuous rotation at a rate of 30 Hz. The beam's energy was set to 32 keV while its intensity was adjusted by means of aluminum filters to deliver a total MGD of 5 mGy. Images followed the usual pre-processing procedure (Brombal et al., 2018a) and phase-retrieval (Brombal et al., 2018c) at a δ/β corresponding to ICRU-44 ICR (1989) to the breast tissue/air interface at 32 keV. Phase-retrieved projections were reconstructed using three methods: a) a GPU-based FBP and Shepp-Logan filtering (Brun et al., 2017), b) a standard SART with 5 iterations, and c) the cSART algorithm. To optimize the cSART parameters, images were reconstructed with different combinations of the algorithm's parameters. For the purposes of this thesis, the results of the clinical image visualization of the breast sample will be discussed.

4.4.2 The cSART algorithm

The iterative corrections were weighed with a relaxation factor and a bilateral 3D filter was applied periodically to the reconstructed image guess during the iterative process as a regularization factors (Golosio et al., 2004; Oliva et al., 2017). In the filter, the content of each pixel was replaced with a weighted average accounting for both the (3D) Euclidean distance and the gray-level difference of neighboring pixels.

The weighting kernel of the pixel identified with indices i'_x, i'_y, i'_z in filtering the pixel i_x, i_y, i_z is:

$$K(i'_x, i'_y, i'_z; i_x, i_y, i_z) = \exp\left[-\frac{(i'_x - i_x)^2 + (i'_y - i_y)^2}{2\sigma_{xy}^2} \cdots \right.$$
$$\left. -\frac{(i'_z - i_z)^2}{2\sigma_z^2} - \frac{(F(i'_x, i'_y, i'_z) - F(i_x, i_y, i_z))^2}{2\sigma_v^2} \right]$$

(4.1)

where σ_{xy}, σ_z and σ_v are parameters related to the spatial width of the filter in the horizontal plane, in vertical direction, and in content difference, respectively. $F(i'_x, i'_y, i'_z)$ and $F(i_x, i_y, i_z)$ are the contents of the pixels i'_x, i'_y, i'_z and i_x, i_y, i_z respectively, where x and y are the spatial coordinates in each projection image and z is the projection index.

To optimize the cSART, images were reconstructed with different combinations of the algorithm's parameters, by varying $\sigma_{xy} = \sigma_z$ in the range $[2:7]$ pixels with a step of 1 pixel, σ_v in the range $[0.004:0.014]$ with step of 0.002 and w in the range $[0.04:0.16]$ with step of 0.02, corresponding to a total of 252 reconstructions. 5 iterations were carried out, consistently with the standard SART reconstructions, while the regularization filter was applied every 100 randomly ordered angular steps.

4.4.3   Quantitative assessment

Reconstructed images with FBP algorithm were assumed as a reference, to compare against the standard SART and cSART images. Images were analyzed through dedicated MATLAB (The MathWorks, Inc., Natick, MA, United States) codes. Contrast-to-noise-ratio (CNR), spatial resolution and image texture, were analyzed as indicated by the regions-of-interest (ROI) in figure 4.14. In this thesis work, only the results of CNR will be discussed and their relation to the qualitative comparison that was carried out.

Contrast-to-noise-ratio was evaluated by using the following definition:

$$CNR = \frac{\overline{I_d} - \overline{I_b}}{\sqrt{(\sigma_d{}^2 + \sigma_b{}^2)/2}} \tag{4.2}$$

where I_d and I_b are the average pixel intensities of the glandular detail (d) and the adipose background (b), while σ_d and σ_b are the respective standard deviations (noise). CNR was computed as the average CNR value of three pairs of square ROIs selected.
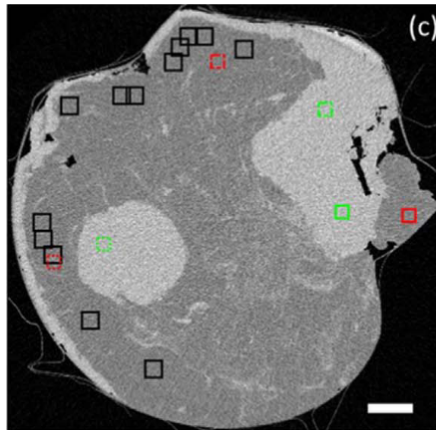
Figure 4.14: Representation on the regions used in the breast tissue reconstruction to carry out the quantitative assessment. Black squares represent the ROIs used to evaluate the NPS, while for CNR the green squares where used as detail and the red squares as background. Scalebar = 10 mm. taken from Donato et al. (2019a).

A qualitative comparison of a tumor detail of the breast sample is shown in figure 4.15

reconstructed with FBP, SART, cSART (within and out from the threshold condition) at 5 mGy dose. The images reconstructed with the different algorithms (b-e) were compared to the the reference FBP image (a) acquired at high radiation dose (50 mGy). For cSART within the threshold condition (d) the parameters were $\sigma_{xy,z} = 2$, $\sigma_v = 0.008$ and $w = 0.06$ and out from the threshold condition (e) they were $\sigma_{xy,z} = 7$, $\sigma_v = 0.014$ and $w = 0.08$. Refering to fig. 4.15, a 3-fold decrease in CNR was observed when images were reconstructed using FBP from high (a), with CNR of 9.2, to low dose (b), CNR of 3.1, as expected from the photon statistics. The use of conventional SART (c), on the other hand, showed no advantage over FBP in terms of image quality, whereas the cSART image satisfying the threshold criterion (d) had a higher CNR (4.2), similar texture, and no apparent spatial resolution degradation. Increasing the cSART parameters, as shown in (e), resulted in an image with the same CNR as the reference high dose image (CNR = 9.2) at the expense of increased patchiness.
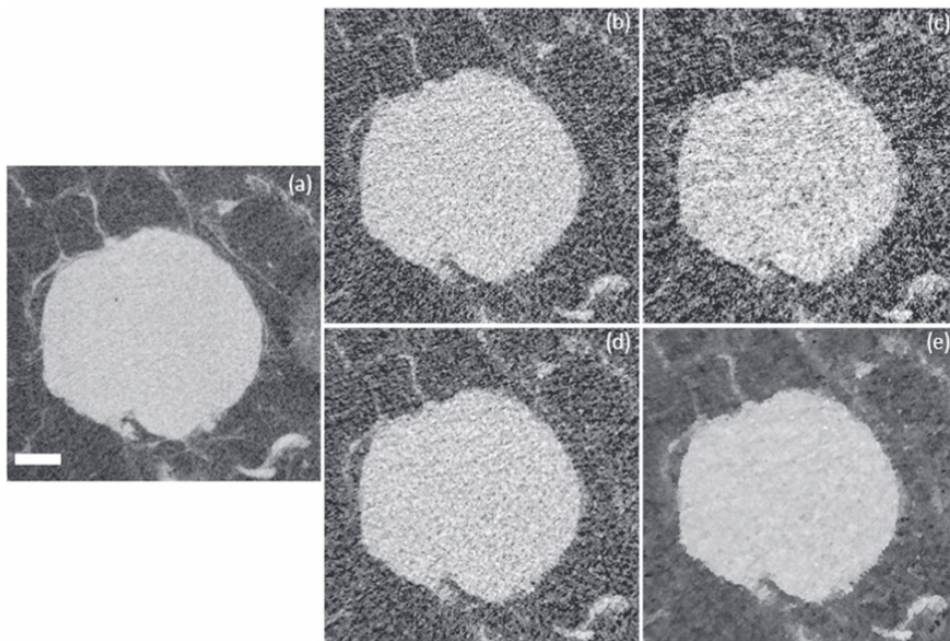
Figure 4.15: A visual comparison of a breast sample detail depicting a tumor mass (light gray) in an adipose background (dark gray) reconstructed with different algorithms: a) FBP at 50 mGy (ground truth), b) FBP at 5 mGy, c)SART at 5 mGy, d) cSART within the threshold condition at 5mGy, d) cSART out from the threshold condition at 5mGy. Scalebar = 5 mm. Image from Donato et al. (2019a).

According to these findings, dedicated iterative reconstruction techniques could provide significant benefits in phase-contrast bCT imaging using free-space propagation and phase-retrieval. The customized GPU-based SART algorithm provides a high degree of flexibility in

image reconstruction optimization for diagnostic evaluation, with either a limited gain in CNR and textural properties similar to FBP, or with a major gain in CNR (by a factor of 3 or more) at cost of increased image patchiness.

The clinical significance of the proposed cSART algorithm's improvements will be assessed in a follow-up visual assessment study performed by qualified readers in collaboration with the IMBL's PB-bCT research group at the Australian synchrotron.

4.5   Radiological Assessment

As part of the collaboration with ANSTO Synchrotron in Australia, a study to evaluate the visual-grading performance of the detectors used in synchrotron radiation PB-bCT breast imaging was also carried out. Six mastectomy specimens were scanned at the IMBL using a Hamamatsu C10900D Flat Panel detector and three mastectomy specimens were scanned at the SYREMP beamline using PIXIRAD-8 CdTe single-photon-counting detector according to the previously discussed setup (ch.   3). It should be mentioned that different mastectomies scans were performed at each location in order to replicate the same experiment with the similar scanning settings because mastectomy specimens cannot be transported. This investigation was carried out at the most effective but separate configurations for each beamline, as summarized in table 4.2, rather than matching the experimental conditions. SR absorption-based CT (AB-CT) reference images and PB-bCT images under various imaging settings were compared. The image quality improvement delivered by PB-bCT relative to AB-CT was investigated using a visual grading characteristics (VGC) study, where eleven experienced readers evaluated the visual image quality of the various image sets. Although the slices acquired at SYRMEP are 60 μm thick, the slices for the visual grading assessment were prepared to have a 1 mm thickness in order to be comparable to the slices acquired at the Australian synchrotron facility. My contribution of this thesis to this study encompassed only the activities carried out at the SYRMEP beamline, where I participated in the data collection during the beamtime, as well as in the image reconstruction and post-processing of the acquired images.

Image analysis was carried out on dedicated workstations for breast imaging. Each expert was asked to compare the PB-bCT image quality to reference AB-CT images from the same sample. The image attributes' rating scored the perceptible contrast in various soft tissue regions, the clarity of definition of lesions and spiculations, the clarity of visualisation of interfaces between fatty and fibroglandular tissues, the calcification visibility (if present), the presence of quantum mottle in the image (image noise), and the evidence of any artifacts such

	SYRMEP beamline	**IMBL beamline**
Detector	CdTe Photon-counting	Flat panel
Pixel size (μm)	60	100
Slice thickness (mm)	1	1
Slice imaging plane	Coronal	Coronal
Scanning energy (kev)	32	32
Propagation distances (m)	3.7, 9.6	6
MGD (mGy)	1, 2, 5	2, 4
Absorption-based images	32 keV, 0.2 m	32 keV, 0.2 m
properties	5 mGy	4 mGy
TIE-HOM phase retrieval	$\gamma = 870$ (full)	$\gamma = 435$ (half)

Table 4.2: Scanning protocol settings of the two synchrotron facilities for the visual grading assessment

as rings or distortions. The table shown in fig. 4.16 shows the results of the VGC analysis. The cumulative distributions of the rating data for the test images were plotted against the reference images for each image criterion, resulting in a curve whose area under the curve (AUC) could be used to compare the quality of the two sets of images. An AUC of 0.5 shows an equivalence between the two image sets, a value of 0 to 0.5 suggests that the test images were of lower quality than the reference images, and 0.5 to 1 indicates a higher quality. The intraclass correlation coefficient (ICC) test was also used to measure the inter-observer agreement, showing a moderate/good inter-observer agreement for the image set analysed (ICC = 0.626, $p \leq 0.001$).

The image quality improvement in PB-bCT images obtained by the PIXIRAD-8 CdTe single-photon-counting detector were consistently higher (AUC > 0.95) than the one for flat-panel Hamamatsu detector (AUC = 0.80) at standard radiation doses (5 mGy). Moreover, a higher image quality was obtained using the CdTe photon-counting detector at a low radiation doses, when the highest propagation distance at SYRMEP beamline that was employed. On the other hand, the standard dose PB-bCT images produced by the flat panel sensor had significantly higher image quality than the standard dose AB-CT images. This is consistent with previous research (Baran et al.; Brombal et al., 2019; Pacilè et al., 2019) which has shown that PB-bCT performs better than clinical cone-beam breast CT. However, at any of the imaging conditions, the corresponding low dose PB-CT scans from either facility were not superior to standard dose AB-CT images. It is important to acknowledge the main limitations of this study, specifically the small sample size examined and the similar, but not identical scanning settings. The different imaging conditions, such as sample-to-detector and source-to-detector distances, is unavoidable given the different layout of the two beamlines. Nevertheless, as previously

| Beamline	Imaging condition	VGC	
		AUC	p-value
SYRMEP PIXIRAD-8 CdTe single-photon-counting detector	3.7m_1mGy		
	3.7m_1mGy	0.000	0.263
	3.7m_1mGy		
	3.7m_2mGy		
	3.7m_2mGy	0.440	0.748
	3.7m_2mGy		
	3.7m_5mGy		
	3.7m_5mGy	**0.970**	<0.001
	3.7m_5mGy		
	9m_1.5mGy		
	9m_1.5mGy	0.257	<0.001
	9m_1.5mGy		
	9m_3mGy		
	9m_3mGy	**0.955**	<0.001
	9m_3mGy		
	9m_7mGy		
	9m_7mGy	**0.985**	<0.001
	9m_7mGy		
IMBL C10900D Flat Panel Detector	6m_2mGy		
	6m_2mGy		
	6m_2mGy	0.403	0.227
	6m_2mGy		
	6m_2mGy		
	6m_2mGy		
	6m_4mGy		
	6m_4mGy		
	6m_4mGy	**0.803**	<0.001
	6m_4mGy		
	6m_4mGy		
	6m_4mGy		

Figure 4.16: Results of the visual grading analysis of the image quality between PB-bCT and reference AB-CT images in both synchrotron facilities. Table taken from Giannotti et al. (2022).

stated, acquisition in each beamline was carried out under the best experimental conditions available. The complete radiological assessment, with the results of both participating centers, is under peer-review process and a related pre-print is available in MedArxiv (Giannotti et al., 2022).

4.6   Reflections on the promising results of PB-bCT

The experimental research conducted for the doctoral studies, and presented in this chapter, has addressed topics that are supportive of the potential contribution of propagation-based phase-contrast breast computed tomography for breast imaging at clinically acceptable radiation dose levels. The findings of the studies described in this chapter demonstrate that high quality diagnostic PB-bCT images for a potential use in a clinical setting can be generated at a SR facility while reducing the measured MGD when using a CdTe photon-counting detector. Hereafter, some images of the technique's promising outcomes are presented. First, to illustrate the effect of the delivered doses in the visual image quality of PB-bCT images scanned at SYRMEP beamline versus absorption-based images, a mastectomy sample acquired with 32 keV at the clinical propagation distance (3.7 m) is shown in figure 4.17. As a reminder, the standard range of radiation doses delivered with current cone beam breast CT is 4 - 12.8 mGy (O'Connell

et al., 2010). Low dose PB-CT scans (a) does not show to superior to standard dose AB-CT. However, at 2 mGy (b), PB-bCT can produce images close to the quality of AB-CT images. Image c) demonstrates that PB-bCT, outperforms AB-CT images at same dose level.
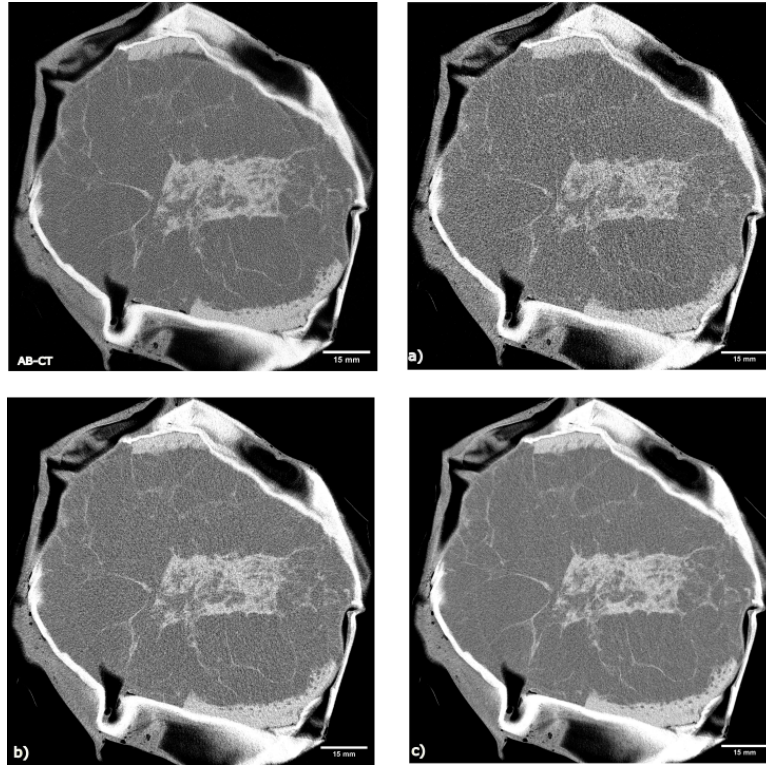

Figure 4.17: Comparison between PB-bCT images of a mastectomy sample acquired at 32 keV with a CdTe photon-counting detector at 3.7 m propagation distance with different MGD (a) 1 mGy, b) 2mGy, and c) 5 mGy), and an absorption-based image (top left) at 0.2 m propagation distance and 5 mGy.

The second example of the achievable quality of tomographic reconstructions of three mastectomy samples with the proposed PB-bCT technique under clinical bCT conditions (propagation distance = 3.7 m, MGD = 5 mGy) and different energies at SYRMEP beamline is seen figure 4.18. The displayed images underwent the pre-processing procedure (Brombal et al., 2018a) and the application of the PhR (Gureyev et al., 2017) algorithm, but without any post-proccessing corrections for ring artifacts. Visible rings artifacts are numbered 1-4, with some artifacts being more prominent than others, suggesting the presence of time-dependent detector defects, for which a post-processing ring artifact correction could be beneficial. However, an expert in breast radiological imaging techniques might find these artifacts to have a low impact in comparison to the substantially higher spatial resolution and soft tissue visibility that PB-bCT images offer. Although PB-bCT images using PIXIRAD can achieve a excellent

image quality more research with larger datasets is required. Therefore, a quantitative investigation using various mastectomy samples for the optimization of different imaging parameters, such as nr. projections and doses, energies, and propagation distances is forthcoming.

The presence of a medical physicist carrying out experiments in a synchrotron-based PB-bCT facility, as presented in this chapter, is beneficial in order to meet the high criteria for image quality as well as for safety requirements. The transformation of Elettra synchrotron facility to Elettra 2.0 and the spread of the pandemic have temporarily placed a halt to SYRMA-3D activities, which are however, planned to resume with additional experiments and optimization to clinically implement PB-bCT in the improved SYRMEP beamline.
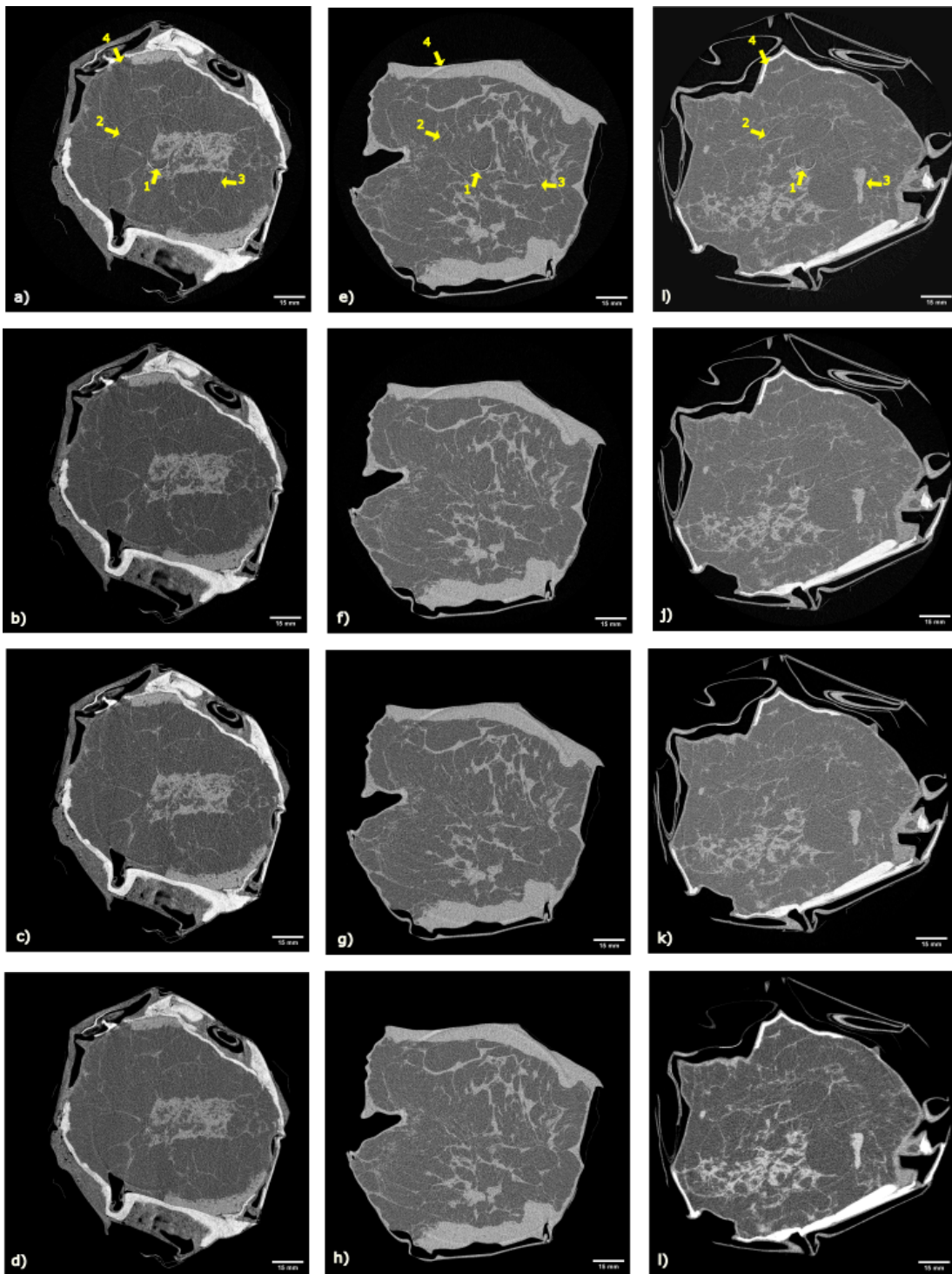
Figure 4.18: Tomographic reconstructions acquired at 3.7 m and 5 mGy of (a-d) sample 1, (e-h) sample 2, and (i-l) sample 3. Images (a, e, i) were acquired at 25 keV, (b, f, j) at 28 keV, (c, g, k) at 32 keV, and (d, h, l) at 35 keV. The samples show ring-artifacts (numbered 1-4) as post-proccessing corrections were not applied. Scale bar = 15 mm.

Chapter 5

PB micro-CT imaging for breast samples

In the previous chapters it has been described how breast tissue imaging should provide high contrast and sensitivity in order to reliably detect small structures and patterns of comparable composition. The most accurate method to identify breast cancer is through histological slicing either from an intrusive biopsy or from a surgical breast sample, while X-ray breast imaging examinations serve a non-invasive role in the identification and therapy of cancer. The reference standard procedures in the pathology of breast disease, as well as in other benign or malignant tumours, play a crucial role in cancer diagnosis and therapy planning (Zaha, 2014), that include histologic and immunohistochemical studies. Histology microscopy's great spatial resolution (better than 1 μm) enables tissue imaging down to an individual cell level. Histological slicing, however, is fundamentally a bi-dimensional approach that involves various procedures, making it a challenging, time-consuming, and costly task with a lack of capability of rendering direct 3D information of the sample (Zanette et al., 2015). In this context, the availability of a fully three-dimensional and nondestructive technique such as X-ray phase-contrast micro computed tomography (micro-CT or μCT) can be regarded as an interesting option to generate three-dimensional images of samples at a micrometer scale, that would not be otherwise resolved by conventional absorption CT. This visualization technique is referred to as virtual histology, and with the use of micro-CT, it could represent a valuable asset for pathological evaluation. Virtual histology using SR PB PhC micro-CT (PB-μCT) has been introduced as a very promising additional tool, providing full three-dimensional visualization of unstained surgical specimens at a micrometric resolution (Saccomano et al., 2018; Mittone et al., 2020; Frohn et al., 2020). This chapter presents a 3D approach for virtual histology of breast tissues, based on phase-contrast micro-CT, and the advantages and disadvantages of the methodology are discussed. The activities I carried out in this part of the thesis include my participation in the optimization

of imaging parameters specifically for micro-CT imaging at SYRMEP beamline at the Elettra synchrotron, and morphological study of three different breast samples using phase-contrast virtual histology, where I post-processed the acquired images and carried out a one-on-one analysis together with a pathologist.

5.1   Breast lesion diagnosis with conventional histology

Upon a suspicious area in the breast, such as a breast lump found in a clinical exam or other signs in radiological images, patients with possible breast cancer are referred to perform a breast biopsy. A breast biopsy is a procedure to remove a sample of breast tissue for testing, where pathologists examine the tissue sample and provide a diagnosis. The results of a breast biopsy can show whether the area in question is breast cancer or not. In confirmed cancer cases, a lumpectomy or mastectomy is performed to remove cancerous or other abnormal breast tissues, which are later studied by pathologists. An alternative approach, when accompanied with radiation therapy, is the breast conserving surgery. It is considered safe and preferential for early detected cancers, since it provides the same level of survival rates as mastectomy and much better cosmetic effect (Mansell et al., 2017). In this kind of treatment, a small amount of normal tissue surrounding the tumor, known as surgical margin, is also removed and evaluated through histology to determine the presence of cancer between the tumor itself and the outer edge of the margin. There is a great deal of debate surrounding the definition of the margin, as its delineation will determine the course of treatment while evaluating the risk of recurrences, and whether additional surgery may be recommended.

Histological slicing is the gold standard for the evaluation and characterization of biological tissues. Owing to the great variety of class-specific dyes (DNA, proteins, lipids, or carbohydrates), histology provides a high discriminative power at both tissue and cellular levels Veuthey et al. (2014). This is combined with the high spatial resolution offered by microscopy , that allows imaging at cellular level. A series of technique processes are involved for the preparation and analysis of tissue samples, as seen in figure 5.1. Routine tissue processing for histology requires fixing the samples in 10% neutral-buffered formalin. The specimens are then moved to xylene, a clarifying agent that is added for easier reading, and paraffin wax is then melted down to embed the sample and form a tissue block. The tissue blocks are then sectioned into fine sections (usually 2-6 μm thick) using stainless steel knives, which are later set up on glass slides. Most stains used in light microscopy are aqueous, so the sections have to be rehydrated before staining. A graded series of solvents is used to remove the paraffin from the tissue,

which is then rehydrated, and finally color stained to enhance the visibility of the cells.
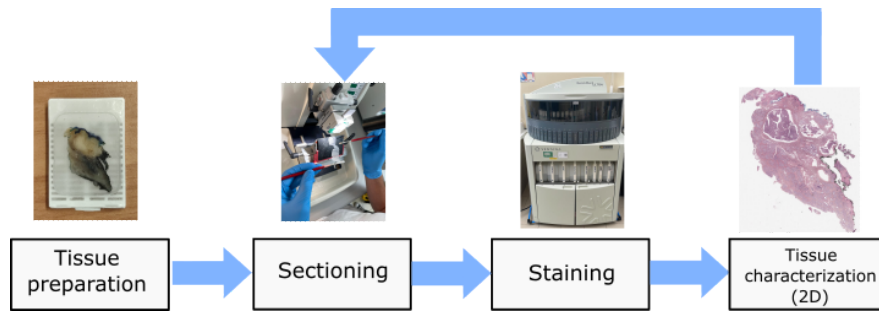
Figure 5.1: The different steps involved in conventional histology to obtain a two-dimensional image. If additional information on the sample is needed, new sections need to be cut and stained. Original artwork.

The examination of the mammary glands benefits from the use of several stains. Hematoxylin and Eosin (H&E) is the most widely used stain in histology and histopathology laboratories. The eosin component gives protein-composed structures a pinkish color, while the hematoxylin component gives the nuclei a blue/purple stain. Other stains are applied for different purposes, such as Masson's trichrome stain, to visualize collagen fibers and it is helpful to assess fibrosis. Immunostaining can also be utilized to recognize antigens that are important diagnostic markers. However, due to the several steps involved in conventional histology (slicing, staining, imaging, and analysis) the methodology is time-consuming, expensive, and labor-intensive, as each step requires the use of specialized equipment (not to mention human resources).

Histology is fundamentally a two-dimensional technique, which makes it difficult to understand the relationship of the information gathered in one section to the original three-dimensional structure, unless serial sections are performed. Even though serial sectioning can offer rather coarse in-depth information (Lakin et al., 2013), important features could be missed if the appropriate section is not taken. Additionally, cutting is a destructive procedure that can result in tissue damage or deformation from the mechanical stress, or can even lead to creating cutting artifacts (Albers et al., 2018b; Ross and Pawlina, 2011).

Therefore, it would be appealing to have a method that it would be fully three-dimensional, non-destructive and that offers good soft tissue sensitivity. PB-μCT has been introduced as an extremely promising alternative for virtual histology, as it is fully three-dimensional, thanks to the properties of phase-contrast technique that were presented in chapters 1.5 and 3, it offers a complete three-dimensional visualization at micrometric resolution of surgical specimens, which can be virtually sliced at any point and in any direction without requiring any

staining and without destroying the block sample. The potential benefits of using this method are detailed in the next section.

5.2 Phase-Contrast Virtual Histology

The use of Computed Tomography at the micrometre scale (μCT) is becoming a viable solution in the field of virtual histology (Albers et al., 2018a,c; Baran et al., 2018b). One of the challenges of virtual histology is related to the poor X-ray attenuation contrast that exists between the soft tissues commonly encountered in sample specimens. Conventional μCT typically yields insufficient tissue differentiation, contrast-enhanced μCT has been proposed (de Bournonville et al., 2019) to overcome this limitation, where histological samples are perfused with tissue-specific radio-opaque contrast agents, therefore yielding a high image contrast. Phase-contrast micro-CT has been introduced as an extremely promising alternative, as it can be performed without tissue staining (Saccomano et al., 2018), therefore being in principle simpler and compatible with standard histology procedures. Moreover, PB-μCT opens up the possibility of studying specimens that require imaging down to a micrometer resolution, that can be virtually sliced at any point and in any direction without needing staining and without destroying the sample. In this context, investigations at SYRMEP (Albers et al., 2018b; Baran et al., 2018b) carried out in the experimental station have shown that PB-μCT provides a tissue visibility, both in terms of contrast and spatial resolution, that is compatible with the requirements of virtual histology.

To be suitable for clinical evaluation, virtual histology images should have a spatial resolution high enough to distinguish small structures but, at the same time, cover a sufficiently large volume to enable the inspection of the specimens, usually having sizes of 4-5 cm^3. The spatial resolution required by virtual histology is considerably higher than that used for diagnostic imaging, as pixel values of the order of 1-5μm must be achieved. Such high spatial resolutions must be combined with high signal-to-noise ratio (SNR) to provide adequate visibility of soft-tissue structures in the virtual slices. The high soft tissue contrast offered by X-ray phase-contrast imaging techniques can be compatible with virtual histology requirements (Donato et al., 2022a; Albers et al., 2018b; Töpperwien et al., 2018; Baran et al., 2018a; Katsamenis et al., 2019; Longo et al., 2020; Massimi et al., 2022; Twengström et al., 2022). The extremely high X-ray fluxes which are needed to provide high SNR at high resolution, is commonly achieved at synchrotron facilities by employing polychromatic beams. These features require the use of small-pixel indirect-conversion detectors, such as CCD or sCMOS, usually coupled

with magnifying optical elements, leading to a detector's response function that is far from being a 1-pixel wide function. In this context, an experimental optimization the geometrical parameters of free propagation distance and pixel size to provide adequate resolution images for x-ray based virtual histology of breast surgery specimens was performed at the SYRMEP beamline by means of PhC μCT and employing a commercial sCMOS detector. Many of the contents presented in the following sections of this thesis have been published in Donato et al. (2022a), work in which I was a co-author.

5.3 Optimization of acquisition parameters for virtual histology

The works by Brombal et al. (2018b); Brombal (2020b) quantitatively demonstrated that a careful optimization in terms of pixel size and propagation distance is required to fully exploit the advantages of PB and PhR. Within this frame of reference, an investigation was carried out to optimize acquisition parameters, namely the propagation distance and the pixel size, in PhC μCT for virtual histology of breast surgery specimens. Differently form other experiments presented in PB-bCT, where a single photon counting detector was used, a commercial sCMOS detector imaging system was employed in order to achieve the requirements of higher spatial resolution of virtual histology.

5.3.1 Image noise model in PB-μCT

Nesterets and Gureyev (2014) and Nesterets et al. (2018) described mathematically the effect of PhR on μCT images proposing a model in which all the the components of the tomographic imaging chain are included. More specifically, the model assumes a Poisson dominated detector noise, flat-fielded 2D projection images, stable source intensity and imaging setup, and a parallel beam geometry with reconstruction performed through the Filtered-Back-Projection (FBP) algorithm Nesterets et al. (2018). When measured in a homogeneous region portion of the μCT image acquired at a fixed fluence, the SNR can be expressed as:

$$SNR \propto \frac{h^2}{M^2} \frac{1}{f(A;d/h)} \tag{5.1}$$

where, M is the geometric magnification, h the detector pixel size, $f(A;d/h)$ a dimensionless function that accounts for the tomographic process (filtering and interpolation), the detector's Modulation Transfer function (MTF) and the phase retrieval Brombal (2020b). Additionally, d is the full-width-at-half-maximum (FWHM) of the detector's point spread function and the parameter A depends on the refractive properties of the sample, on the setup geometry and on

the detector pixel size as:

$$A = \pi \frac{\delta_1 - \delta_2}{\beta_1 - \beta_2} \lambda M \frac{R_2}{h^2} \tag{5.2}$$

where λ is the radiation wavelength, the subscripts 1, 2 in the δ and β terms refer to an interface between two materials having given different refractive indices, and R_2 is the sample-to-detector (or propagation) distance. The validity of the model applies in the near-field propagation regime, corresponding to large Fresnel numbers, i.e., $N_F = d^2/(M^2 \lambda R_2) >> 1$ (even if often this condition is relaxed down to N_F slightly higher than 1)

5.3.2   Experimental configuration and data processing

A surgical breast specimen with an intraductal papilloma, a benign breast lesion that develops within the mammary duct. The sample was acquired following the framework of the operative protocol of the Breast Unit of the Trieste University Hospital ("PDTA Neoplasia mammaria", approved on 11 December 2019 by ASUGI-Azienda Sanitaria Universitaria Giuliano Isontina, Italy) and the standard operative procedures of the clinical unit of the Anatomy and Histology Department of the University Hospital of Cattinara. The protocol entails a written informed consent which is obtained from the patients before their inclusion into breast CT imaging studies. The specialist breast center of ASUGI is in compliance with the standard of EUSOMA guidelines (certificate No. 1027/01). The Directive 2004/23/EC of the European Parliament and of the Council of 31 March 2004 was followed on setting quality and safety standards for the donation, procurement, testing, processing, preservation, storage, and distribution of human tissues.

Tomographic acquisitions for the virtual histology studies of the surgical breast specimen were acquired at the SYRMEP beamline, which can be operated in monochromatic or polychromatic (white/pink) mode using the entire energy spectrum. When operating in white/pink beam modality, as in this study, the SR beam produced by the bending magnet is filtered by using different materials, such as silicon (Si), aluminum (Al) or molybdenum (Mo) to optimize the X-ray spectrum for the desired experiment (Dullin et al., 2021). For this investigation a filtration with 1 mm of Si was used to exclude low energy components and lessen the beam-hardening effect, resulting in a beam in the energy range from 8.5 - 40 keV, with average energy of 24 keV. A Hamamatsu sCMOS camera (2048×2048 pixels) coupled with a GGG:Eu scintillator (thickness of 45 μm) and a high numerical aperture optic was employed as imaging system, which enables to adjust the pixel size between 0.9 and 6.5 μm. The scans were acquired using three different pixel sizes (h), namely 1, 2.5 and 4 μm at five different sample-to-detector

distances (R_2): 4.5, 150, 250, 500 and 1000 mm, while the source-to-sample distance was constant at 22.3 m. 1800 projections over 180° were collected at 40 msec/projection, resulting in an overall exposure of 72 s per scan.

Projections were pre-processed by conventional flat-fielding and ring artifact removal. Subsequently, the TIE-Hom-based phase-retrieval filter (Paganin et al., 2002) was applied with a two-material interface $\delta/\beta = 350$ filter parameter. Phase-retrieved projections were reconstructed by using a GPU-based FBP algorithm (Brun et al., 2017) and Shepp-Logan filtering. Low-energy X-rays in polychromatic X-ray tomography are attenuated more efficiently than high-energy X-rays when passing through matter. Further inside the material, the transmitted beam spectrum gets proportionately richer in high-energy photons, increasing its penetration or becoming "harder" on the material. Beam hardening (BH) is a phenomenon that implies that the projection data's grey levels are non-linear with respect to the form of a cross-sectional linear profile (Khan et al., 2015). As a result, there are some visual aberrations in the reconstructed image, such as pronounced edges ("cupping effect"). The attenuation coefficient of the cupping artifact appears to be stronger at the outer portions than the inner. Such artifacts only affect polychromatic (X-rays) CT and not monochromatic CT. Therefore, reconstructed μCT images from the polychromatic source were processed via a de-trending procedure developed by (Khan et al., 2015) for an additional beam-hardening correction .

For each dataset, SNR was measured within an homogeneous region filled by paraffin. A square region of interest (ROI) was selected in 10 consecutive slices and the SNR was evaluated as the average gray level over the standard deviation within the same ROI. The measured value was then divided by the SNR computed in the image acquired at the shortest propagation distance (45 mm) without the application of the phase-retrieval , as in conventional μCT, resulting in an SNR_{gain}. The final $SNR_{(gain)}$ values and associated uncertainties were originally computed taking the average and standard error over the 10 measurements.

5.3.3 Results

For each image, noise and SNR were measured within an homogeneous regions of the paraffin embedded sample Experimental results as shown in the plots in Fig. 5.2, were compared to the theoretical model, which was adapted to the imaging system-specific point-spread function.

The SNR is displayed as a function of propagation distance h for 1.0, 2.5, and 4.0 μm pixel sizes in panels (a), (b), and (c), respectively. A normalizing factor has been used to scale the theoretical curves so that points at 45 mm of propagation distance are in agreement with
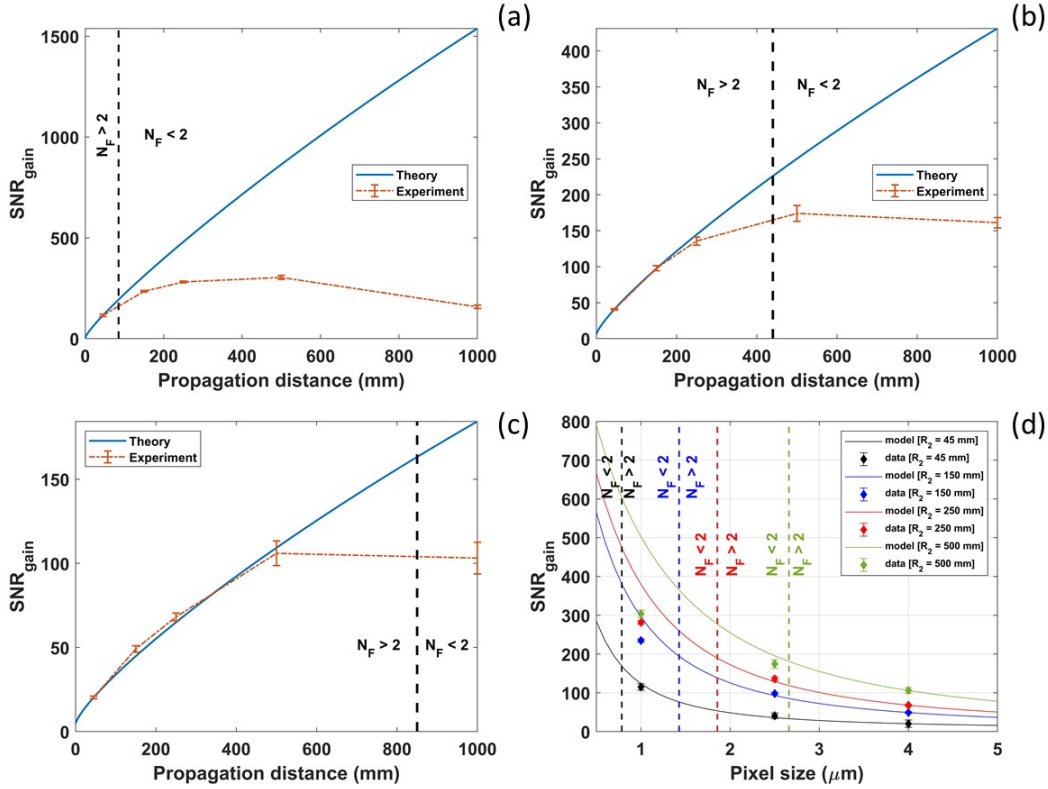
Figure 5.2: Panels from (a) to (c) show SNR as a function of the propagation distance (uncertainties are showed with error bars) for h = 1.0, 2.5 and 4.0 μm, respectively. Blue solid lines are the theoretical predictions while red dot-dashed lines the experimental measurements at propagation distance of 45 mm, 150 mm, 250 mm, 500 mm and 1000 mm. Panel (d) shows the measured SNR as a function of the pixel size for 45 mm (black), 150 mm (blue), 250 mm (red) and 500 mm (green) propagation distance. A threshold N_F=2 is used for illustration purposes. The departure from the model is observed for $N_F < 2$. Plots taken from Donato et al. (2022a).

the experimental readings. When the near field requirement is met (a threshold of N_F=2 is used for illustration purposes), and taking the errors into account, the experimental results agree with the model's prediction of an increase in SNR. For all propagation distances in panel (d) (in different colors), the measured SNR is plotted against the pixel size . Disparities between experiment and theory were identified when the near-field condition is no longer satisfied (at $N_F < 2$).

Images acquired with $h = 4$ μm at five sample-detector distances are displayed in Fig. 5.3, where a detail of the image without using PhR, at the shortest propagation distance is shown in (a), and the reconstruction using PhR is shown from (b) to (f). The function f does not explicitly depend on both pixel size h and magnification M when no PhR is used ($A = 0$), as shown in panel (a), therefore SNR is proportional to $h2/M2$ as is known for conventional μCT. When PhR is applied ($A > 0$), as shown in (b) to (f), the function f will produce smaller results

than in the case of $A = 0$, increasing SNR as a result.

Experimental results are in good agreement with the theoretical values for the SNR as predicted by the model for large Fresnel numbers ($N_F > 2$). The model describes well the experimental data for all the geometrical configurations, allowing to select the most appropriate propagation distance to generate images with the highest SNR, once the pixel size is selected. Therefore, this careful optimization in terms of pixel size and propagation distance using polychromatic synchrotron radiation and a commercial imaging system was validated. This optimization served as guideline in the choice of the best experimental parameters for the subsequent study aimed to evaluate the potential of 3D PhC virtual histology for features of breast tissues, by comparing them using conventional histology and PhC virtual histology, study that will be discussed in the next section.
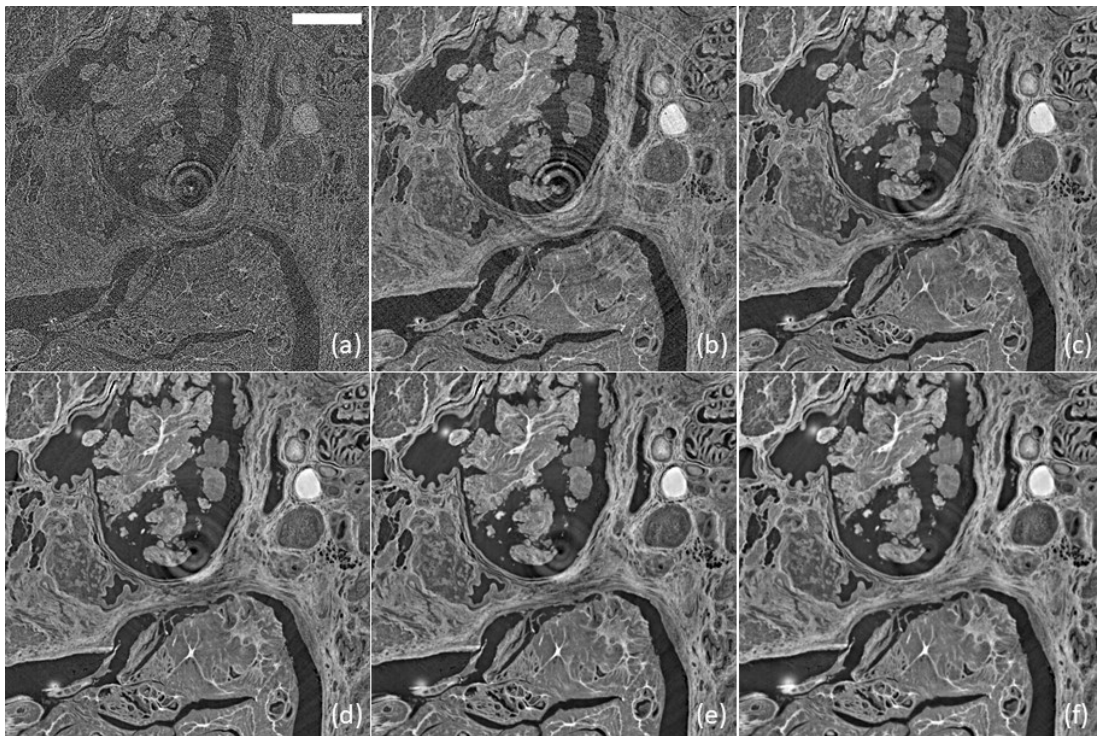
Figure 5.3: Detail of a slice of the breast specimen acquired with pixel size of 4 μm. Panel (a) shows the detail at 45 mm of propagation distance without the application of phase-retrieval. From (b) to (f) the same detail at propagation distance of 45 mm, 150 mm, 250 mm, 500 mm and 1000 mm, respectively, with the application of PhR. At larger propagation distances, up to 500 mm, a major increase in SNR can be observed. Scalebar in (a) is equal to 1 mm. Figure extracted from Donato et al. (2022a).

5.4   3D Phase-Contrast Virtual Histology of Breast Tissues

As mentioned previously, the distinction of breast tissue alterations is essential to identify both benign and malignant alterations. The gold standard to assess and characterize tissue alterations is through histological slicing, but the technique may be limited by their bidimensional approach along with other conditions stated in sec. 5.1. This limitation has served as motivation to continue developing 3D virtual histology studies using PB-μCT technique as means for improving tissue visualization and a volumetric perspective of surgical breast tissue sample to complement their histological characterization. The methodology and results of this study carried out in the last part of my doctorate studies are detailed in the following paragraphs, where I post-processed the acquired images and carried out a one-on-one analysis together with a pathologist.

5.4.1   Surgical breast specimens

Three breast tissue samples were acquired from one mastectomy and two lumpectomy samples, following in the framework of the operative protocol mentioned in 5.3. The samples were representative of one benign breast lesion, an intraductal papilloma, and two malignant lesions, an invasive micropapillary cystic carcinoma and an invasive lobular carcinoma. An intraductal papilloma is a benign proliferative lesion of the breast that grows in a milk duct of the breast. Histologically speaking, is a complex arborizing (tree-like) fibrovascular cores surrounded by myoepithelial cells and covered by luminal cells are present within a dilated ductal space. On the other hand, the two remaining lesions are categorized as invasive, meaning that the cancer has spread beyond the layer of tissue in which it developed and is growing into surrounding, healthy tissues. The invasive micropapillary intracystic carcinoma (IMPIC) is a distinct variant of mammary carcinoma, in which tumor cells are grouped in bubble-like clusters of cells lacking of fibrovascular cores, and situated within empty stromal spaces. It is an infrequent type of breast cancer often discussed for its potency for lymphovascular invasion and difficulty in accurate imaging estimation (Yang et al., 2016). The other scanned malignant lesion, the invasive lobular carcinoma of the breast (ILC), is the second most frequent invasive breast carcinomas, accounting for 10%–15% of all invasive breast carcinomas (Luveta et al., 2020). ILC begins in the lobules of the breast and infiltrates adjacent healthy breast tissues in a single-file pattern, with little disturbance of normal tissue architecture and without frequently forming a palpable lesion, thus making it hard to detect on a physical exam. Moreover, radiological diagnosis of ILC can be particularly challenging as current imaging modalities lack specificity

for differentiating ILC from other invasive breast cancers (Helvie et al., 1993; Grubstein et al., 2016; Tagliati et al., 2021) , which is related to its characteristic pattern of growth . According to Lopez and Bassett (2009), higher false-negative rates in mammography (up to 19%) are reported for ILC than for other invasive cancers.

In regards of the stains used to analyze the aforementioned samples, Hematoxylin and eosin (H&E), Masson's trichrome stain and pancytokeratin, an immunochemistry stain, were used for the routine tissue processing is histology at the Breast Unit of the Trieste University Hospital, as explained in sec. 5.1. All histological images were digitized using a D-Sight F 2.0 slide scanner with the same acquisition conditions with magnification of 20× and pixel size of $0.42\mu m \times 0.42\mu m$. Afterwards, some regions of major histological interest (ROI) were chosen to be scanned using PB-μCT (see Figure 5.5).

5.4.2 Experimental micro-CT setup and image reconstruction

X-ray phase-contrast tomographic acquisitions of the previously chosen ROI for each paraffin-embedded sample were carried out the Elettra SYRMEP beamline using the experimental set-up explained in sec. 5.3.2 as well as the image processing and reconstruction method. The magnifying optics of the imaging system allowed the effective pixel size to be adjusted to 1, 2.5, and 4 μm. Based on the results of the optimization study for virtual histology (sec. 5.3) the selected propagation distances were 150 mm for 1 μm pixel size, 250 mm for 2.5 μm pixel size and 500 mm for 4 μm pixel size, with a resulting field-of-view (FOV) 1.86 mm, 4.65 mm, and 7.44 mm in diameter respectively (see Figure 5.4). Considering the sensor size, acquisitions at 2.5 and 4 μm enabled to acquire the full height of the sample, while only 1.86 mm from the upper surface of the specimens were acquired at pixel size of 1 μm. It is important to remark that there was no additional sample preparation for the micro-CT scans, and, with the selected acquisition parameters, no noticeable radiation damage was observed.

I performed the de-trending procedure (Khan et al., 2015) in the μCT reconstructions to mitigate cupping effects due to BH, in addition to applying the ring-removal methodology as presented in sec. 3.3.3. The final tomographic reconstructions could be viewed as an interactive image stack, allowing a 3D visualization of the whole scan.

### 5.4.3 Virtual slicing and 3D assessment

Tomographic reconstruction slices on a local CT dataset corresponding to the surface of the paraffin-embedded sample block were reviewed and compared to the preliminary H&E histological sections to ensure that the μCT scanning area corresponded to the ROI chosen by

the pathologist. An interactive virtual depiction of the 3D sample volume was made possible via CT reconstructions. The experienced pathologist examined the entire sample through virtual slicing and evaluated important characteristics in the specimen's three orthogonal planes. The pathologist's knowledge of the sample's features and their visualization was improved by the 3D analysis of the sample volume, and this enabled the pathologist to be guided or the consecutive sectioning of the sample.

5.4.4   Subsequent histological procedures and final match

Each paraffin-embedded sample block was subsequently sectioned at various depths in accordance with the traits seen in the previous 3D volume evaluation to further characterize the sample's histology. Sections were routinely deparaffinized and stained with H&E using the Masson's trichrome staining method (Sun et al., 2018), which highlighted the collagen deposition around the tissue. Pancytokeratin, an essential immunohistochemical marker (Bonacho et al., 2020), was also employed to identify isolated tumor cells.

The pathologist manually traced important elements in the H&E histological images that best matched in the corresponding virtual μCT stack. I analyzed the resulting paired CT slices
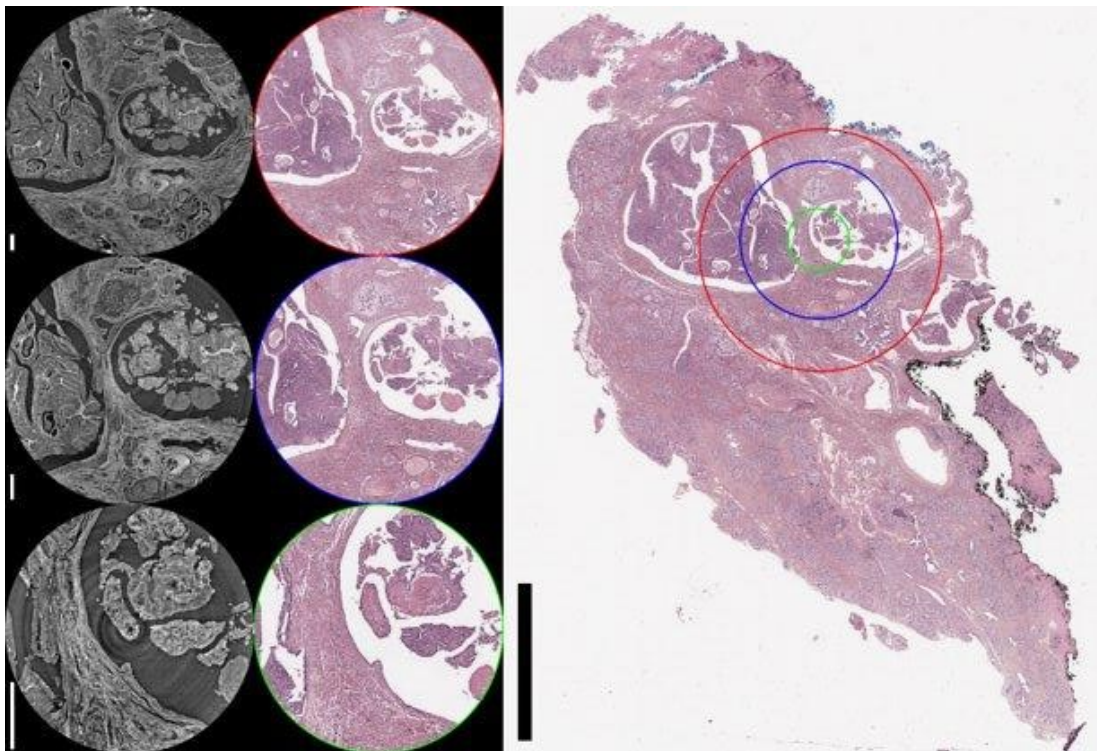
Figure 5.4: Comparison of the image resolution between PB-μCT images acquired at : top, 4 μm (red circle), middle, 2.5 μm (blue circle) and bottom, 1 μm (green circle) pixel size. There is a trade-off between FOV and spatial resolution. Original image.

were thoroughly analyzed together with the pathologist through comparing, contrasting, and correlating the observable morphological structures across the methodologies, as well as pin-pointing visualization advantages and disadvantages of PB-μCT images in comparison to the different staining protocols. A visual representation of the methodology followed in this study is shown in fig. 5.6.

5.4.5   From conventional to virtual histology: a morphological comparison

Virtual slicing was used to show the entire sample PhC 3D data during a one-on-one analysis with the pathologist. More information was obtained without the need to further manipulate the sample, as is the case with conventional histology, considering that micro-CT images could be manipulated in any direction and the cross sections of the internal areas of the samples could be viewed from any angle. The pathologist's comprehension of the sample's features and their visualization was improved by this 3D analysis of the sample volume. It also helped the pathologist decide on a better cutting section and define additional staining to highlight particular features that were seen in PhC virtual histology. The specific findings for each breast specimen are discussed in the following paragraphs.

#### 5.4.5.1   Normal breast tissue

One of the aims of this study was to evaluate the ability of micro-CT to differentiate various components of breast tissue in formalin-fixed, paraffin-embedded samples. Differentiating the
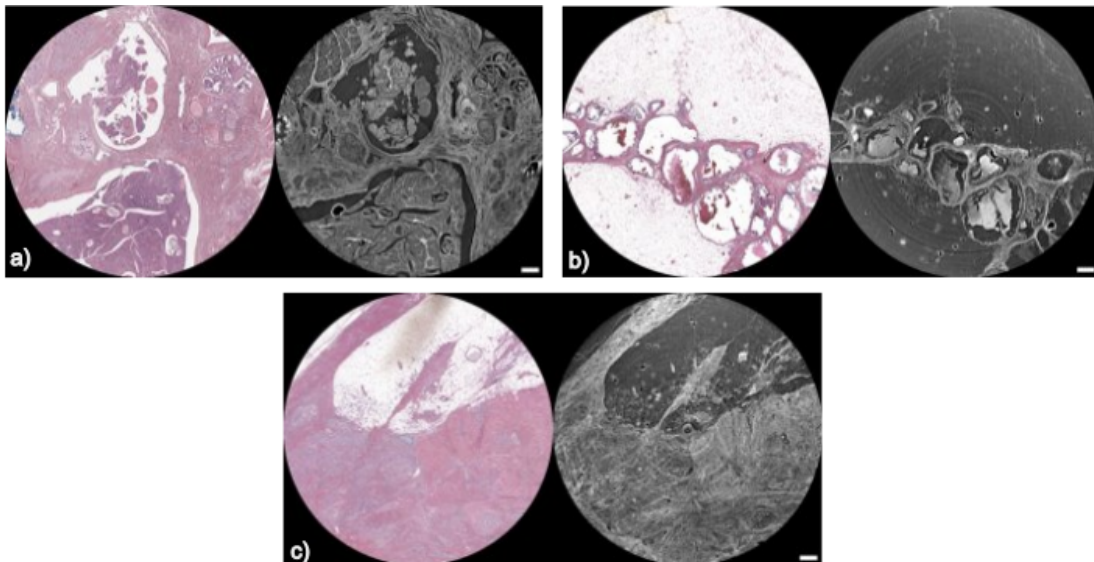
Figure 5.5: Regions of histological features of interest for all breast samples studied. On the left, the histological slides of the breast specimens. On the right, the area that was scanned with PhC mCT. a) Normal breast tissue and intraductal papilloma, b) micropapillary intracystic carcinoma, c) invasive lobular carcinoma. Scalebars equal to 0.5 mm. Original image.

individual parts of normal tissue is very useful in order to subsequently identify both benign and malignant alterations. Particularly, it is useful to identify the basement membrane and the interface zone between the epithelium and the stroma, to distinguish and invasive from an in situ carcinoma. The reader is invited to review section 1.2 and fig. 1.1 to recall the structures of the complex network of lobes and ducts that forms the breast, for better understanding of this section.

It is important to remark that the histological structure of the ductal tree is identical regardless of the size of the duct. A uninvolved site taken from a patient diagnosed with intraductal papilloma was used to analyze the architecture of the normal breast. Figure 5.7 shows a representative section of normal tissue in histology slides using: (a) 2D hematoxylin and eosin (H&E),(c) Masson's trichrome, and (d) pancytokeratin staining methods, along with the corresponding the reconstructed 3D PB-μCT dataset (b) scanned at 4 μm. By comparing the H&E image (gold standard histology) and its corresponding PB-μCT image (virtual histology)
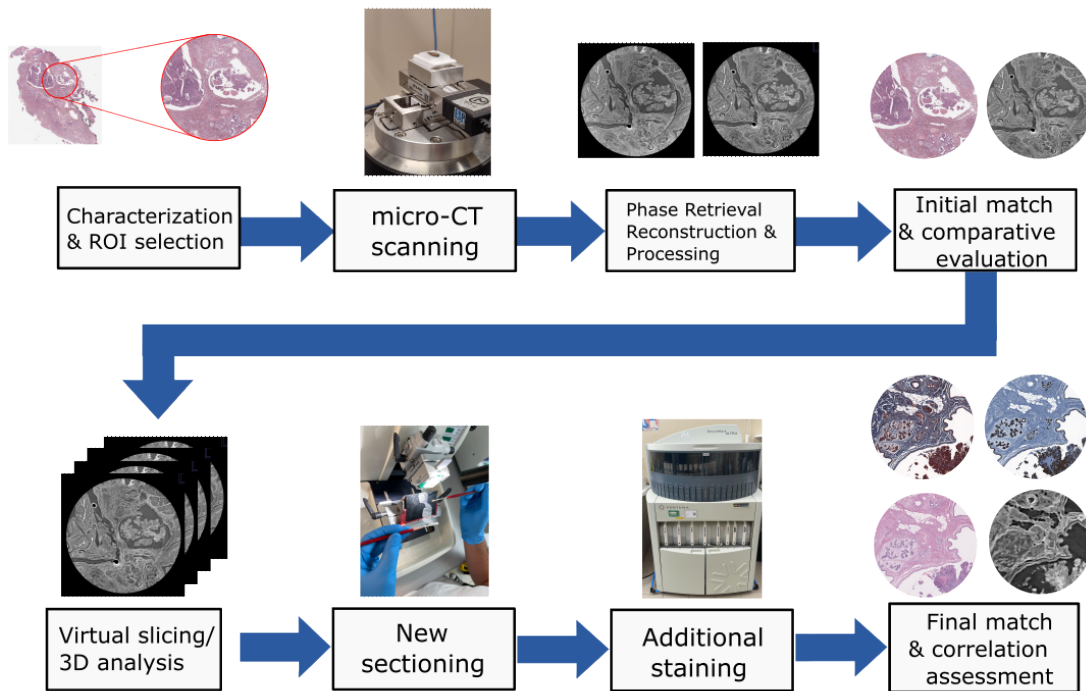
Figure 5.6: Step-by-step visual description of the procedure used in this investigation. Following sample characterisation, phase-contrast x-ray μCT was used to scan the selected ROIs. The subsequent phase retrieval, reconstruction, and analysis of the generated projections followed. A preliminary match and comparison were done. Further sections were created for additional histological assessment. The resulting histology images and the associated PhC-CT images were matched. Finally, a compare-and-contrast assessment of the resulting matched images was performed. Original artwork.

fig. 5.7, two mammary lobules (sack-like structures) can be identified in each image. Smaller structures are also visible such as, the acini (A) open into the terminal duct lobular unit, TDLU, (marked as D) embedded in the intralobular stroma (I), which is subsequently surrounded by a more compact interlobular stroma (E) with abundant adipose tissue. This adipose tissue, is recognized very well in both conventional and micro-CT histology images, as the single adipocytes (Ad) cells.
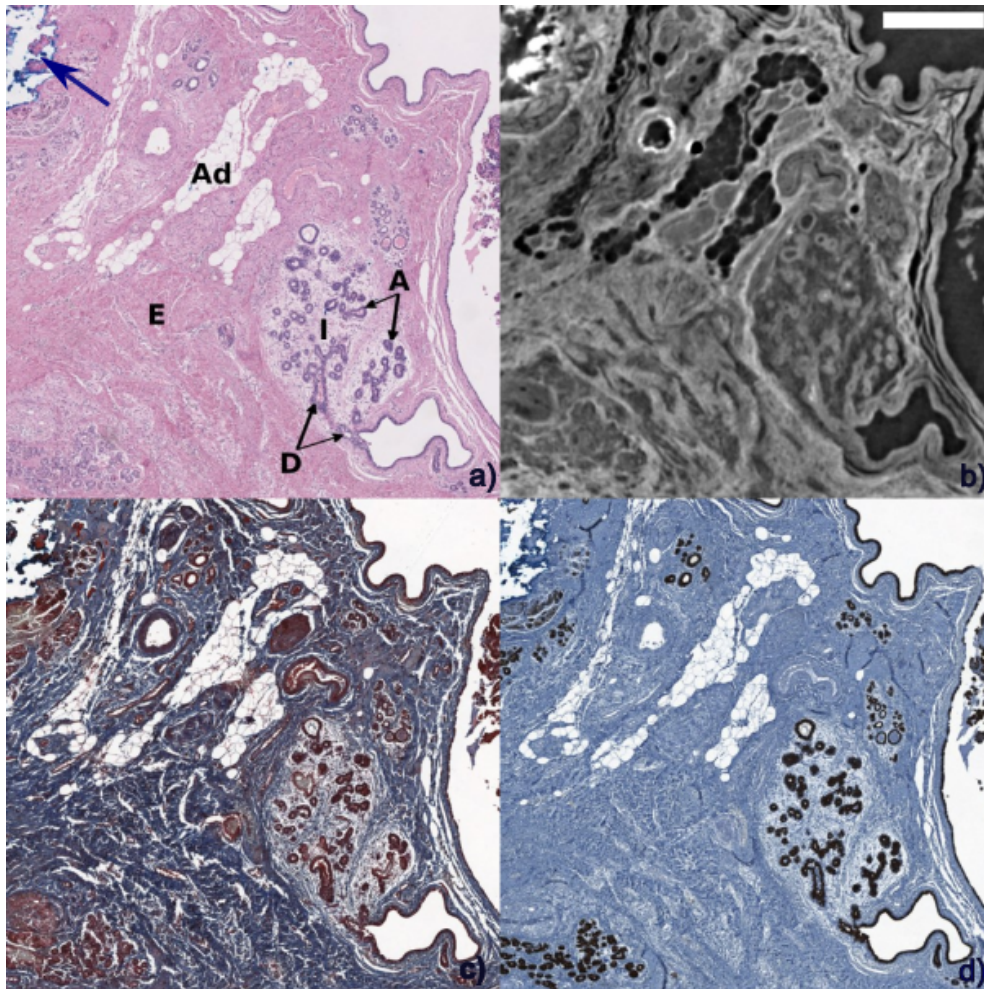
Figure 5.7: A comprehensive visual correlation of the mammary lobules and fibroadipose tissue between : the histological staining techniques (a, c-d) obtained with a D-Sight F 2.0 slide scanner for digital pathology and PB-μCT (b) at 4 μm. The histological techniques presented are: (a) haematoxylin and eosin, (c) Masson's trichromic, (d) pancytokeratin. In the images important visible structures within the two lobes (sack-like structures) are: approximately twenty small glandular structures called acini (A) in each lobe that open into a terminal duct (D). Other visible structures are: adipocites (Ad), intralobular stroma (I), and interlobular stroma (E). In the upper left corner of each image is also visible the cauterization artifact, indicated by the arrow, that appears blueish in the histological images and white in PB-μCT images. Scalebar equal to 0.5 mm. Original image.

Artifacts in histological slides can be generated at all stages of tissue preparation and are

related to the methodology, equipment, or reagents used during preparation (Ross and Pawlina, 2011) leading to morphological variations. However, the artifact depicted by the blue arrow, in the upper left corner in figure 5.7, is caused by the cauterization method (electrocautery) applied during the surgical specimen collection. Such artifacts should not be undermined as the magnitude of the distortion and affect the whole sample, and not only the slice that was taken, as it seen in fig. 5.9, where a 3D rendering of the sample shows the complete extension of the electrocautery artifact (yellow arrow). According to the pathologist, different effects caused by the electrosurgical method can be identified in figures 5.9 and 5.7 such as: complete charring without cellular structures, severe tissue degeneration, and confluent tissue with few discernible structures, indistinguishable nuclei, and rupture tissue, distressed cellular architecture with a thin appearance, irregular elongated and tapering nuclei, smeared chromatin, visible distorted fibroblast nuclei without clear cell boundaries, and cells visible but not clear whether they are epithelial or stromal. Although PB-μCT images did not show single ductal cells as in the histological staining techniques, they did offer an enhanced visibility of the lobe and the ductal lobular unit compared to any of the three histological images, without requiring specific preparation to highlight its visibility. The different gray levels that phase-contrast images offered, improved the discernability of the TDLU as an encapsulated structure with a clear margin, rather than the color gradient that was seen in any of the histological colorations. It can be stated that using PhC virtual histology for differentiating the various components of normal tissue is similar to histology, and for particular structures, virtual histology use offers better visibility than conventional histology.
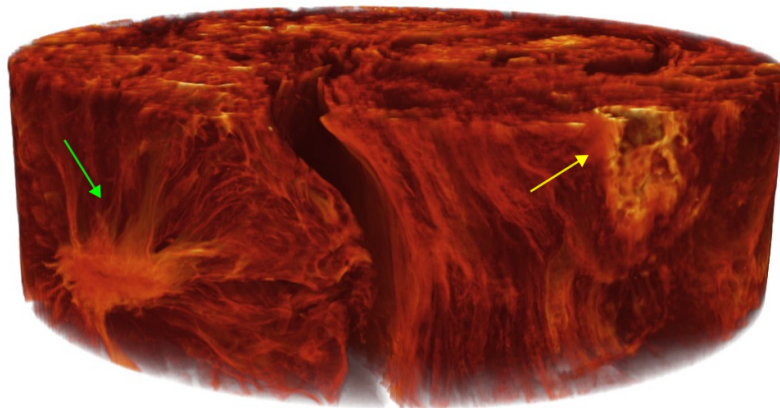
5.4.5.2   Intraductal papilloma

The side-by-side presentation of PB-μCT and histology data in figure 5.8 of the intraductal papilloma the stromal tissue, the fibrovascular core and the stromal axis (with a tree-like appearance) in PB-μCT images at 4 μm were better distinguished as with the Masson's trichromic image. They are clearly identifiable in the micro-CT images even to the untrained eye. Recognition of the stromal tissue is important for the progression of breast cancers, as it can determine tumor suppressing or tumor-promoting environments (Arendt et al., 2010). An interactive visualization of the 3D PB-μCT data sets was made with Avizo software (TermoFischer Scientific) and a volume-rendering image is displayed in figure 5.9. It not only shows the presence of the fibrovascular core (green arrow) thanks to the tissue-contrast provided by the virual histology methodoloy, but also the extension of the whole structure.
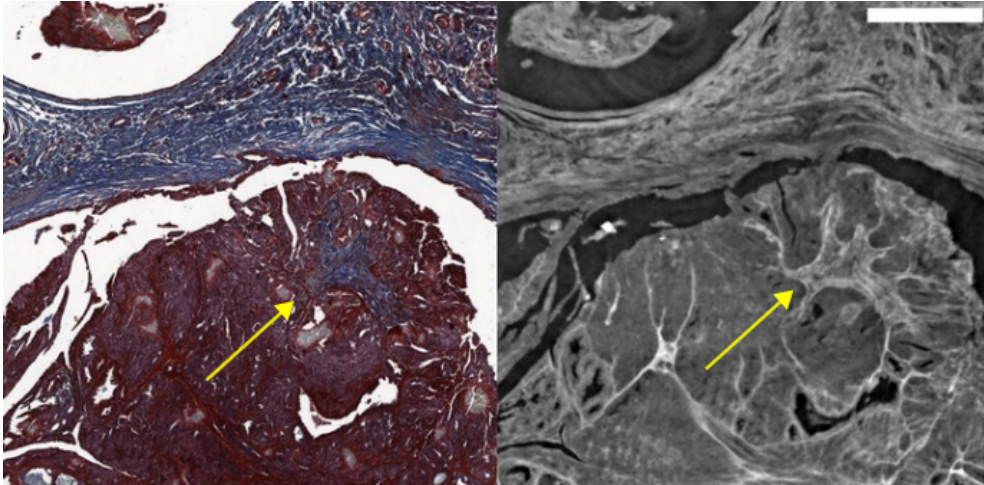
Figure 5.8: Comparison of the visibility of the fibrovascular axis and core in Masson's trichromic (let) and in PB-μCT at 4 μm. The presence or absence of the fibrovascular cores is crucial for the assessment between benign and malignant papillary lesions. Scalebar equal to 0.5 mm. Original image.

PB-μCT virtual histology improved the visibility of intraductal papilloma-related characteristics, without any extra preparation of the sample, and could therefore supplement traditional histology with more information. Virtual histology with PB-μCT enhances its visibility , as it is needed for the histological slides.

Figure 5.9: A PhC-/muCT 3D rendering visualization of the paraffin-embedded sample containing a benign intraductal papilloma. The extension of the fibrovascular core (green arrow) is appreciated thanks to the three-dimensionality of the technique. Similarily, the electrocautery artifact (yellow arrow) exhibits a tissue distortion affecting a large portion of the sample. Original image.

5.4.5.3   Invasive micropapillary cystic carcinoma

Virtual histology images of the micropapillary cystic carcinoma show the bubble-like cluster of cells, typical morphology of such lesions, with an enhancement between the stromal/epithelial interface and the basement membrane (red arrows in fig.   5.10. Even very small and thin structures, such as the fibrous septum (FS) are easily identified in PB-μCT images at a pixel size of 4 μm (fig. 5.10). Clots within the cystic spaces (blue star) are clearly evident in PB-μCT, while they may not be present in the hematoxylin-eosin images, because these structures can be lost during the specimen cutting procedure or during glass slice preparation.
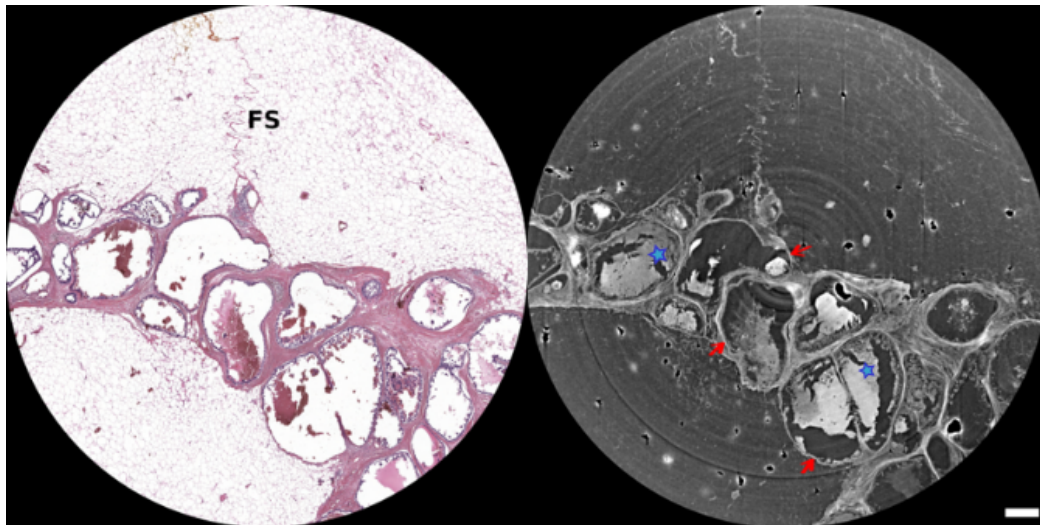
Figure 5.10: Comparison of the fibrous septum (FS), clots within the cystic spaces (blue stars) and basement membrane (red arrows) between PB-μCT images (right panel) acquired at 4 μm pixel size and its corresponding histological image (left panel). Scalebar equal to 0.5 mm. Original image.

A hybrid visualization of the histological cross-section and 3D phase-contrast micro-CT of the sample paraffin block (fig.   5.11) was also made with Avizo software. The histological image was first scaled to the PhC μCT dimensions, and then registered to the corresponding micro-CT slice. Besides appreciating the adequate match between the two methodologies, the hybrid visualization shows that the amount of information available to pathologist narrows down to observing only a small portion of the whole sample. A prepared histological section is representative of only one-thousandth of the thickness of the sample. Virtual histology with PB-μCT offers a better understanding for the characterization of the entire sample, allowing for subsequet characterizations as needed, in contrast to serial sectioning, which can result in the destruction of the sample.

To sum up, the visibility of the invasive micropapillary cystic carcinoma with PB-μCT is
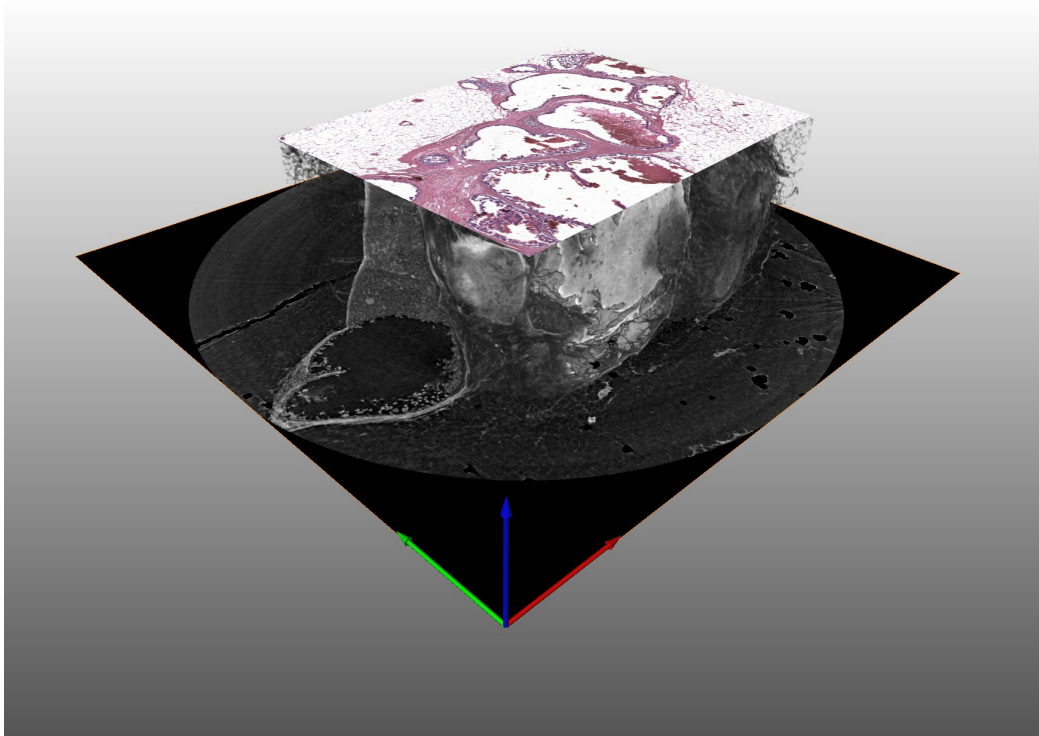
Figure 5.11: Hybrid visualization of the histological cross-section and 3D phase-contrast micro-CT of the IMPIC sample paraffin block. Virtual histology with PB-µCT provides a deeper insight for the characterization of the complete sample. Original image.

comparable to that offered by histology images, providing a better discernability of the stromal/epithelial interface in contrast to conventional H&E image. Moroever, virtual histology with PB-µCT provides two- and three-dimensional data, offering new insights into tissue microstructure while preserving the sample.

5.4.5.4 Invasive lobular carcinoma

The ILC sample was scanned at 4 µm and 1 µm and the resulting tomographic acquisitions were compared to the histological slices. The characteristic single-filed tumor cells of this type of breast lesion, are indicated by the red asterisks in fig. 5.12. It is clearly visible that the tumor cells do not form a solid, uniform lesion, but they are rather arranged in files, between collagen fibers, that are very clearly visible on µCT images. PB-µCT images acquired at 4 µm show the region where the single-file structures are located, but only at the 1 µm resolution images could the single files be identified. Contrarily, in the pancytokeratin stain evidences and allows to quantify the presence of the individual ILC cells.

Limitations of the use of PhC μ CT for ILC should be acknowleded, such as an insufficient spatial resolution to allow a distinction between benign and malignant tissues at a cellular
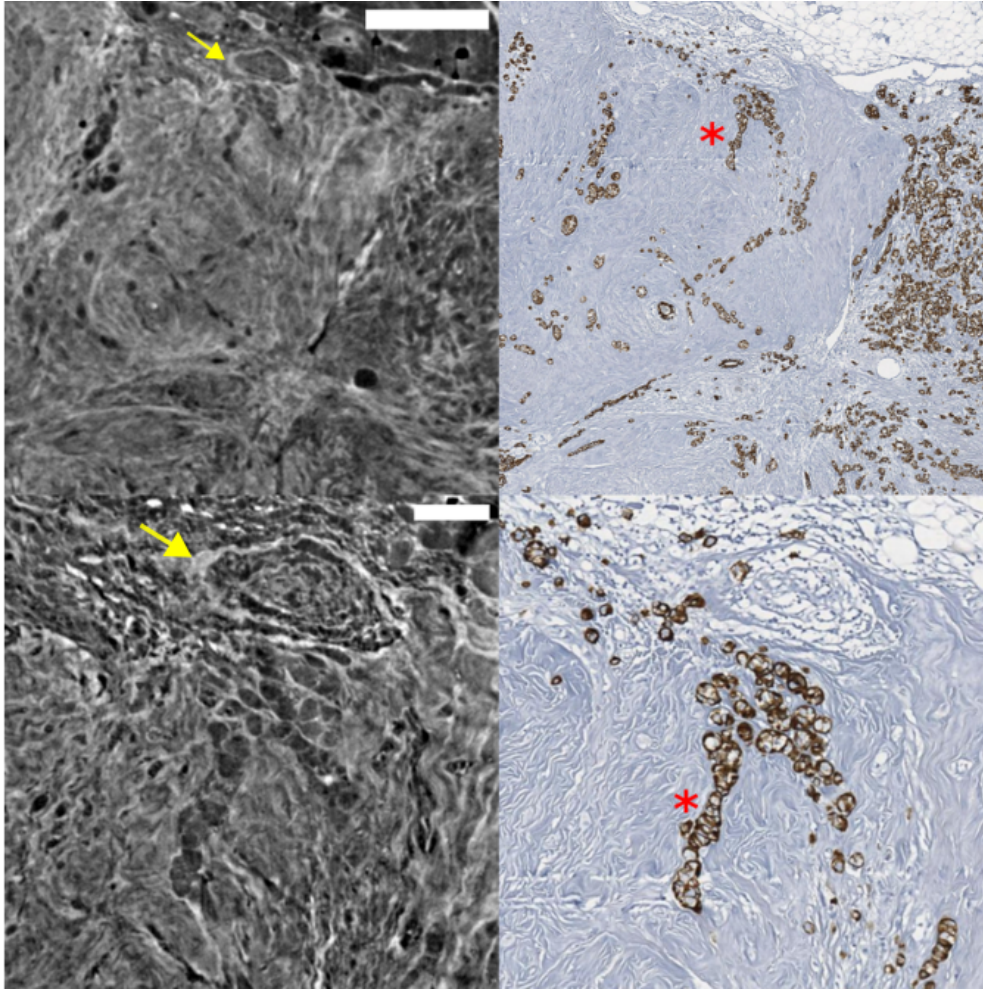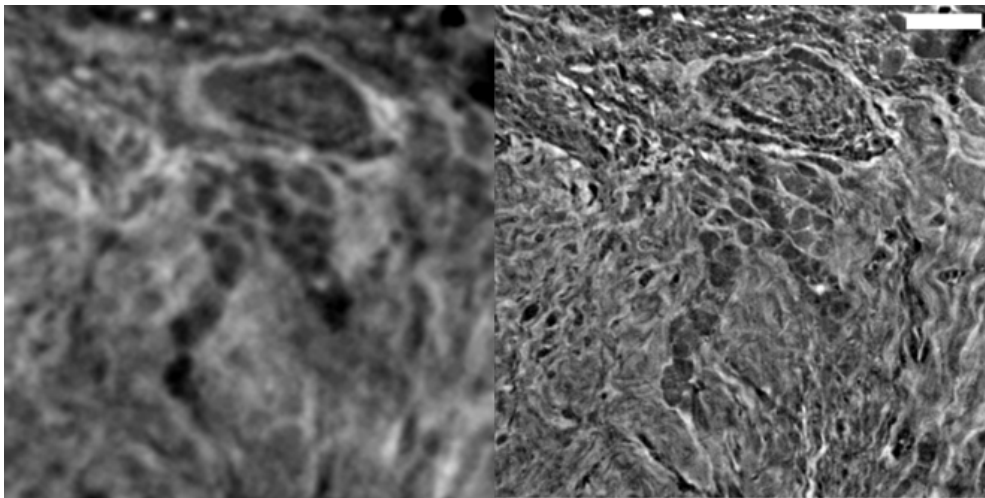
Figure 5.12: A comparison of the visibility of the features of ILC tumor cells. Images with pancytokeratin histological coloring are shown on the right, while the corresponding PB-μCT, acquired at 4 μm (top) and 1 μm (bottom) respectively, can be seen on the left. Pancytokeratin images show tumor cells grouped in single files, cords, and single cells, whereas 1-μm micro-CT scans are able to precisely define the areas occupied by tumor cells in the stroma (red asterisk). For the top and bottom PB-μCT images. Scale bars correspond to 0.5 mm and 0.1 mm, respectively. Original image.

level, as seen in the pancytokeratin stained histological images. It can be concluded that virtual histology with PhC μ CT offers less information about the ILC structure than does conventional histology, yet it does show the characteristic single-file appearance of the lesion.

5.4.6   Image resolution

The combination of parameters applied from the optimization work of Donato et al. (2022a) for propagation phase contrast technique in virtual histology for breast specimens resulted in remarkable visibility of important structural characteristics of the samples, providing images of good quality, with a resolution of details that was comparable to histological methods in

most cases, and in some, higher. The images shown in fig. 5.13 display the considerable image quality gain of the details when changing the employed pixel size from 4 (left) to 1 μm (right). A higher spatial resolution, namely a small pixel size, implied a reduction of the size of the FOV, as it can be appreciated in fig. 5.4, but at the same time, it achieves an increase in the visibility of details that can be useful for clinical investigation . Since a smaller FOV will inevitably require longer acquisition times to cover a larger area of the material, high-resolution scans could be employed to image specific regions of interest, selected by pathologists, for further investigation to complement the current histological procedure .

Figure 5.13: A comparison of the visibility of the features of tumor cells of ILC sample as seen in PB-μCT at different spatial resolutions. On the left side a region of interest of an image taken at 4 μm while on the right side the same region is taken at 1 μm. Scale bar corresponds to 0.1 mm. Original image.

5.4.7 Implications and future directions

The remarkable correspondence between PB-μCT and conventional histology images suggest that virtual histology with PB-μCT images could complement the histological characterization for the presented breast lesions. Despite the numerous staining techniques and the use of microscopy allowing a highly specific analysis down to the (sub)cellular level in conventional histology, the methodology falls short when it comes to acquiring 3D information about tissues. Serial sectioning only partially overcomes this issue, but it is labor- and time-intensive and does not produce true 3D data. Therefore, conventional histology could benefit from the use of 3D volumes generated with PB-μCT since the intrinsic bidimensionality of the histological slides may restrict the understanding and relationship of the original three-dimensional sample structure. In this context, 3D virtual histology could support the missing gap in histo-

logical procedures by providing a global representation of the tissue, thus potentially guiding the pathologist to choose the most suitable direction prior to section cutting to prevent information loss, as well as to provide additional morphological information during the evaluation of surgical margins towards breast-conserving surgery.

An extension on the work of the optimization of PhC μCT for virtual histology of breast tissues can be found in Peña et al. (2022). The research conducted in this thesis on PB-μCT for virtual histology is currently being prepared in a manuscript for publication, where I am the main author. It also lays the foundations towards a larger virtual histology study aiming to assess the invasiveness of malignant diseases, such as in follicular thyroid carcinomas. The technique has also the potential to facilitate future collaborations focused on evaluating chronic pathologies, particularly fibrotic conditions, such as pulmonary fibrosis.

Chapter 6

Multiscale imaging analysis of a breast sample

The previous sections and chapter have demonstrated the potential of PB PhC imaging techniques in meeting the demand for high soft-tissue visibility in biomedical X-ray imaging. It was also proven that by using a coherent photon beam available at synchrotron facilities and long sample-to-detector distances, these techniques are highly effective. Multiscale imaging bridging spatial resolution and FOV from the whole organ/clinical level (100 μm over ¿ 10 cm) to virtual histology level (few μm over few centimeter) is a key to understanding system-level behaviors in health or disease   (Walsh et al., 2021). This chapter explores the use of imaging equipment and techniques described in chapter 4 and in chapter 5 to achieve multiscale imaging of a breast mastectomy sample at the SYRMEP beamline. The resulting images showcase the bridging of spatial resolutions from whole breast imaging with propagation-based breast-CT methodology to virtual histology with propagation-based micro-CT imaging of the same sample. It will be demonstrated in this chapter that multiscale approach has the potential to complement current diagnostic procedures, as the acquired 2D and 3D information can be correspondingly aligned and jointly used in a multidisciplinary clinical context. The work presented in this chapter has recently been submitted for peer review, where I am the principal author of a manuscript, and it is currently being taken into consideration for publication.

6.1   Surgical breast specimen

An entire breast mastectomy sample was extracted from a patient diagnosed with moderately differentiated infiltrating ductal carcinoma following the framework of the operative protocol presented in sec. 5.3. Figure 6.1 shows the radiological pre-operative images of the breast. A pre-operative mediolateral oblique (MLO) mammography image of the breast is shown in the left panel of figure 6.1, and in the right panel, a pre-operative contrast-enhanced T1-weighted MRI image, where the contrast medium's uptake is clearly visible. Although a big malig-

nant mass is seen with both imaging modalities, the visibility of small features, such as the microcalcifications that typically accompany this type of carcinoma, is scarce. In fact, microcalcifications are potentially missed by both screening or pre-surgical imaging, due to the insufficient spatial resolution of attenuation-based x-ray modalities.
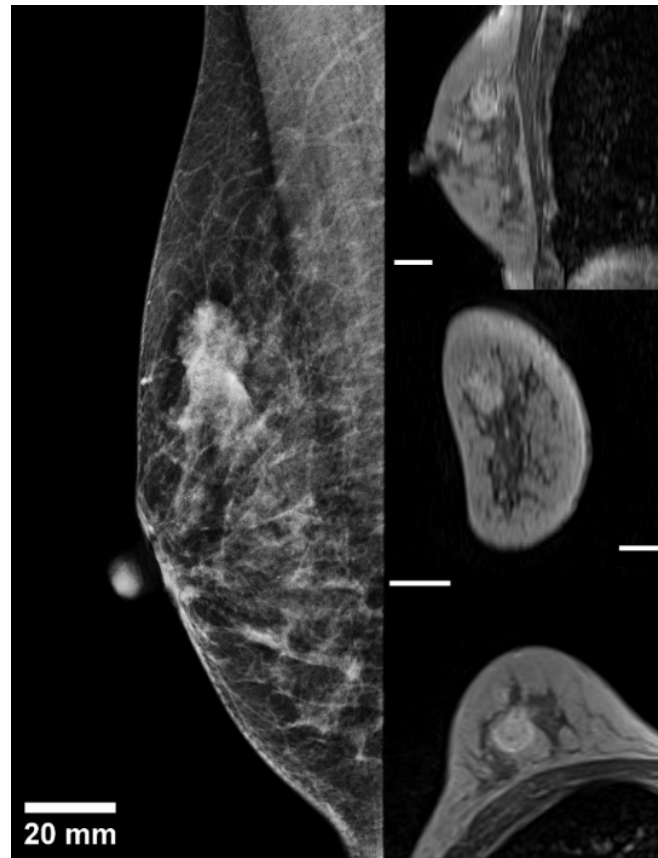
Figure 6.1: On the left, mammography MLO view of the patient. On the right, T1-weighted MRI scans display the uptake contrast agent region with the highlighted mass as seen from three different planes: sagittal (top right), coronal (center right), and transversal (bottom right) All scale bars represent 20 mm. Original image.

Fresh tissue specimens should be appropriately fixed as soon as possible after dissection. In order to obtain a homogeneous fixation, the mastectomy tissue was cut immediately after surgery and infiltrated with liquid formalin before vacuum bag preparation. The breast tissue sample underwent standard tissue processing for histology as explained in sec. 5.1 to create a tissue block of 3.0 cm × 2.5 cm × 0.5 cm. Prior to CT scanning, pathologists cut a 5 micrometers section from the surface of the aforementioned block, which was subsequently stained with standard H&E. The histological section was converted to the digital format by using a D-Sight F 2.0 slide scanner with a 20x magnification and 0.5μm × 0.5μm pixel size.

6.2 Experimental setup

The PB-bCT acquisitions for the whole sample were carried out using the monochromatic beam mode because using low-energy X-rays in the polychromatic X-ray mode attenuate the beam within the sample, resulting in a beam-hardening effect and increased radiation dose rather than image contrast. However, to achieve the high spatial resolution required for virtual histology of the paraffin-block sample using PB-μCT, the white/pink beam mode was necessary to maximize the number of photons hitting the small-pixel indirect-conversion detectors.

6.2.1 Full specimen scan via PB-bCT

The scans of the full mastectomy was performed using the PIXIRAD-8 with monochromatic beam at 32 keV (Oliva et al., 2020), acquiring a total of 1200 equally spaced projections at a MGD of 5 and 20 mGy. The surgical specimen was imaged in a pendant geometry hanging from the patient support in the radiological station, positioned at a 30.0 m distance away from the X-ray source, and at a propagation distance of 1.6 m. The largest portion of the sample that could be imaged during each scan is of 210 mm wide and 5.5 mm high, thus requiring multiple scans to acquire the full sample volume. However, the complete volume acquisition was performed in less than ten minutes. The dedicated pre-processing procedure for compensating detector-specific artifacts, phase-retrieval process and image via a GPU-based Filtered Back-Projection with Shepp-Logan filtering were carried out as explained in chapter 3. Further technical details can be found in Longo et al. (2019) and in table 6.1.

6.2.2 Virtual histology via PB-μCT

The paraffin-embedded block was imaged with polychromatic radiation with an energy range from 10 to 50 keV. The X-ray spectrum, filtered by means of 1.0 mm of Silicon, resulted in an average energy of 20 keV. The sample was positioned in the experimental station of the beamline, at a distance of 23 m from the source. The beam height at this position was approximately 4 mm (FWHM). Acquisitions were performed by using the sCMOS detector tuned to an effective pixel size of 4 μm, resulting in a lateral field of view of approximately 8 mm. The paraffin-embedded block was oriented by placing its longest side parallel to the rotation axis of the acquisition system and placed 500 mm upstream from the detector following the optimization of the experimental setup described in sec. 5.3. The scan of the entire sample required multiple local-area acquisitions (the so-called "Mosaic tomography" (Vescovi et al., 2018)) performed using an in-house built automatic script. Each scan acquired 1800 equally spaced projections, with a total of 24 scans acquired in 120 minutes for the complete paraffin

block. The dedicated pre- and post-processing procedures were carried out as described in sec. 5.3.2 and sec. 5.4.2. More technical information can be found in table 6.1 and in Donato et al. (2022a).

	PB-bCT	PB-μCT
Ring electron energy (GeV)	2.4	2.0
Flux (photons/s/mm^2)	0.8×10^6-3.2×10^6	2.7×10^{11}
Beam modality	monochromatic	polychromatic
Beam energy (keV)	32	20 keV (average)
Detector type	CdTe photon-counting	sCMOS
Pixel size (μm)	60 μm	4
Lateral field of view (mm)	210	8
Propagation distance (mm)	1600	500
Scan time (minutes)	> 10 min	~120 min
δ/β	2308	350

**Table 6.1:** The experimental setup and reconstruction parameters of the two imaging modalities.

6.3   Volume co-registration

PB-bCT and PB-μCT reconstructions allow for interactive virtual visualization of the 3D sample volume. The virtual stack was evaluated with the pathologist, and significant characteristics were manually traced in the specimen's three orthogonal planes. The best tomographic reconstruction slice in the virtual μCT stack was then selected to correspond to the histological section. Avizo 9.3 (Thermo Fisher Scientific Inc, MA, USA) software was used to automatically register the virtual volumes created by PB-bCT and PB-μCT. The program was used to load, scale, and normalize the volumes obtained using the two imaging modalities so that they displayed the same mean gray values in regions of glandular tissue. From the complete volume produced by PB-bCT, a volume of interest (VOI) was chosen to begin the registration process. This selection was guided by the pathologists who sampled the tissue and made the paraffin-embedded block. The digital volume of the block was aligned in 3D using this VOI as a reference by applying rigid transformations (3 rotations and 3 translations) and using a Euclidean distance metric.

6.4   From breast-CT to micro-CT images

Figure 6.2 shows a comparison of PB-bCT slices acquired at 5 (left) and 20 (right) mGy. These images confirm the challenge of differentiating between carcinomas and glandular tissues in breast imaging. There is no clear distinction between the tumor and fibroglandular

tissue, both of which share comparable gray levels, in contrast to adipose tissue. However, the combined effect of PB PhC technique and the application of PhR enhances the visibility of the calcifications that typically accompany this type of carcinoma (green arrows). The lower panels of figure 1 provide the Maximum Intensity Projection (MIP) images of a 4 mm thick slab of the white square area (5 and 20 mGy, respectively) in order to better visualize calcifications. Several microcalcification clusters can be seen in both high and low dosage MIP images. It is clear that the high dose image offers higher visibility overall, allowing a clearer identification of weaker signals arguably due to calcifications smaller than the voxel size (60 μm). The dark air bubbles indicated by the white arrows arose as a result the cut made during the fixation process, as explained in sec. 6.1.
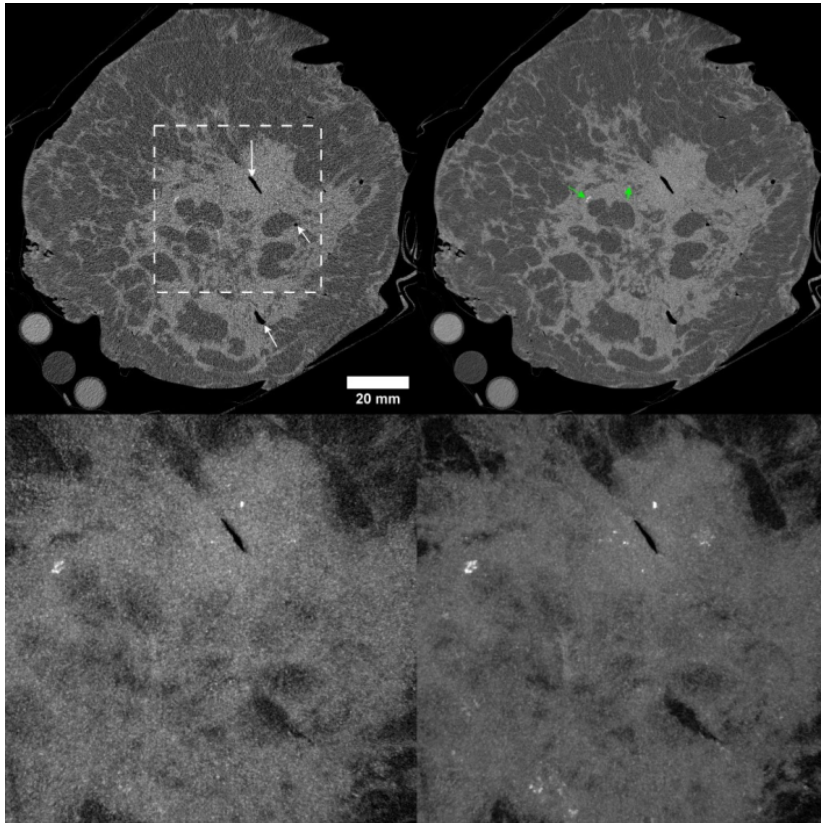
Figure 6.2: PB-bCT images of the sample acquired at 5 (left) and 20 (right) mGy. Top: White arrows denoting air bubbles left over after the formalin fixation and green arrows highlight the presence of microcalcifications. Materials for calibrating the linear attenuation coefficient are depicted as circular features in the lower left corner (Piai et al., 2019). Bottom: the respective MIP of a 4 mm slab corresponding to the white square area in the top right image. Original image.

These images (6.2) demonstrate the potential of PB-bCT as a detection-assisting tool for radiologists, showing a promising 3D evaluation of the glandular structures with a markedly

higher spatial resolution and soft tissue visibility compared to the state-of-the-art radiological imaging techniques, even at clinically acceptable radiation doses (5 mGy). Additionally, because of their excellent signal-to-noise ratio, bCT data acquired at higher radiation doses (20 mGy) enable a very detailed 3D view of the entire breast sample and can be used to create efficient models for virtual clinical trials (Samei et al., 2020). These images have also been already used to create 3D patient-based super-resolution digital breast phantoms (Caballo et al., 2018b), and are generally regarded as the gold standard when developing new image reconstruction and processing algorithms, as described in 4.4.

PB-μCT, on the other hand, can provide high-resolution 3D imaging that might supplement the currently available histological imaging procedures, potentially leading to a more precise and/or effective diagnosis. Figure 6.3 presents the multi-scale transition from whole breast imaging with PB-bCT to virtual histology with PB-μCT imaging. The top section shows a zoomed-in view of a 3D rendering of the tissue volume acquired using PB-μCT (4 μm voxel) alongside an inset of the investigated paraffin-embedded tissue block that has been co-registered. The bottom section compares a 2D slice of the X-ray virtual histology volume with a conventional 2D histology image.

By comparing the μCT slice with the corresponding histological section, the image detail allows identification of the neoplasm as a solid, lobulated tissue with an infiltrative front of invasion and sharp margins. This is well distinguished from the adipose tissue and surrounding parenchyma. The image detail also allows recognition of the thickened basement membrane of the ducts involved in intraductal carcinoma and the type of intraepithelial growth. The features indicated by the green arrows denote reconstruction artifacts. The calcifications (red arrows) are clearly visible in both PB-bCT and virtual histology scans. However, microcalcifications can potentially be missed by screening or presurgical imaging due to insufficient spatial resolution (see sec. 1.2, and their presence may be compromised during the thin histological slice preparation. When paraffin blocks are prepared, calcifications may dissolve during processing or, in some cases, they can fall out from the slice of interest during section cutting, potentially damaging the surrounding tissue if the cutting blade drags the calcification, as it is the case shown by the blue arrow in figure 6.3. The images also demonstrates the limited portion of the tissue that the pathologist can examine compared to the whole tissue acquired with PB-bCT (upper panel) and the paraffin-embedded block that can be scanned with PB-μCT (insert and bottom panel). A histological section represents only a small fraction (4-5 μm) of the thickness

of the paraffin-embedded tissue block (3-5 mm of the tissue height).

6.5 Improving clinical decisions with multiscale imaging

The PhC multi-scale approach offers a more comprehensive understanding of the whole breast by providing two- and three-dimensional information in different planes at various resolutions. This multiscale imaging approach enables bridging spatial resolution and FOV from the whole organ/clinical level (100 μm over ¿ 10 cm) to the virtual histology level (a few μm over a few centimeters), which is crucial for understanding system-level behaviors in health or disease (Walsh et al., 2021). This technique has the potential to complement various diagnostic procedures conducted in the clinical setting, which can benefit health professionals from diverse interdisciplinary environments in their efforts to combat breast cancer-related deaths.

An example is the 3D evaluation of the glandular structures with a significantly higher spatial resolution and soft tissue visibility offered by PB-bCT at clinically acceptable radiation doses (5 mGy), thanks to its excellent signal-to-noise ratio, demonstrates to be a potentially useful tool for radiologists for a more accurate detection of breast cancer, hence, that can possibly improve the diagnosis and treatment outcomes for patients. Another example of the benefits of using a multi-scale approach for analyzing the whole specimen down to the paraffin block is that it could assist pathologists in obtaining a better understanding of the complete sample, potentially leading to a more accurate diagnosis. By evaluating the entire sample volume from PB-bCT data, the pathologist could identify the most indicative region and the plane of pathological interest before extracting the samples for histology procedures. The selected paraffin-embedded block can then be imaged using PB-μCT, providing a high-resolution 3D representation that can guide tissue sectioning of a diagnostically pertinent area. By presenting virtual and conventional histology images side by side, the pathologist can potentially identify numerous relevant tissue structures and gain complementary information that aids in the diagnosis of breast lesions. Moreover, PB-μCT may contain additional structural information of the sample, such as evidence of microinfiltrations located deeper in the block, that might be otherwise missed by the pathologist. In cases of extensive carcinomas in-situ, where the lesion appears as a large area of microcalcifications rather than a mass, inspecting the entire block in 3D could highlight areas of infiltration located deeper in the tissue that might be missed by a single standard section. This could help in correctly staging the neoplasm and establishing the most suitable treatment for the patient.

The advantages of PB PhC imaging over other standard techniques have generated signif-

icant interest as a potential tool for clinical use. However, the lack of access to synchrotron radiation sources for the general population has hindered its widespread clinical implementation. To address this issue, new compact laboratory X-ray sources that provide high spatial coherence and high flux are being developed, potentially enabling the translation of PB PhC imaging to clinical environments (Hornberger et al., 2019; Faillace et al., 2019). A PB breast tomosynthesis system has already been developed and is currently under clinical evaluation (Ghani et al., 2021). Alternatively, source coherence requirements can be relaxed by inserting X-ray optical devices that are compatible with conventional X-ray tubes. A promising development towards clinical application of PhC imaging has been made in chest imaging using grating interferometry techniques and an X-ray tube (Gassert et al., 2021). As for μCT systems for virtual histology, multiple studies using compact sources and various phase-sensitive techniques have been reported, such as grating interferometry (Birnbacher et al., 2021; Kimm et al., 2020), edge illumination techniques (Massimi et al., 2021, 2022), or PB (Twengström et al., 2022). However, the images generated do not exhibit the spatial and contrast resolution attainable with synchrotron radiation.

Multiscale imaging with PB PhC CT has the potential to reinforce clinical care by providing innovative imaging tools that can improve the accuracy of diagnoses and, in turn, could establish the most suitable treatment course for the patient. The optimization of techniques that enable multiscale phase-contrast imaging of the breast presented in this chapter have been addressed in a manuscript, where I am the main author as mentioned previously, that has been recently submitted for peer-review and is currently under consideration for publication.
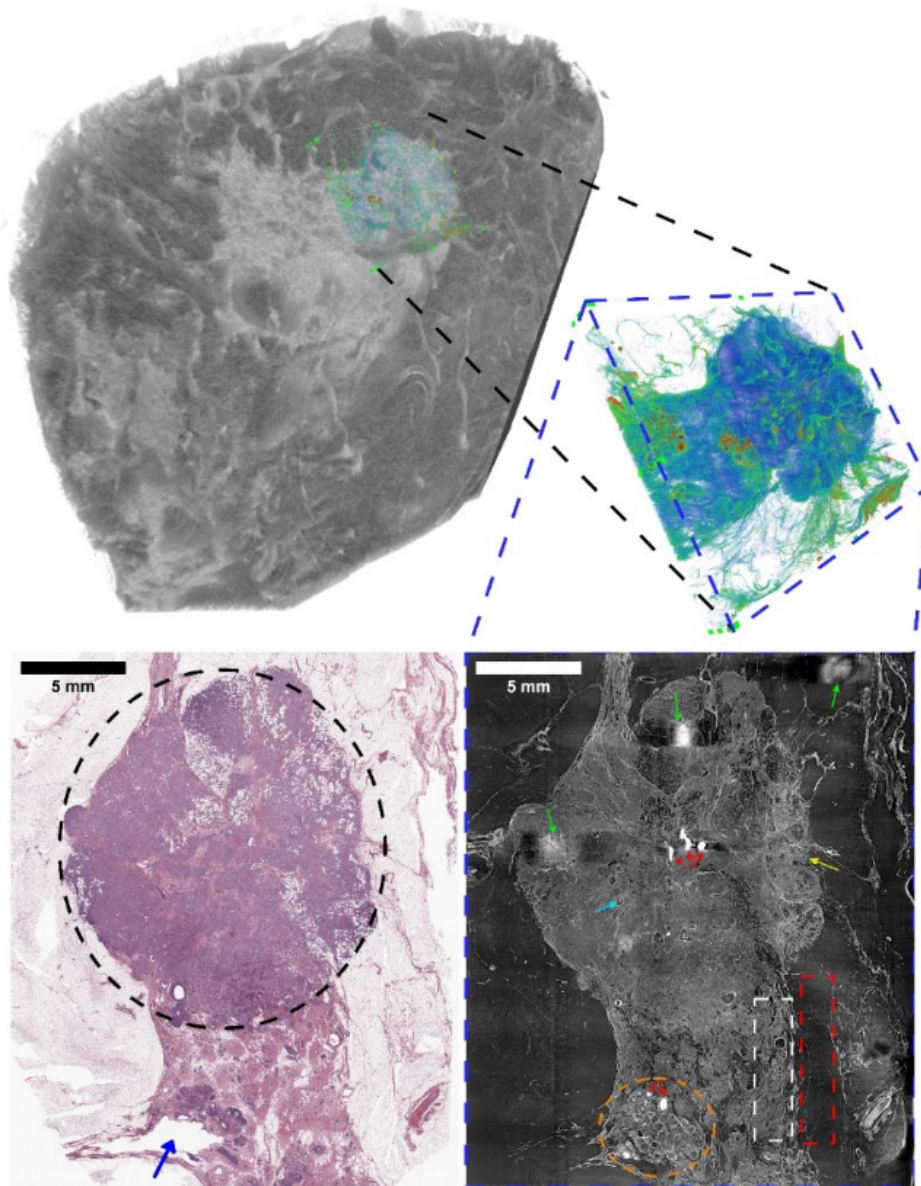
Figure 6.3: Multi-scale imaging of sample 1. Top, PB-bCT scan of the whole breast with an inset of the paraffin-embedded tissue block, enlarged to the left to display the tissue volume obtained by PB-μCT. Bottom, a 2D virtual histology slice (right) and its corresponding standard 2D histology image (left). The neoplasm, which appears as a solid, lobulated tissue, is enclosed by the black ellipse. The invasive tumor front is indicated by the yellow arrow. An in-situ extralesional region (solid, cribriform with microcalcifications) is enclosed by the orange ellipse. The presence of an in-situ intralesional component is indicated by the cyan arrow. The adipose tissue and the typical fibroglandular tissue between the neoplasia and in-situ component are indicated by red and white dashed rectangles respectively. Microcalcifications are denoted by red arrows, while reconstruction artifacts are denoted by green arrows. The blue arrow shows the tissue damage risen during section cutting due to presence of microcalcifications. Original image.

Chapter 7

Conclusions

Different approaches to address breast cancer detection and disease management are a driving force towards reducing breast cancer-related fatalities. Medical physicists are part of such driving force by contributing with analytical and problem-solving skills applied to a clinical setting, and by ensuring the safe and effective practices of ionizing radiation in an imaging facility. The spectrum of subjects and challenges covered in this work is fairly extensive, as breast cancer is fought in a multidisciplinary context. The topics ranged from comprising breast dosimetric models in conventional x-ray imaging, to the uses of phase-contrast tomography for an innovative setup in a breast examination, and collaboratively working one-on-one with another health professional, for a better characterization of breast tissues and lesions.

Various experimental studies carried out in this thesis, as part of SYRMA-3D projects, help to bring propagation-based phase-contrast breast CT closer to the ambitious goal of establishing a clinical setting of breast CT into a synchrotron facility. To ensure high-quality images in PB-bCT, the proposed methods in this thesis approached the patient motion issue and potential compensatory procedures by developing a breast immobilization device and by assessing patient breathing motion to generate a corrective mechanism to compensate for such motions. Another important approach was the optimization of a dedicated iterative reconstruction algorithm to ensure the best possible image quality in a clinical PB-bCT setting. The optimization provided the most favorable combinations of algorithm parameters while preserving image quality with a high degree of flexibility for image reconstruction.

Although breast cancer is typically detected by imaging the entire breast, a definite case of breast cancer is only identified on a micrometric level by histological slicing using small samples. In this context, a potential adjuvant tool for tissue characterization in histological processes has been demonstrated by the use of phase-contrast micro-CT for virtual histology

studies of breast samples. The proposed method might aid other healthcare professionals in getting a better understanding of the disease environment and choose an appropriate therapeutic course.

The Elettra-based breast CT experiment detailed in this thesis is just one of the ongoing or upcoming breast clinical projects in synchrotron facilities, such as in ANSTO, with whom there is an ongoing collaboration. In this thesis, two collaborative research initiatives with ANSTO were described. The Indian Synchrotron Facility (Indus-2) researchers also have similar interests (Sharma et al., 2019). As part of the Elettra 2.0 upgrade program, the construction of a new beamline dedicated to imaging applications in the life sciences is envisaged, with a much wider x-ray energy spectrum and a flux many orders of magnitude higher than SYRMEP. The program includes the construction of a hutch dedicated to clinical imaging, where conditions for breast CT as well as lung imaging will be optimized, as encouraging results on human-scale samples been reported (Wagner et al., 2018).

In short, the research aimed to demonstrate the benefits of phase-contrast tomography and its influence in one of the most challenging x-ray imaging techniques: breast imaging. Specifically, this work showed the capability of PB PhC CT to strengthen clinical care by offering advanced imaging techniques that can enhance the precision of diagnoses by

- scanning and analyzing full-volume breast samples with PB-bCT at clinically acceptable radiation dose levels.

- using PhC μ-CT as a supplemental 3D staging tool in histological procedures in breast samples.

The findings reported in this work have already been documented in five distinct papers in scholarly journals, including Medical Physics, Journal of Instrumentation, Physics in Medicine and Biology, and SPIE Proceedings, with other two upcoming manuscripts reporting the latest findings being submitted.

This thesis work has made significant advancements in evaluating phase-contrast computed tomography as a means for breast imaging in a multiscale approach. These radiological synchrotron applications widen the horizons by demonstrating the benefits of phase-contrast imaging either for diagnostic purposes or as a staging complementary tool, as well as presenting the challenges and limitations that need to be addressed for the technique to become available in clinical settings. An example is the implementation of new compact laboratory X-ray

sources that produce enough flux and spatial coherence to be used for phase-contrast imaging of biomedical samples. These sources present greater availability, compactness, and lower cost compared to synchrotrons, that could lead the transition of multiscale imaging with PB PhC CT from synchrotrons to a clinical practice in hospitals, improving X-ray diagnostic methods and determining the best treatment options for patients accessible to a large population.

.

Bibliography

Icru report 44, tissue substitutes in radiation dosimetry and measurement. Technical Report DOE-SLC-6903-1, International Commission on Radiation Units and Measurements, Bethesda, MD (United States), 1 1989. [Cited on page 99.]

Medical imaging, implementation of x-ray phase-contrast tomography to transform cancer diagnosis, 2023. URL https://impact-mi.sydney.edu.au. [Cited on pages 60 and 86.]

AAPM. The future of medical physics - medical phyics 3.0. URL https://mp30.aapm.org/. [Cited on pages 12 and 16.]

AAPM. Task group no. 282 - development of a new universal breast dosimetry method (tg282), 2022. URL https://www.aapm.org/org/structure/default.asp?committee_code=TG282. [Cited on page 45.]

AB-CT. Advanced breast-CT, 2022. URL https://www.ab-ct.com/nuview/. [Cited on page 26.]

A. Abrami, F. Arfelli, R. Barroso, A. Bergamaschi, F. Bille, P. Bregant, F. Brizzi, K. Casarin, E. Castelli, V. Chenda, et al. Medical applications of synchrotron radiation at the syrmep beamline of elettra. *Nuclear Instruments and Methods in Physics Research Section A: Accelerators, Spectrometers, Detectors and Associated Equipment*, 548(1-2):221–227, 2005. [Cited on pages 37 and 42.]

S. Agostinelli, J. Allison, K. Amako, and J. A. et al. Geant4—a simulation toolkit. *Nuclear Instruments and Methods in Physics Research Section A: Accelerators, Spectrometers, Detectors and Associated Equipment*, 506(3):250 – 303, 2003. ISSN 0168-9002. doi: https://doi.org/10.1016/S0168-9002(03)01368-8. URL http://www.sciencedirect.com/science/article/pii/S0168900203013688. [Cited on page 54.]

J. Albers, M. A. Markus, F. Alves, and C. Dullin. X-ray based virtual histology allows guided

sectioning of heavy ion stained murine lungs for histological analysis. *Scientific reports*, 8 (1):1–10, 2018a. [Cited on page 112.]

J. Albers, S. Pacilé, M. A. Markus, M. Wiart, G. Vande Velde, G. Tromba, and C. Dullin. X-ray-based 3d virtual histology—adding the next dimension to histological analysis. *Molecular Imaging and Biology*, 20(5):732–741, 2018b. [Cited on pages 111 and 112.]

J. Albers, S. Pacilé, M. A. Markus, M. Wiart, G. V. Velde, G. Tromba, and C. Dullin. X-ray-based 3d virtual histology—adding the next dimension to histological analysis. *Molecular Imaging and Biology*, 20(5):732–741, 2018c. [Cited on page 112.]

L. Arana Peña, C. Fedon, E. Garcia, O. Diaz, R. Longo, D. Dance, and I. Sechopoulos. Monte carlo dose evaluation of different fibroglandular tissue distribution in breast imaging. In *15th International Workshop on Breast Imaging (IWBI2020)*, volume 11513, pages 117–122. SPIE, 2020. [Cited on page 46.]

L. M. Arendt, J. A. Rudnick, P. J. Keller, and C. Kuperwasser. Stroma in breast development and disease. *Seminars in Cell and Developmental Biology*, 21:11–18, 2010. ISSN 10849521. doi: 10.1016/j.semcdb.2009.10.003. [Cited on page 124.]

F. Arfelli, M. Assante, V. Bonvicini, A. Bravin, G. Cantatore, E. Castelli, L. Dalla Palma, M. Di Michiel, R. Longo, A. Olivo, et al. Low-dose phase contrast X-ray medical imaging. *Physics in Medicine & Biology*, 43(10):2845, 1998. doi: 10.1088/0031-9155/43/10/013. [Cited on pages 34, 37, and 39.]

F. Arfelli, V. Bonvicini, A. Bravin, G. Cantatore, E. Castelli, L. D. Palma, M. D. Michiel, M. Fabrizioli, R. Longo, R. H. Menk, et al. Mammography with synchrotron radiation: phase-detection techniques. *Radiology*, 215(1):286–293, 2000. [Cited on pages 36 and 37.]

F. Arfelli, A. Abrami, P. Bregant, V. Chenda, M. A. Cova, F. de Guarrini, D. Dreossi, R. Longo, R.-H. Menk, E. Quai, et al. Synchrotron radiation mammography: clinical experimentation. In *AIP Conference Proceedings*, volume 879, pages 1895–1898. American Institute of Physics, 2007. [Cited on page 37.]

V. Astromskas, E. N. Gimenez, A. Lohstroh, and N. Tartoni. Evaluation of polarization effects of e- collection Schottky CdTe Medipix3RX hybrid pixel detector. *IEEE Transactions on Nuclear Science*, 63(1):252–258, 2016. doi: 10.1109/tns.2016.2516827. [Cited on page 63.]

F. Attix. Introduction to radiological physics and radiation dosimetry. usa, john wiley and sons, 1986. [Cited on page 21.]

A. Aydiner, A. Igci, and A. Soran. *Breast Disease*, volume 1. Springer Cham, Switzerland, second edition edition, 2019. doi: https://doi.org/10.1007/978-3-030-04606-4. [Cited on pages 15, 17, and 18.]

M. S. Bae, W. K. Moon, J. M. Chang, H. R. Koo, W. H. Kim, N. Cho, A. Yi, B. La Yun, S. H. Lee, M. Y. Kim, et al. Breast cancer detected with screening us: reasons for nondetection at mammography. *Radiology*, 270(2):369–377, 2014. [Cited on page 23.]

R. Ballabriga, J. Alozy, M. Campbell, E. Frojdh, E. Heijne, T. Koenig, X. Llopart, J. Marchal, D. Pennicard, T. Poikela, et al. Review of hybrid pixel detector readout ASICs for spectroscopic X-ray imaging. *Journal of Instrumentation*, 11(01):P01007, 2016. [Cited on page 61.]

Y. Baneva, K. Bliznakova, L. Cockmartin, S. Marinov, I. Buliev, G. Mettivier, H. Bosmans, P. Russo, N. Marshall, and Z. Bliznakov. Evaluation of a breast software model for 2d and 3d x-ray imaging studies of the breast. *Physica Medica*, 41:78–86, 2017. [Cited on page 48.]

P. Baran, S. Pacile, Y. I. Nesterets, S. Mayo, C. Dullin, D. Dreossi, F. Arfelli, D. Thompson, D. Lockie, M. McCormack, et al. Optimization of propagation-based x-ray phase-contrast tomography for breast cancer imaging. *Physics in Medicine & Biology*, 62(6):2315. [Cited on page 103.]

P. Baran, S. Mayo, M. McCormack, S. Pacile, G. Tromba, C. Dullin, F. Zanconati, F. Arfelli, D. Dreossi, J. Fox, Z. Prodanovic, M. Cholewa, H. Quiney, M. Dimmock, Y. Nesterets, D. Thompson, P. Brennan, and T. Gureyev. High-Resolution X-Ray Phase-Contrast 3-D Imaging of Breast Tissue Specimens as a Possible Adjunct to Histopathology. *IEEE Transactions on Medical Imaging*, 37(12):2642–2650, Dec. 2018a. ISSN 0278-0062, 1558-254X. doi: 10.1109/TMI.2018.2845905. URL https://ieeexplore.ieee.org/document/8379447/. [Cited on page 112.]

P. Baran, S. Mayo, M. McCormack, S. Pacilè, G. Tromba, C. Dullin, F. Zanconati, F. Arfelli, D. Dreossi, J. Fox, et al. High-resolution x-ray phase-contrast 3-d imaging of breast tissue specimens as a possible adjunct to histopathology. *IEEE transactions on medical imaging*, 37(12):2642–2650, 2018b. [Cited on page 112.]

BCSC. Breast cancer surveillance consortium, 2022. URL http://www.bcsc-research.org/. The Breast Cancer Surveillance Consortium and its data collection and sharing activities are funded by grants from the National Cancer Institute (P01CA154292, U54CA163303), Patient-Centered Outcomes Research Institute (PCS-1504-30370), and Agency for Health Research and Quality (R01 HS018366-01A1). [Cited on page 30.]

J. Bednar and T. Watt. Alpha-trimmed means and their relationship to median filters. *IEEE Transactions on acoustics, speech, and signal processing*, 32(1):145–153, 1984. [Cited on page 69.]

R. Bellazzini, G. Spandre, A. Brez, M. Minuti, M. Pinchera, and P. Mozzo. Chromatic X-ray imaging with a fine pitch cdte sensor coupled to a large area photon counting pixel asic. *Journal of Instrumentation*, 8(02):C02028, 2013. doi: 10.1088/1748-0221/8/02/C02028. [Cited on page 61.]

R. B. Benítez, R. Ning, D. Conover, and S. Liu. NPS characterization and evaluation of a cone beam CT breast imaging system. *Journal of X-ray science and technology*, 17(1):17–40, 2009. doi: 10.3233/XST-2009-0213. [Cited on page 27.]

N. Berger, M. Marcon, N. Saltybaeva, W. A. Kalender, H. Alkadhi, T. Frauenfelder, and A. Boss. Dedicated breast computed tomography with a photon-counting detector: Initial results of clinical in vivo imaging. *Investigative radiology*, 2019. doi: 10.1097/RLI.0000000000000552. [Cited on page 26.]

E. A. Berns, J. Baker, L. Barke, et al. Digital mammography quality control manual. *American College of Radiology. Reston, Va*, 2016. [Cited on page 47.]

R. Betancourt-Benitez, R. Ning, D. L. Conover, and S. Liu. Composite modulation transfer function evaluation of a cone beam computed tomography breast imaging system. *Optical Engineering*, 48(11):117002, 2009. doi: 10.1117/1.3258348. [Cited on page 27.]

L. Birnbacher, E.-M. Braig, D. Pfeiffer, F. Pfeiffer, and J. Herzen. Quantitative x-ray phase contrast computed tomography with grating interferometry: Biomedical applications of quantitative x-ray grating-based phase contrast computed tomography. *European Journal of Nuclear Medicine and Molecular Imaging*, pages 1–18, 2021. doi: 10.1007/s00259-021-05259-6. [Cited on page 138.]

R. J. Bleicher and M. Morrow. Mri and breast cancer: role in detection, diagnosis, and staging. *Oncology*, 21(12):1521, 2007. [Cited on page 28.]

T. Bonacho, F. Rodrigues, and J. Liberal. Immunohistochemistry for diagnosis and prognosis of breast cancer: a review. *Biotechnic & Histochemistry*, 95(2):71–91, 2020. [Cited on page 120.]

J. M. Boone. Glandular breast dose for monoenergetic and high-energy x-ray beams: Monte carlo assessment. *Radiology*, 213(1):23–37, 1999. [Cited on pages 47, 48, and 79.]

J. M. Boone. Normalized glandular dose (dgn) coefficients for arbitrary x-ray spectra in mammography: Computer-fit values of monte carlo derived data. *Medical physics*, 29(5):869–875, 2002. [Cited on page 48.]

J. M. Boone, T. R. Nelson, K. K. Lindfors, and J. A. Seibert. Dedicated breast CT: radiation dose and image quality evaluation. *Radiology*, 221(3):657–667, 2001. doi: 10.1148/radiol.2213010334. [Cited on pages 25 and 26.]

J. M. Boone, A. L. Kwan, K. Yang, G. W. Burkett, K. K. Lindfors, and T. R. Nelson. Computed tomography for imaging the breast. *Journal of mammary gland biology and neoplasia*, 11 (2):103–111, 2006. [Cited on page 27.]

M. Born and E. Wolf. Principles of optics, 7th (expanded) ed. *Cambridge U. Press, Cambridge, UK*, 890, 1999. doi: 10.1017/CBO9781139644181. [Cited on page 33.]

A. Brahme. *Comprehensive biomedical physics*. Newnes, 2014. [Cited on page 41.]

A. Bravin, P. Coan, and P. Suortti. X-ray phase-contrast imaging: from pre-clinical applications towards clinics. *Physics in Medicine & Biology*, 58(1):R1, 2012. doi: 10.1088/0031-9155/58/1/R1. [Cited on pages 35 and 41.]

F. Bray, M. Laversanne, E. Weiderpass, and I. Soerjomataram. The ever-increasing importance of cancer as a leading cause of premature death worldwide. *Cancer*, 127(16):3029–3030, 2021. doi: https://doi.org/10.1002/cncr.33587. URL https://acsjournals.onlinelibrary.wiley.com/doi/abs/10.1002/cncr.33587. [Cited on pages 11 and 15.]

L. Brombal. *X-ray Phase-Contrast Tomography*. Springer Theses. Springer International Publishing, 2020a. [Cited on page 37.]

L. Brombal. Effectiveness of x-ray phase-contrast tomography: effects of pixel size and magnification on image noise. *Journal of Instrumentation*, 15(01):C01005, 2020b. doi: 10.1088/1748-0221/15/01/C01005. [Cited on pages 77 and 113.]

L. Brombal. *X-ray phase-contrast tomography: Underlying Physics and Developments for Breast Imaging*. Springer Nature, 2020c. [Cited on pages 34, 36, 61, 64, and 68.]

L. Brombal, S. Donato, F. Brun, P. Delogu, V. Fanti, P. Oliva, L. Rigon, V. Di Trapani, R. Longo, and B. Golosio. Large-area single-photon-counting cdte detector for synchrotron radiation computed tomography: a dedicated pre-processing procedure. *Journal of Synchrotron Radiation*, 25(4), 2018a. doi: 10.1107/S1600577518006197. [Cited on pages 63, 70, 74, 92, 99, and 105.]

L. Brombal, S. Donato, D. Dreossi, F. Arfelli, D. Bonazza, A. Contillo, P. Delogu, V. Di Trapani, B. Golosio, G. Mettivier, et al. Phase-contrast breast CT: the effect of propagation distance. *Physics in Medicine & Biology*, 63(24):24NT03, 2018b. doi: 10.1088/1361-6560/aaf2e1. [Cited on pages 64, 65, 66, 77, and 113.]

L. Brombal, B. Golosio, F. Arfelli, D. Bonazza, A. Contillo, P. Delogu, S. Donato, G. Mettivier, P. Oliva, L. Rigon, et al. Monochromatic breast computed tomography with synchrotron radiation: phase-contrast and phase-retrieved image comparison and full-volume reconstruction. *Journal of Medical Imaging*, 6(3):031402, 2018c. doi: 10.1117/1.JMI.6.3.031402. [Cited on pages 59, 60, 64, 68, 77, 92, and 99.]

L. Brombal, F. Arfelli, P. Delogu, S. Donato, G. Mettivier, K. Michielsen, P. Oliva, A. Taibi, I. Sechopoulos, R. Longo, et al. Image quality comparison between a phase-contrast synchrotron radiation breast ct and a clinical breast ct: a phantom based study. *Scientific reports*, 9(1):1–12, 2019. [Cited on pages 60, 61, and 103.]

L. Brombal, L. M. Arana Peña, F. Arfelli, R. Longo, F. Brun, A. Contillo, F. Di Lillo, G. Tromba, V. Di Trapani, S. Donato, et al. Motion artifacts assessment and correction using optical tracking in synchrotron radiation breast ct. *Medical Physics*, 2021. [Cited on pages 77, 89, 92, 93, 96, and 97.]

F. Brun, S. Pacilè, A. Accardo, G. Kourousias, D. Dreossi, L. Mancini, G. Tromba, and R. Pugliese. Enhanced and flexible software tools for x-ray computed tomography at the

italian synchrotron radiation facility elettra. *Fundamenta Informaticae*, 141(2-3):233–243, 2015. [Cited on page 64.]

F. Brun, L. Massimi, M. Fratini, D. Dreossi, F. Billé, A. Accardo, R. Pugliese, and A. Cedola. SYRMEP Tomo Project: a graphical user interface for customizing CT reconstruction workflows. *Advanced Structural and Chemical Imaging*, 3(1):4, Jan. 2017. ISSN 2198-0926. doi: 10.1186/s40679-016-0036-8. URL https://doi.org/10.1186/s40679-016-0036-8. [Cited on pages 69, 94, 99, and 115.]

F. Brun, V. Di Trapani, D. Dreossi, L. Rigon, R. Longo, and P. Delogu. Towards in vivo k-edge X-ray micro-CT with the pixirad-i/pixie-iii detector. In *World Congress on Medical Physics and Biomedical Engineering 2018*, pages 123–126. Springer, 2019. doi: 10.1007/978-981-10-9035-6_22. [Cited on page 63.]

A. Burvall, U. Lundström, P. A. Takman, D. H. Larsson, and H. M. Hertz. Phase retrieval in X-ray phase-contrast imaging suitable for tomography. *Optics express*, 19(11):10359–10376, 2011. doi: 10.1364/OE.19.010359. [Cited on page 68.]

R. Butler, E. F. Conant, and L. Philpotts. Digital breast tomosynthesis: What have we learned? *Journal of Breast Imaging*, 1(1):9–22, 2019. [Cited on page 25.]

T. M. Buzug. Computed tomography. In *Springer Handbook of Medical Technology*, pages 311–342. Springer, 2011. doi: 10.1007/978-3-540-39408-2. [Cited on page 69.]

M. Caballo, J. M. Boone, R. Mann, and I. Sechopoulos. An unsupervised automatic segmentation algorithm for breast tissue classification of dedicated breast computed tomography images. *Medical Physics*, 45(6):2542–2559, 2018a. doi: 10.1002/mp.12920. URL https://aapm.onlinelibrary.wiley.com/doi/abs/10.1002/mp.12920. [Cited on page 50.]

M. Caballo, C. Fedon, L. Brombal, R. Mann, R. Longo, and I. Sechopoulos. Development of 3d patient-based super-resolution digital breast phantoms using machine learning. *Physics in Medicine & Biology*, 63(22):225017, 2018b. [Cited on page 136.]

M. Caballo, K. Michielsen, C. Fedon, and I. Sechopoulos. Towards 4d dedicated breast ct perfusion imaging of cancer: development and validation of computer simulated images. *Physics in Medicine & Biology*, 64(24):245004, 2019. [Cited on page 97.]

M. Caballo, C. Rabin, C. Fedon, A. Rodríguez-Ruiz, O. Diaz, J. M. Boone, D. R. Dance, and I. Sechopoulos. Patient-derived heterogeneous breast phantoms for advanced dosimetry in mammography and tomosynthesis. *Medical physics*, 49(8):5423–5438, 2022. [Cited on page 57.]

C. Canelo-Aybar, M. Posso, N. Montero, I. Solà, Z. Saz-Parkinson, S. W. Duffy, M. Follmann, A. Gräwingholt, P. Giorgi Rossi, and P. Alonso-Coello. Benefits and harms of annual, biennial, or triennial breast cancer mammography screening for women at average risk of breast cancer: a systematic review for the european commission initiative on breast cancer (ecibc). *British journal of cancer*, 126(4):673–688, 2022. [Cited on page 15.]

E. Castelli, F. Arfelli, D. Dreossi, R. Longo, T. Rokvic, M. A. Cova, E. Quaia, M. Tonutti, F. Zanconati, A. Abrami, et al. Clinical mammography at the syrmep beam line. *Nuclear Instruments and Methods in Physics Research Section A: Accelerators, Spectrometers, Detectors and Associated Equipment*, 572(1):237–240, 2007. [Cited on page 38.]

E. Castelli, M. Tonutti, F. Arfelli, R. Longo, E. Quaia, L. Rigon, D. Sanabor, F. Zanconati, D. Dreossi, A. Abrami, et al. Mammography with synchrotron radiation: first clinical experience with phase-detection technique. *Radiology*, 259(3):684–694, 2011. doi: 10.1148/radiol.11100745. [Cited on pages 39, 40, and 59.]

R. Chen, R. Longo, L. Rigon, F. Zanconati, A. De Pellegrin, F. Arfelli, D. Dreossi, R. Menk, E. Vallazza, T. Xiao, et al. Measurement of the linear attenuation coefficients of breast tissues by synchrotron radiation computed tomography. *Physics in Medicine & Biology*, 55 (17):4993, 2010. doi: 10.1088/0031-9155/55/17/008. [Cited on pages 21 and 22.]

P. Cloetens, M. Pateyron-Salomé, J. Buffiere, G. Peix, J. Baruchel, F. Peyrin, and M. Schlenker. Observation of microstructure and damage in materials by phase sensitive radiography and tomography. *Journal of Applied Physics*, 81(9):5878–5886, 1997. doi: 10.1063/1.364374. [Cited on page 60.]

A. Contillo, A. Veronese, L. Brombal, S. Donato, L. Rigon, A. Taibi, G. Tromba, R. Longo, and F. Arfelli. A proposal for a quality control protocol in breast CT with synchrotron radiation. *Radiology and Oncology*, 52(3):1–8, 2018. doi: 10.2478/raon-2018-0015. [Cited on pages 75, 76, and 98.]

J. R. Cunningham and H. E. Johns. The physics of radiology. *Springfield: Charles C. Thosmas*, 1983. doi: 10.1118/1.595545. [Cited on pages 20 and 21.]

D. Dance. Monte-carlo calculation of conversion factors for the estimation of mean glandular breast dose. *Physics in Medicine & Biology*, 35(9):1211, 1990. [Cited on pages 46, 47, and 79.]

D. Dance, C. Skinner, K. Young, J. Beckett, and C. Kotre. Additional factors for the estimation of mean glandular breast dose using the uk mammography dosimetry protocol. *Physics in medicine & biology*, 45(11):3225, 2000. [Cited on pages 45 and 46.]

D. Dance, K. Young, and R. Van Engen. Estimation of mean glandular dose for breast tomosynthesis: factors for use with the uk, european and iaea breast dosimetry protocols. *Physics in Medicine & Biology*, 56(2):453, 2010. [Cited on page 48.]

D. R. Dance and I. Sechopoulos. Dosimetry in x-ray-based breast imaging. *Physics in Medicine and Biology*, 61(19):R271–R304, Oct. 2016a. ISSN 0031-9155, 1361-6560. doi: 10.1088/0031-9155/61/19/R271. URL http://stacks.iop.org/0031-9155/61/i=19/a=R271?key=crossref.7030e3a21b4056d207fcc7adccfcd532. [Cited on page 57.]

D. R. Dance and I. Sechopoulos. Dosimetry in x-ray-based breast imaging. *Physics in Medicine & Biology*, 61(19):R271, 2016b. [Cited on page 47.]

D. R. Dance, R. Hunt, P. Bakic, A. Maidment, M. Sandborg, G. Ullman, and G. Alm Carlsson. Breast dosimetry using high-resolution voxel phantoms. *Radiation protection dosimetry*, 114(1-3):359–363, 2005a. [Cited on pages 45 and 48.]

D. R. Dance, R. A. Hunt, P. R. Bakic, A. D. A. Maidment, M. Sandborg, G. Ullman, and G. Alm Carlsson. Breast dosimetry using high-resolution voxel phantoms. *Radiation Protection Dosimetry*, 114(1-3):359–363, 2005b. ISSN 0144-8420. doi: 10.1093/rpd/nch510. URL https://doi.org/10.1093/rpd/nch510. [Cited on page 48.]

S. de Bournonville, S. Vangrunderbeeck, and G. Kerckhofs. Contrast-enhanced microct for virtual 3d anatomical pathology of biological tissues: a literature review. *Contrast media & molecular imaging*, 2019, 2019. [Cited on page 112.]

J. E. de Groot, M. J. Broeders, C. A. Grimbergen, and G. J. den Heeten. Pain-preventing strategies in mammography: an observational study of simultaneously recorded pain and

breast mechanics throughout the entire breast compression cycle. *BMC women's health*, 15 (1):1–9, 2015. [Cited on page 19.]

H. De Leeuw, B. L. Stehouwer, C. J. Bakker, D. W. Klomp, P. J. van Diest, P. R. Luijten, P. R. Seevinck, M. A. van den Bosch, M. A. Viergever, and W. B. Veldhuis. Detecting breast microcalcifications with high-field mri. *NMR in Biomedicine*, 27(5):539–546, 2014. [Cited on page 29.]

H. Delis, K. Christaki, B. Healy, G. Loreti, G. Poli, P. Toroi, and A. Meghzifene. Moving beyond quality control in diagnostic radiology and the role of the clinically qualified medical physicist. *Physica Medica*, 41:104–108, 2017. [Cited on page 16.]

P. Delogu, P. Oliva, R. Bellazzini, A. Brez, P. De Ruvo, M. Minuti, M. Pinchera, G. Spandre, and A. Vincenzi. Characterization of pixirad-1 photon counting detector for X-ray imaging. *Journal of Instrumentation*, 11(01):P01015, 2016. doi: 10.1088/1748-0221/11/01/P01015. [Cited on page 63.]

P. Delogu, L. Brombal, V. Di Trapani, S. Donato, U. Bottigli, D. Dreossi, B. Golosio, P. Oliva, L. Rigon, and R. Longo. Optimization of the equalization procedure for a single-photon counting cdte detector used for ct. *Journal of Instrumentation*, 12(11):C11014, 2017a. doi: 10.1088/1748-0221/12/11/C11014. [Cited on pages 63 and 70.]

P. Delogu, B. Golosio, C. Fedon, F. Arfelli, R. Bellazzini, A. Brez, F. Brun, F. Di Lillo, D. Dreossi, G. Mettivier, et al. Imaging study of a phase-sensitive breast-CT system in continuous acquisition mode. *Journal of Instrumentation*, 12(01):C01016, 2017b. doi: 10.1088/1748-0221/12/01/C01016. [Cited on pages 59 and 61.]

P. Delogu, V. Di Trapani, L. Brombal, G. Mettivier, A. Taibi, and P. Oliva. Optimization of the energy for breast monochromatic absorption X-ray computed tomography. *Scientific reports*, 9(1):1–10, 2019. doi: 10.1038/s41598-019-49351-2. [Cited on page 77.]

C. DeSantis, J. Ma, L. Bryan, and A. Jemal. Breast cancer statistics, 2013. *CA: a cancer journal for clinicians*, 64(1):52–62, 2014. [Cited on page 22.]

V. Di Trapani, A. Bravin, F. Brun, D. Dreossi, R. Longo, A. Mittone, L. Rigon, and P. Delogu. Characterization of the acquisition modes implemented in pixirad-1/pixie-iii x-ray detector:

Effects of charge sharing correction on spectral resolution and image quality. *Nuclear Instruments and Methods in Physics Research Section A: Accelerators, Spectrometers, Detectors and Associated Equipment*, 955:163220, 2020. [Cited on page 63.]

M. Dimmock, J. McKinley, A. Massey, D. Hausermann, N. Tam, E. Stewart, C. Cowling, J. Sim, P. C. Brennan, T. Gureyev, et al. Designing a breast support device for phase contrast tomographic imaging: getting ready for a clinical trial. *The British Journal of Radiology*, 95:20211243, 2022. [Cited on page 87.]

S. Donato, L. Brombal, F. Arfelli, V. Fanti, R. Longo, P. Oliva, L. Rigon, and B. Golosio. Optimization of a customized simultaneous algebraic reconstruction technique algorithm for breast ct. In *2019 IEEE Nuclear Science Symposium and Medical Imaging Conference (NSS/MIC)*, pages 1–2. IEEE, 2019a. [Cited on pages 98, 100, and 101.]

S. Donato, L. Brombal, G. Tromba, R. Longo, et al. Phase-contrast breast-CT: Optimization of experimental parameters and reconstruction algorithms. In *World Congress on Medical Physics and Biomedical Engineering 2018*, pages 109–115. Springer, 2019b. doi: 10.1007/978-981-10-9035-6_20. [Cited on pages 68, 69, and 98.]

S. Donato, L. Arana Peña, D. Bonazza, V. Formoso, R. Longo, G. Tromba, and L. Brombal. Optimization of pixel size and propagation distance in X-ray phase-contrast virtual histology. *Journal of Instrumentation*, 17(05):C05021, May 2022a. ISSN 1748-0221. doi: 10.1088/1748-0221/17/05/C05021. URL https://iopscience.iop.org/article/10.1088/1748-0221/17/05/C05021. [Cited on pages 112, 113, 116, 117, 128, and 134.]

S. Donato, L. Brombal, L. Arana Peña, F. Arfelli, A. Contillo, P. Delogu, F. Di Lillo, V. Di Trapani, V. Fanti, R. Longo, et al. Optimization of a customized simultaneous algebraic reconstruction technique algorithm for phase-contrast breast computed tomography. *Physics in Medicine & Biology*, 67(9):095012, 2022b. [Cited on page 98.]

J. S. Drukteinis, B. P. Mooney, C. I. Flowers, and R. A. Gatenby. Beyond mammography: new frontiers in breast cancer screening. *The American journal of medicine*, 126(6):472–479, 2013. [Cited on page 29.]

C. Dullin, F. di Lillo, A. Svetlove, J. Albers, W. Wagner, A. Markus, N. Sodini, D. Dreossi, F. Alves, and G. Tromba. Multiscale biomedical imaging at the syrmep beamline of elettra-

closing the gap between preclinical research and patient applications. *Physics Open*, 6: 100050, 2021. [Cited on pages 37, 42, and 114.]

M. Dustler, I. Andersson, H. Brorson, P. Fröjd, S. Mattsson, A. Tingberg, S. Zackrisson, and D. Förnvik. Breast compression in mammography: pressure distribution patterns. *Acta Radiologica*, 53(9):973–980, 2012. [Cited on page 23.]

M. Endrizzi. X-ray phase-contrast imaging. *Nuclear instruments and methods in physics research section A: Accelerators, spectrometers, detectors and associated equipment*, 878: 88–98, 2018. [Cited on pages 34 and 67.]

L. Enriquez and J. Listinsky. Role of mri in breast cancer management. *Cleveland Clinic journal of medicine*, 76(9):525–532, 2009. [Cited on page 29.]

I. FabLab. Ictp scientific fabrication laboratories, 2023. URL http://scifablab.ictp.it/about/. [Cited on page 80.]

L. Faillace, R. Agostino, A. Bacci, R. Barberi, A. Bosotti, F. Broggi, P. Cardarelli, S. Cialdi, I. Drebot, V. Formoso, et al. Status of compact inverse compton sources in italy: Brixs and star. In *Advances in Laboratory-Based X-ray Sources, Optics, and Applications VII*, volume 11110, pages 14–21. SPIE, 2019. doi: 10.1117/12.2531168. [Cited on page 138.]

C. Fedon, F. Longo, G. Mettivier, and R. Longo. Geant4 for breast dosimetry: parameters optimization study. *Physics in Medicine & Biology*, 60(16):N311, 2015. doi: 10.1088/0031-9155/60/16/N311. [Cited on pages 60 and 75.]

C. Fedon, M. Caballo, and I. Sechopoulos. Internal breast dosimetry in mammography: Monte carlo validation in homogeneous and anthropomorphic breast phantoms with a clinical mammography system. *Medical Physics*, 45(8):3950–3961, 2018a. doi: 10.1002/mp.13069. URL https://aapm.onlinelibrary.wiley.com/doi/abs/10.1002/mp.13069. [Cited on page 40.]

C. Fedon, M. Caballo, and I. Sechopoulos. Internal breast dosimetry in mammography: Monte carlo validation in homogeneous and anthropomorphic breast phantoms with a clinical mammography system. *Medical physics*, 45(8):3950–3961, 2018b. [Cited on page 48.]

C. Fedon, C. Rabin, M. Caballo, O. Diaz, E. García, A. Rodríguez-Ruiz, G. A. González-Sprinberg, and I. Sechopoulos. Monte carlo study on optimal breast voxel resolution for

dosimetry estimates in digital breast tomosynthesis. *Physics in Medicine & Biology*, 64(1): 015003, 2018c. [Cited on page 52.]

C. Fedon, C. Rabin, M. Caballo, O. Diaz, E. Garcia, A. Rodriguez, G. Gonzalez, and I. Sechopoulos. Monte Carlo study on optimal breast voxel resolution for dosimetry in digital breast tomosynthesis. *Phys. Med. Biol.*, 64:12, 2019. [Cited on pages 49, 50, and 54.]

C. Fedon, M. Caballo, E. García, O. Diaz, J. M. Boone, D. R. Dance, and I. Sechopoulos. Fibroglandular tissue distribution in the breast during mammography and tomosynthesis based on breast ct data: A patient-based characterization of the breast parenchyma. *Medical physics*, 48(3):1436–1447, 2021. [Cited on page 48.]

M. A. Flower. *Webb's physics of medical imaging*. CRC press, 2012. [Cited on page 20.]

D. Förnvik, I. Andersson, T. Svahn, P. Timberg, S. Zackrisson, and A. Tingberg. The effect of reduced breast compression in breast tomosynthesis: human observer study using clinical cases. *Radiation protection dosimetry*, 139(1-3):118–123, 2010. [Cited on page 24.]

J. Frohn, D. Pinkert-Leetsch, J. Missbach-Güntner, M. Reichardt, M. Osterhoff, F. Alves, and T. Salditt. 3d virtual histology of human pancreatic tissue by multiscale phase-contrast x-ray tomography. *Journal of Synchrotron Radiation*, 27(6):1707–1719, 2020. doi: 10.1107/S1600577520011327. [Cited on page 109.]

F. Galati, G. Moffa, and F. Pediconi. Breast imaging: Beyond the detection. *European Journal of Radiology*, 146:110051, 2022. [Cited on page 29.]

E. García, C. Fedon, M. Caballo, R. Martí, I. Sechopoulos, and O. Diaz. Realistic compressed breast phantoms for medical physics applications. In *15th International Workshop on Breast Imaging (IWBI2020)*, volume 11513, pages 30–37. SPIE, 2020. [Cited on page 51.]

F. T. Gassert, T. Urban, M. Frank, K. Willer, W. Noichl, P. Buchberger, R. Schick, T. Koehler, J. von Berg, A. A. Fingerle, et al. X-ray dark-field chest imaging: qualitative and quantitative results in healthy humans. *Radiology*, 301(2):389–395, 2021. doi: 10.1148/radiol.2021210963. [Cited on page 138.]

A. Gervaise, B. Osemont, S. Lecocq, A. Noel, E. Micard, J. Felblinger, and A. Blum. Ct image quality improvement using adaptive iterative dose reduction with wide-volume acquisition on 320-detector ct. *European radiology*, 22(2):295–301, 2012. [Cited on page 98.]

M. U. Ghani, L. L. Fajardo, F. Omoumi, A. Yan, P. Jenkins, M. Wong, Y. Li, M. E. Peterson, E. J. Callahan, S. L. Hillis, et al. A phase sensitive x-ray breast tomosynthesis system: Preliminary patient images with cancer lesions. *Physics in Medicine & Biology*, 66(21): 21LT01, 2021. doi: 10.1088/1361-6560/ac2ea6. [Cited on page 138.]

N. Giannotti, S. T. Taba, T. Gureyev, S. Lewis, L. Brombal, R. Longo, S. Donato, G. Tromba, L. A. Pena, D. Hausermann, C. Hall, A. Maksimenko, B. Arhatari, Y. Nesterets, and P. Brennan. Propagation-based phase-contrast breast computed tomography: a visual grading assessment of the performance of photon-counting and flat-panel x-ray detectors, 2022. URL https://www.medrxiv.org/content/early/2022/11/01/2022.11.01.22281633. [Cited on page 104.]

F. J. Gilbert and K. Pinker-Domenig. Diagnosis and staging of breast cancer: when and how to use mammography, tomosynthesis, ultrasound, contrast-enhanced mammography, and magnetic resonance imaging. *Diseases of the Chest, Breast, Heart and Vessels 2019-2022*, pages 155–166, 2019. [Cited on pages 24 and 30.]

F. J. Gilbert, L. Tucker, and K. C. Young. Digital breast tomosynthesis (dbt): a review of the evidence for use as a screening tool. *Clinical radiology*, 71(2):141–150, 2016. [Cited on page 24.]

B. Golosio, A. Brunetti, and R. Cesareo. Algorithmic techniques for quantitative compton tomography. *Nuclear Instruments and Methods in Physics Research Section B: Beam Interactions with Materials and Atoms*, 213:108–111, 2004. doi: 10.1016/S0168-583X(03)01542-8. [Cited on pages 98 and 99.]

H. I. Greenwood, K. Dodelzon, and J. T. Katzen. Impact of advancing technology on diagnosis and treatment of breast cancer. *Surgical Clinics*, 98(4):703–724, 2018. [Cited on page 30.]

J. Greffier, F. Macri, A. Larbi, A. Fernandez, E. Khasanova, F. Pereira, C. Mekkaoui, and J. Beregi. Dose reduction with iterative reconstruction: optimization of ct protocols in clinical practice. *Diagnostic and interventional imaging*, 96(5):477–486, 2015. [Cited on page 98.]

A. Grubstein, Y. Rapson, S. Morgenstern, I. Gadiel, A. Haboosheh, R. Yerushalmi, and M. Cohen. Clinical information invasive lobular carcinoma of the breast: Appearance on digital

breast tomosynthesis. 2016. doi: 10.1159/000450868. URL www.karger.com/brc. [Cited on pages 24 and 119.]

T. Gureyev, Y. I. Nesterets, P. Baran, S. Taba, S. Mayo, D. Thompson, B. Arhatari, A. Mihocic, B. Abbey, D. Lockie, J. Fox, B. Kumar, Z. Prodanovic, D. Hausermann, A. Maksimenko, C. Hall, A. Peele, M. Dimmock, K. Pavlov, M. Cholewa, S. Lewis, G. Tromba, H. Quiney, and P. Brennan. Propagation-based X-ray phase-contrast tomography of mastectomy samples using synchrotron radiation. *Medical physics*, 46(12):5478–5487, 2019. [Cited on page 60.]

T. E. Gureyev, Y. I. Nesterets, A. Kozlov, D. M. Paganin, and H. M. Quiney. On the "unreasonable" effectiveness of transport of intensity imaging and optical deconvolution. *JOSA A*, 34 (12):2251–2260, 2017. doi: 10.1364/JOSAA.34.002251. [Cited on pages 65, 68, and 105.]

R. Hammerstein, D. W. Miller, D. R. White, M. Ellen Masterson, H. Q. Woodard, and J. S. Laughlin. Absorbed radiation dose in mammography. *Radiology*, 130(2):485–491, 1979. doi: 10.1148/130.2.485. URL https://doi.org/10.1148/130.2.485. PMID: 760167. [Cited on pages 46, 50, 54, and 75.]

S. E. Harms. Mri in breast cancer diagnosis and treatment. *Current problems in diagnostic radiology*, 25(6):192–215, 1996. [Cited on page 29.]

M. A. Helvie, C. Paramagul, H. A. Oberman, and D. D.Adler. Invasive lobular carcinoma. imaging features and clinical detection. *Invest Radiol*, 28:202–7, 1993. ISSN 2366-1070. doi: 10.1097/00004424-199303000-00002. [Cited on pages 29 and 119.]

A. M. Hernandez and J. M. Boone. Tungsten anode spectral model using interpolating cubic splines: Unfiltered x-ray spectra from 20 kv to 640 kv. *Medical Physics*, 41(4):042101, 2014. doi: 10.1118/1.4866216. URL https://aapm.onlinelibrary.wiley.com/doi/abs/10.1118/1.4866216. [Cited on page 54.]

A. M. Hernandez and J. M. Boone. Average glandular dose coefficients for pendant-geometry breast ct using realistic breast phantoms. *Medical physics*, 44(10):5096–5105, 2017. [Cited on pages 80 and 81.]

A. M. Hernandez, J. A. Seibert, and J. M. Boone. Breast dose in mammography is about 30% lower when realistic heterogeneous glandular distributions are considered. *Medical Physics*,

42(11):6337–6348, 2015. doi: 10.1118/1.4931966. URL https://aapm.onlinelibrary.wiley.com/doi/abs/10.1118/1.4931966. [Cited on pages 48 and 57.]

A. M. Hernandez, A. E. Becker, and J. M. Boone. Updated breast ct dose coefficients (dg nct) using patient-derived breast shapes and heterogeneous fibroglandular distributions. *Medical Physics*, 46(3):1455–1466, 2019. [Cited on page 48.]

K. Holland, I. Sechopoulos, R. M. Mann, G. J. Den Heeten, C. H. van Gils, and N. Karssemeijer. Influence of breast compression pressure on the performance of population-based mammography screening. *Breast cancer research*, 19(1):1–8, 2017. [Cited on page 23.]

B. Hornberger, J. Kasahara, M. Gifford, R. Ruth, and R. Loewen. A compact light source providing high-flux, quasi-monochromatic, tunable x-rays in the laboratory. In *Advances in Laboratory-based X-Ray Sources, Optics, and Applications VII*, volume 11110, page 1111003. SPIE, 2019. doi: 10.1117/12.2527356. [Cited on page 138.]

S. Y. Huang, J. Boone, K. Yang, N. Packard, S. McKenney, N. Prionas, K. Lindfors, and M. Yaffe. The characterization of breast anatomical metrics using breast ct. *Medical Physics*, 38:2180–2191, 2011. [Cited on page 48.]

International Atomic Energy Agency. *Diagnostic Radiology Physics*. Non-serial Publications. INTERNATIONAL ATOMIC ENERGY AGENCY, Vienna, 2014. ISBN 978-92-0-131010-1. URL https://www.iaea.org/publications/8841/diagnostic-radiology-physics. [Cited on pages 16, 20, 23, and 26.]

International Atomic Energy Agency. *Radiation Protection and Safety in Medical Uses of Ionizing Radiation. Specific Safety Guides, SSG-46.* International Atomic Energy Agency, Vienna, Austria, 2018. URL https://www.iaea.org/publications/11102/radiation-protection-and-safety-in-medical-uses-of-ionizing-radiation. [Cited on page 15.]

S. Iranmakani, T. Mortezazadeh, F. Sajadian, M. F. Ghaziani, A. Ghafari, D. Khezerloo, and A. E. Musa. A review of various modalities in breast imaging: technical aspects and clinical outcomes. *Egyptian Journal of Radiology and Nuclear Medicine*, 51(1):1–22, 2020. [Cited on page 29.]

P. C. Johns and M. J. Yaffe. X-ray characterisation of normal and neoplastic breast tissues. *Physics in Medicine & Biology*, 32(6):675, 1987. [Cited on page 22.]

S. F. Johnsen, Z. A. Taylor, M. J. Clarkson, J. Hipwell, M. Modat, B. Eiben, L. Han, Y. Hu, T. Mertzanidou, D. J. Hawkes, and et al. Niftysim: A gpu-based nonlinear finite element package for simulation of soft tissue biomechanics. *International journal of computer assisted radiology and surgery*, 10(7):1077–1095, 2015. [Cited on page 50.]

A. C. Kak, M. Slaney, and G. Wang. Principles of computerized tomographic imaging. *Medical Physics*, 29(1):107–107, 2002. doi: 10.1118/1.1455742. [Cited on page 98.]

W. A. Kalender, M. Beister, J. M. Boone, D. Kolditz, S. V. Vollmar, and M. C. Weigel. High-resolution spiral CT of the breast at very low dose: concept and feasibility considerations. *European radiology*, 22(1):1–8, 2012. doi: 10.1007/s00330-011-2169-4. [Cited on pages 25 and 30.]

W. A. Kalender, D. Kolditz, C. Steiding, V. Ruth, F. Lück, A.-C. Rößler, and E. Wenkel. Technical feasibility proof for high-resolution low-dose photon-counting CT of the breast. *European radiology*, 27(3):1081–1086, 2017. doi: 10.1007/s00330-016-4459-3. [Cited on page 26.]

A. Karellas and S. Vedantham. Breast cancer imaging: a perspective for the next decade. *Medical physics*, 35(11):4878–4897, 2008. [Cited on page 29.]

O. L. Katsamenis, M. Olding, J. A. Warner, D. S. Chatelet, M. G. Jones, G. Sgalla, B. Smit, O. J. Larkin, I. Haig, L. Richeldi, I. Sinclair, P. M. Lackie, and P. Schneider. X-ray Micro-Computed Tomography for Nondestructive Three-Dimensional (3D) X-ray Histology. *The American Journal of Pathology*, 189(8):1608–1620, Aug. 2019. ISSN 00029440. doi: 10.1016/j.ajpath.2019.05.004. URL https://linkinghub.elsevier.com/retrieve/pii/S0002944019302068. [Cited on page 112.]

F. Khan, F. Enzmann, and M. Kersten. Beam-hardening correction by a surface fitting and phase classification by a least square support vector machine approach for tomography images of geological samples. *Solid Earth Discussions*, 7(4), 2015. [Cited on pages 115 and 119.]

M. A. Kimm, M. Willner, E. Drecoll, J. Herzen, P. B. Noël, E. J. Rummeny, F. Pfeiffer, and A. A. Fingerle. Grating-based phase-contrast ct (pcct): histopathological correlation of human liver cirrhosis and hepatocellular carcinoma specimen. *Journal of Clinical Pathology*, 73(8):483–487, 2020. doi: 10.1136/jclinpath-2019-206380. [Cited on page 138.]

M. J. Kitchen, R. Lewis, N. Yagi, K. Uesugi, D. Paganin, S. B. Hooper, G. Adams, S. Jureczek, J. Singh, C. Christensen, et al. Phase contrast x-ray imaging of mice and rabbit lungs: a comparative study. *The British journal of radiology*, 78(935):1018–1027, 2005. [Cited on page 41.]

M. J. Kitchen, G. A. Buckley, T. E. Gureyev, M. J. Wallace, N. Andres-Thio, K. Uesugi, N. Yagi, and S. B. Hooper. CT dose reduction factors in the thousands using X-ray phase contrast. *Scientific reports*, 7(1):15953, 2017. doi: 10.1038/s41598-017-16264-x. [Cited on page 41.]

G. F. Knoll. *Radiation detection and measurement*. John Wiley & Sons, 2010. doi: 10.1016/S0969-806X(00)00323-6. [Cited on page 63.]

T. M. Kolb, J. Lichy, and J. H. Newhouse. Comparison of the performance of screening mammography, physical examination, and breast us and evaluation of factors that influence them: an analysis of 27,825 patient evaluations. *Radiology*, 225(1):165–175, 2002. [Cited on page 30.]

C. Koning. Koning breast CT, 2022. URL https://www.koninghealth.com/product-solutions/koning-breast-ct. [Cited on pages 26 and 79.]

G. Kowalski. Suppression of ring artefacts in ct fan-beam scanners. *ieee Transactions on nuclear science*, 25(5):1111–1116, 1978. [Cited on page 70.]

Y. Kyriakou, D. Prell, and W. A. Kalender. Ring artifact correction for high-resolution micro ct. *Physics in medicine & biology*, 54(17):N385, 2009. [Cited on page 71.]

B. Lakin, D. Grasso, S. Shah, R. Stewart, P. Bansal, J. Freedman, M. Grinstaff, and B. Snyder. Cationic agent contrast-enhanced computed tomography imaging of cartilage correlates with the compressive modulus and coefficient of friction. *Osteoarthritis and cartilage*, 21(1):60–68, 2013. [Cited on page 111.]

D. L. Lam, N. Houssami, and J. M. Lee. Imaging surveillance after primary breast cancer treatment. *AJR. American journal of roentgenology*, 208(3):676, 2017. [Cited on page 24.]

K. Lång, I. Andersson, A. Rosso, A. Tingberg, P. Timberg, and S. Zackrisson. Performance of one-view breast tomosynthesis as a stand-alone breast cancer screening modality: results

from the malmö breast tomosynthesis screening trial, a population-based study. *European radiology*, 26(1):184–190, 2016. doi: 10.1007/s00330-015-3803-3. [Cited on page 24.]

C. H. Lee, D. D. Dershaw, D. Kopans, P. Evans, B. Monsees, D. Monticciolo, R. J. Brenner, L. Bassett, W. Berg, S. Feig, et al. Breast cancer screening with imaging: recommendations from the society of breast imaging and the acr on the use of mammography, breast mri, breast ultrasound, and other technologies for the detection of clinically occult breast cancer. *Journal of the American college of radiology*, 7(1):18–27, 2010. [Cited on page 27.]

R. Lewis. Medical phase contrast X-ray imaging: current status and future prospects. *Physics in medicine & biology*, 49(16):3573, 2004. doi: 10.1088/0031-9155/49/16/005. [Cited on page 34.]

R. A. Lewis, N. Yagi, M. J. Kitchen, M. J. Morgan, D. Paganin, K. K. W. Siu, K. Pavlov, I. Williams, K. Uesugi, M. J. Wallace, et al. Dynamic imaging of the lungs using x-ray phase contrast. *Physics in Medicine & Biology*, 50(21):5031, 2005. [Cited on page 41.]

S. J. Lewis, N. Tam, L. M. Arana Pena, I. Juria, S. T. Taba, D. Hausermann, P. C. Brennan, C. Hall, B. Arhatari, G. Tromba, et al. Getting a-breast of immobilisation needs for the implementation of phase contrast tomography. In *15th International Workshop on Breast Imaging (IWBI2020)*, volume 11513, pages 443–449. SPIE, 2020. [Cited on pages 86, 87, and 88.]

K. K. Lindfors, J. M. Boone, T. R. Nelson, K. Yang, A. L. Kwan, and D. F. Miller. Dedicated breast ct: initial clinical experience. *Radiology*, 246(3):725–733, 2008. doi: 10.1148/radiol.2463070410. [Cited on pages 25 and 30.]

K. K. Lindfors, J. M. Boone, M. S. Newell, and C. J. D'Orsi. Dedicated breast computed tomography: the optimal cross-sectional imaging solution? *Radiologic Clinics*, 48(5):1043–1054, 2010. doi: 10.1016/j.rcl.2010.06.001. [Cited on page 25.]

R. Longo, A. Abrami, F. Arfelli, P. Bregant, V. Chenda, M. A. Cova, D. Dreossi, F. De Guarrini, R. Menk, E. Quai, et al. Phase contrast mammography with synchrotron radiation: physical aspects of the clinical trial. In *Medical Imaging 2007: Physics of Medical Imaging*, volume 6510, page 65100T. International Society for Optics and Photonics, 2007. doi: 10.1117/12.708403. [Cited on pages 38 and 75.]

R. Longo, M. Tonutti, L. Rigon, F. Arfelli, D. Dreossi, E. Quai, F. Zanconati, E. Castelli, G. Tromba, and M. A. Cova. Clinical study in phase-contrast mammography: image-quality analysis. *Philosophical Transactions of the Royal Society A: Mathematical, physical and engineering sciences*, 372(2010):20130025, 2014. doi: 10.1098/rsta.2013.0025. [Cited on pages 39 and 40.]

R. Longo, F. Arfelli, R. Bellazzini, U. Bottigli, A. Brez, F. Brun, A. Brunetti, P. Delogu, F. Di Lillo, D. Dreossi, et al. Towards breast tomography with synchrotron radiation at elettra: first images. *Physics in Medicine & Biology*, 61(4):1634, 2016. [Cited on pages 26, 59, 63, and 77.]

R. Longo, F. Arfelli, D. Bonazza, U. Bottigli, L. Brombal, A. Contillo, M. Cova, P. Delogu, F. Di Lillo, V. Di Trapani, et al. Advancements towards the implementation of clinical phase-contrast breast computed tomography at elettra. *Journal of Synchrotron Radiation*, 26 (4), 2019. doi: 10.1107/S1600577519005502. [Cited on pages 59, 60, 69, 77, and 133.]

R. Longo, F. Arfelli, S. Donato, D. Bonazza, L. Brombal, A. Contillo, M. A. Cova, P. De-logu, V. Di Trapani, B. Golosio, G. Mettivier, P. Oliva, L. Rigon, A. Taibi, M. Tonutti, G. Tromba, and F. Zanconati. Lesion visibility in phase-contrast breast CT: comparison with histological images. In C. Van Ongeval, N. Marshall, and H. Bosmans, editors, *15th International Workshop on Breast Imaging (IWBI2020)*, page 68, Leuven, Belgium, May 2020. SPIE. ISBN 978-1-5106-3831-0 978-1-5106-3832-7. doi: 10.1117/12.2564202. URL https://www.spiedigitallibrary.org/conference-proceedings-of-spie/11513/2564202/Lesion-visibility-in-phase-contrast-breast-CT--comparison-with/10.1117/12.2564202.full. [Cited on page 112.]

J. K. Lopez and L. W. Bassett. Invasive Lobular Carcinoma of the Breast: Spectrum of Mam-mographic, US, and MR Imaging Findings. *RadioGraphics*, 29(1):165–176, Jan. 2009. ISSN 0271-5333, 1527-1323. doi: 10.1148/rg.291085100. URL http://pubs.rsna.org/doi/10.1148/rg.291085100. [Cited on pages 29 and 119.]

A. Löve, M. Olsson, R. Siemund, F. Stålhammar, I. Björkman-Burtscher, and M. Söderberg. Six iterative reconstruction algorithms in brain ct: a phantom study on image quality at different radiation dose levels. *The British journal of radiology*, 86(1031):20130388, 2013. [Cited on page 98.]

J. Luveta, R. M. Parks, D. M. Heery, K.-L. Cheung, and S. J. Johnston. Invasive lobular breast cancer as a distinct disease: Implications for therapeutic strategy. *Oncology and Therapy*, 8: 1–11, 6 2020. ISSN 2366-1070. doi: 10.1007/S40487-019-00105-0. [Cited on page 118.]

R. M. Mann, N. Cho, and L. Moy. Breast mri: state of the art. *Radiology*, 292(3):520–536, 2019. [Cited on page 29.]

J. Mansell, E. Weiler-Mithoff, S. Stallard, J. Doughty, E. Mallon, and L. Romics. Oncoplastic breast conservation surgery is oncologically safe when compared to wide local excision and mastectomy. *The Breast*, 32:179–185, 2017. [Cited on pages 18 and 110.]

G. Margaritondo. Introduction to synchrotron radiation, 1988. [Cited on page 35.]

L. Massimi, T. Suaris, C. K. Hagen, M. Endrizzi, P. R. Munro, G. Havariyoun, P. Hawker, B. Smit, A. Astolfo, O. J. Larkin, et al. Detection of involved margins in breast specimens with x-ray phase-contrast computed tomography. *Scientific reports*, 11(1):1–9, 2021. doi: 10.1038/s41598-021-83330-w. [Cited on page 138.]

L. Massimi, T. Suaris, C. K. Hagen, M. Endrizzi, P. R. T. Munro, G. Havariyoun, P. M. S. Hawker, B. Smit, A. Astolfo, O. J. Larkin, R. M. Waltham, Z. Shah, S. W. Duffy, R. L. Nelan, A. Peel, J. L. Jones, I. G. Haig, D. Bate, and A. Olivo. Volumetric High-Resolution X-Ray Phase-Contrast Virtual Histology of Breast Specimens With a Compact Laboratory System. *IEEE Transactions on Medical Imaging*, 41(5):1188–1195, May 2022. ISSN 0278-0062, 1558-254X. doi: 10.1109/TMI.2021.3137964. URL https://ieeexplore.ieee.org/document/9661394/. [Cited on pages 112 and 138.]

E. S. McDonald, A. Oustimov, S. P. Weinstein, M. B. Synnestvedt, M. Schnall, and E. F. Conant. Effectiveness of digital breast tomosynthesis compared with digital mammography: outcomes analysis from 3 years of breast cancer screening. *JAMA oncology*, 2(6):737–743, 2016. doi: 10.1001/jamaoncol.2015.5536. [Cited on page 24.]

G. Mettivier, C. Fedon, F. Di Lillo, R. Longo, A. Sarno, G. Tromba, and P. Russo. Glandular dose in breast computed tomography with synchrotron radiation. *Physics in Medicine & Biology*, 61(2):569, 2015. doi: 10.1088/0031-9155/61/2/569. [Cited on page 75.]

I. Millet, E. Pages, D. Hoa, S. Merigeaud, F. Curros Doyon, X. Prat, and P. Taourel. Pearls and pitfalls in breast mri. *The British journal of radiology*, 85(1011):197–207, 2012. [Cited on page 28.]

S. Mills. *Histology for Pathologists*. Lippincott Williams and Wilkins, USA, fourth edition edition, 2012. [Cited on page 16.]

A. Mittone, L. Fardin, F. Di Lillo, M. Fratini, H. Requardt, A. Mauro, R. A. Homs-Regojo, P.-A. Douissard, G. E. Barbone, J. Stroebel, et al. Multiscale pink-beam microct imaging at the esrf-id17 biomedical beamline. *Journal of Synchrotron Radiation*, 27(5):1347–1357, 2020. doi: 10.1107/S160057752000911X. [Cited on page 109.]

K. Mori, N. Sekine, H. Sato, D. Shimao, H. Shiwaku, K. Hyodo, H. Sugiyama, M. Ando, K. Ohashi, M. Koyama, et al. Application of synchrotron x-ray imaging to phase objects in orthopedics. *Journal of Synchrotron Radiation*, 9(3):143–147, 2002. [Cited on page 41.]

T. Morita, M. Yamada, A. Kano, S. Nagatsuka, C. Honda, and T. Endo. A comparison between film-screen mammography and full-field digital mammography utilizing phase contrast technology in breast cancer screening programs. In *International Workshop on Digital Mammography*, pages 48–54. Springer, 2008. doi: 10.1007/978-3-540-70538-3_7. [Cited on page 38.]

A. Mozzanica, A. Bergamaschi, M. Brueckner, S. Cartier, R. Dinapoli, D. Greiffenberg, J. Jungmann-Smith, D. Maliakal, D. Mezza, M. Ramilli, et al. Characterization results of the JUNGFRAU full scale readout ASIC. *Journal of Instrumentation*, 11(02):C02047, 2016. doi: 10.1088/1748-0221/11/01/P01007. [Cited on page 61.]

National Research Council. *Health risks from exposure to low levels of ionizing radiation: BEIR VII phase 2*. National Academies Press, 2006. [Cited on pages 22 and 46.]

Y. I. Nesterets and T. E. Gureyev. Noise propagation in X-ray phase-contrast imaging and computed tomography. *Journal of Physics D: Applied Physics*, 47(10):105402, 2014. doi: 10.1088/0022-3727/47/10/105402. [Cited on pages 68 and 113.]

Y. I. Nesterets, T. E. Gureyev, and M. R. Dimmock. Optimisation of a propagation-based X-ray phase-contrast micro-CT system. *Journal of Physics D: Applied Physics*, 51(11):115402, 2018. doi: 10.1088/1361-6560/aa5d3d. [Cited on page 113.]

R. Ning, D. Conover, Y. Yu, Y. Zhang, W. Cai, R. Betancourt-Benitez, and X. Lu. A novel cone beam breast CT scanner: System evaluation. In *Medical imaging 2007: physics of medical imaging*, volume 6510, page 651030. International Society for Optics and Photonics, 2007. doi: 10.1117/12.710340. [Cited on page 27.]

Y. Nishiyama, K. Tada, Y. Nishiyama, H. Mori, M. Maruyama, T. Katsube, N. Yamamoto, H. Kanayama, Y. Yamamoto, and H. Kitagaki. Effect of the forward-projected model-based iterative reconstruction solution algorithm on image quality and radiation dose in pediatric cardiac computed tomography. *Pediatric radiology*, 46(12):1663–1670, 2016. [Cited on page 98.]

A. O'Connell, D. L. Conover, Y. Zhang, P. Seifert, W. Logan-Young, C.-F. L. Lin, L. Sahler, and R. Ning. Cone-beam CT for breast imaging: Radiation dose, breast coverage, and image quality. *American Journal of Roentgenology*, 195(2):496–509, 2010. doi: 10.2214/AJR.08.1017. [Cited on pages 25, 27, 30, and 104.]

A. M. O'Connell, A. Karellas, and S. Vedantham. The potential role of dedicated 3d breast CT as a diagnostic tool: review and early clinical examples. *The breast journal*, 20(6):592–605, 2014. doi: 10.1111/tbj.12327. [Cited on pages 26 and 30.]

K. C. Oeffinger, E. T. H. Fontham, R. Etzioni, A. Herzig, J. S. Michaelson, Y.-C. T. Shih, L. C. Walter, T. R. Church, C. R. Flowers, S. J. LaMonte, A. M. D. Wolf, C. DeSantis, J. Lortet-Tieulent, K. Andrews, D. Manassaram-Baptiste, D. Saslow, R. A. Smith, O. W. Brawley, and R. Wender. Breast Cancer Screening for Women at Average Risk: 2015 Guideline Update From the American Cancer Society. *JAMA*, 314(15):1599–1614, 10 2015. ISSN 0098-7484. doi: 10.1001/jama.2015.12783. URL https://doi.org/10.1001/jama.2015.12783. [Cited on page 15.]

P. Oliva, B. Golosio, F. Arfelli, P. Delogu, F. Di Lillo, D. Dreossi, V. Fanti, L. Fardin, C. Fedon, G. Mettivier, et al. Quantitative evaluation of breast CT reconstruction by means of figures of merit based on similarity metrics. In *2017 IEEE Nuclear Science Symposium and Medical Imaging Conference (NSS/MIC)*, pages 1–5. IEEE, 2017. doi: 10.1109/NSS-MIC.2017.8532786. [Cited on pages 98 and 99.]

P. Oliva, V. Di Trapani, F. Arfelli, L. Brombal, S. Donato, B. Golosio, R. Longo, G. Mettivier, L. Rigon, A. Taibi, et al. Experimental optimization of the energy for breast-ct with synchrotron radiation. *Scientific reports*, 10(1):1–13, 2020. [Cited on pages 77 and 133.]

A. Olivo and E. Castelli. X-ray phase contrast imaging: From synchrotrons to conventional sources. *Rivista del nuovo cimento*, 37(9):467–508, 2014. doi: 10.1393/ncr/i2014-10104-8. [Cited on pages 34 and 35.]

C. E. C. I. on Breast Cancer. Koning breast CT, 2022. URL https://healthcare-quality.jrc.ec.europa.eu/european-breast-cancer-guidelines/screening-tests. [Cited on page 24.]

A. M. O'Connell, A. Karellas, S. Vedantham, and D. T. Kawakyu-O'Connor. Newer technologies in breast cancer imaging: dedicated cone-beam breast computed tomography. In *Seminars in Ultrasound, CT and MRI*, volume 39, pages 106–113. Elsevier, 2018. [Cited on page 27.]

S. Pacilè, C. Dullin, P. Baran, M. Tonutti, C. Perske, U. Fischer, J. Albers, F. Arfelli, D. Dreossi, K. Pavlov, et al. Free propagation phase-contrast breast ct provides higher image quality than cone-beam breast-ct at low radiation doses: a feasibility study on human mastectomies. *Scientific reports*, 9(1):13762, 2019. [Cited on pages 77 and 103.]

D. Paganin, S. Mayo, T. E. Gureyev, P. R. Miller, and S. W. Wilkins. Simultaneous phase and amplitude extraction from a single defocused image of a homogeneous object. *Journal of microscopy*, 206(1):33–40, 2002. doi: 10.1046/j.1365-2818.2002.01010.x. [Cited on pages 67 and 115.]

M. A. Papas and A. C. Klassen. Pain and discomfort associated with mammography among urban low-income african–american women. *Journal of community health*, 30(4):253–267, 2005. doi: 10.1007/s10900-005-3704-5. [Cited on page 19.]

S. E. Park, J. G. Kim, M. Hegazy, M. H. Cho, and S. Y. Lee. A flat-field correction method for photon-counting-detector-based micro-CT. In *Proc. SPIE*, volume 9033, page 90335, 2014. doi: 10.1117/12.2043317. [Cited on page 63.]

S. K. Patterson and M. A. Roubidoux. Update on new technologies in digital mammography. *International journal of women's health*, 6:781, 2014. [Cited on page 24.]

K. M. Pelliccia, Daniele and and K. S. Morgan. Theory of X-ray phase-contrast imaging. In P. Russo, editor, *Handbook of X-ray imaging: Physics and Technology*, chapter 49, pages 971–997. Taylor and Francis, 2018. ISBN 978-1-4987-4152-1. doi: 10.1201/9781351228251. [Cited on pages 33, 35, and 67.]

L. M. A. Peña, S. Donato, D. Bonazza, L. Brombal, F. Arfelli, G. Tromba, and R. Longo. Optimization of x-ray phase-contrast micro tomography for virtual histology. *Physica Medica: European Journal of Medical Physics*, 104:S47, 2022. doi: 10.1016/S1120-1797(22)02224-4. [Cited on page 130.]

D. Pennicard and H. Graafsma. Simulated performance of high-Z detectors with medipix3 readout. *Journal of Instrumentation*, 6(06):P06007, 2011. doi: 10.1088/1748-0221/6/06/P06007. [Cited on page 63.]

F. Pernicka and I. D. McLean. Dosimetry in diagnostic radiology: an international code of practice. Technical Report Technical Reports Series No. 457, International Atomic Energy Agency, Vienna International Centre, Vienna, Austria, 2007. [Cited on page 47.]

N. Perry, M. Broeders, C. de Wolf, S. Törnberg, R. Holland, and L. von Karsa. European guidelines for quality assurance in breast cancer screening and diagnosis. -summary document. *Oncology in Clinical Practice*, 4(2):74–86, 2008. [Cited on page 47.]

X.-A. Phi, A. Tagliafico, N. Houssami, M. J. Greuter, and G. H. de Bock. Digital breast tomosynthesis for breast cancer screening and diagnosis in women with dense breasts–a systematic review and meta-analysis. *BMC cancer*, 18(1):1–9, 2018. [Cited on page 24.]

A. Piai, A. Contillo, F. Arfelli, D. Bonazza, L. Brombal, M. A. Cova, P. Delogu, V. D. Trapani, S. Donato, B. Golosio, G. Mettivier, P. Oliva, L. Rigon, A. Taibi, M. Tonutti, G. Tromba, F. Zanconati, and R. Longo. Quantitative characterization of breast tissues with dedicated CT imaging. *Physics in Medicine & Biology*, 64(15):155011, aug 2019. doi: 10.1088/1361-6560/ab2c29. [Cited on pages 68, 69, 76, and 135.]

E. D. Pisano, C. Gatsonis, E. Hendrick, M. Yaffe, J. K. Baum, S. Acharyya, E. F. Conant, L. L. Fajardo, L. Bassett, C. D'Orsi, et al. Diagnostic performance of digital versus film mammography for breast-cancer screening. *New England Journal of Medicine*, 353(17): 1773–1783, 2005. [Cited on page 30.]

A. Poulos and D. McLean. The application of breast compression in mammography: a new perspective. *Radiography*, 10(2):131–137, 2004. [Cited on page 19.]

E. A. Rakha, S. Badve, V. Eusebi, J. S. Reis-Filho, S. B. Fox, D. J. Dabbs, T. Decker, Z. Hodi, S. Ichihara, A. H. Lee, J. Palacios, A. L. Richardson, A. Vincent-Salomon, F. C. Schmitt, P.-H. Tan, G. M. Tse, and I. O. Ellis. Breast lesions of uncertain malignant nature and limited metastatic potential: proposals to improve their recognition and clinical management. 68 (1):45–56, 2016. ISSN 03090167. doi: 10.1111/his.12861. URL https://onlinelibrary.wiley.com/doi/10.1111/his.12861. [Cited on page 17.]

L. Rigon. *X-ray imaging with coherent sources*, volume 4 of *Comprehensive Biomedical Physics*. Elsevier, 2014. [Cited on pages 33, 34, and 35.]

A.-C. Roessler, F. Althoff, F. Jaeger, W. A. Kalender, and E. Wenkel. Optical measurement of dimensional parameters of the breast with subjects in prone position. *Journal of Medical Imaging*, 2(3):034001, 2015. [Cited on page 90.]

M. Ross and W. Pawlina. *Histology: a text and atlas: with correlated cell and molecular biology*. Lippincott Williams and Wilkins, USA, sixth edition edition, 2011. [Cited on pages 111 and 124.]

A. Rößler, E. Wenkel, F. Althoff, and W. Kalender. The influence of patient positioning in breast ct on breast tissue coverage and patient comfort. *Senologie-Zeitschrift für Mammadiagnostik und-therapie*, 12(02):96–103, 2015. [Cited on pages 27 and 79.]

D. R. Rutter, M. Calnan, M. Vaile, S. Field, and K. A. Wade. Discomfort and pain during mammography: description, prediction, and prevention. *British Medical Journal*, 305(6851):443–445, 1992. [Cited on page 19.]

M. Saccomano, J. Albers, G. Tromba, M. Dobrivojević Radmilović, S. Gajović, F. Alves, and C. Dullin. Synchrotron inline phase contrast μct enables detailed virtual histology of embedded soft-tissue samples with and without staining. *Journal of synchrotron radiation*, 25 (4):1153–1161, 2018. [Cited on pages 109 and 112.]

E. Samei, P. Kinahan, R. M. Nishikawa, and A. Maidment. Virtual clinical trials: Why and what (special section guest editorial). *Journal of Medical Imaging*, 7(4), 2020. [Cited on page 136.]

A. Sarno, G. Mettivier, and P. Russo. Dedicated breast computed tomography: basic aspects. *Medical physics*, 42(6Part1):2786–2804, 2015. doi: 10.1118/1.4919441. [Cited on pages 25 and 30.]

A. Sarno, G. Mettivier, R. M. Tucciariello, K. Bliznakova, J. M. Boone, I. Sechopoulos, F. Di Lillo, and P. Russo. Monte carlo evaluation of glandular dose in cone-beam x-ray computed tomography dedicated to the breast: Homogeneous and heterogeneous breast models. *Physica Medica*, 51:99–107, 2018. [Cited on page 48.]

I. Sechopoulos. A review of breast tomosynthesis. part I. the image acquisition process. *Medical physics*, 40(1), 2013a. doi: 10.1118/1.4770279. [Cited on pages 25 and 30.]

I. Sechopoulos. A review of breast tomosynthesis. part ii. image reconstruction, processing and analysis, and advanced applications. *Medical physics*, 40(1):014302, 2013b. [Cited on page 25.]

I. Sechopoulos, S. Suryanarayanan, S. Vedantham, C. D'Orsi, and A. Karellas. Computation of the glandular radiation dose in digital tomosynthesis of the breast. *Medical Physics*, 34(1): 221–232, 2007. doi: 10.1118/1.2400836. URL https://aapm.onlinelibrary.wiley.com/doi/abs/10.1118/1.2400836. [Cited on page 48.]

I. Sechopoulos, S. S. J. Feng, and C. J. D'Orsi. Dosimetric characterization of a dedicated breast computed tomography clinical prototype. *Medical physics*, 37(8):4110–4120, 2010. doi: 10.1118/1.3457331. [Cited on pages 25, 26, 27, 80, and 81.]

I. Sechopoulos, K. Bliznakova, X. Qin, B. Fei, and S. S. J. Feng. Characterization of the homogeneous tissue mixture approximation in breast imaging dosimetry. *Medical physics*, 39(8):5050–5059, 2012. [Cited on pages 45, 48, and 56.]

J. Sempau, A. Sanchez-Reyes, F. Salvat, S. B. Jiang, and J. M. Fernandez-Varea. Monte Carlo simulation of electron beams from an accelerator head using PENELOPE. *Phys. Med. Biol.*, 46(187):25. [Cited on page 54.]

R. Sharma, S. Sharma, P. Sarkar, B. Singh, A. Agrawal, and D. Datta. Phantom-based feasibility studies on phase-contrast mammography at indian synchrotron facility indus-2. *Journal of medical physics*, 44(1):39, 2019. doi: 10.4103/jmp.JMP_98_18. [Cited on page 142.]

P. J. Slanetz et al. Mri of the breast and emerging technologies. *Weblink: https://www. uptodate. com/contents/mri-of-the-breast-and-emerging-technologies. Last Access: May*, 2020. [Cited on page 28.]

A. Smith. Fundamentals of breast tomosynthesis improving the performance of mammography. 2008. [Cited on page 24.]

P. Spanne, C. Raven, I. Snigireva, and A. Snigirev. In-line holography and phase-contrast microtomography with high energy x-rays. *Physics in Medicine & Biology*, 44(3):741, 1999. doi: 10.1088/0031-9155/44/3/016. [Cited on page 36.]

H. Stark, J. Woods, I. Paul, and R. Hingorani. Direct fourier reconstruction in computer tomography. *IEEE Transactions on Acoustics, Speech, and Signal Processing*, 29(2):237–245, 1981. [Cited on page 71.]

C. Sun, B. Wang, J. Li, J. Shangguan, M. Figini, K. Zhou, L. Pan, Q. Ma, and Z. Zhang. Quantitative measurement of breast carcinoma fibrosis for the prediction in the risk of bone metastasis. *American Journal of Translational Research*, 10(6):1852, 2018. [Cited on page 120.]

H. Sung, J. Ferlay, R. L. Siegel, M. Laversanne, I. Soerjomataram, A. Jemal, and F. Bray. Global Cancer Statistics 2020: GLOBOCAN Estimates of Incidence and Mortality Worldwide for 36 Cancers in 185 Countries. *CA: A Cancer Journal for Clinicians*, 71(3): 209–249, May 2021. ISSN 0007-9235, 1542-4863. doi: 10.3322/caac.21660. URL https://onlinelibrary.wiley.com/doi/10.3322/caac.21660. [Cited on page 15.]

P. Suortti and W. Thomlinson. Medical applications of synchrotron radiation. *Physics in Medicine & Biology*, 48(13):R1, 2003. [Cited on pages 32 and 41.]

S. T. Taba, B. D. Arhatari, Y. I. Nesterets, Z. Gadomkar, S. C. Mayo, D. Thompson, J. Fox, B. Kumar, Z. Prodanovic, D. Hausermann, et al. Propagation-based phase-contrast ct of the breast demonstrates higher quality than conventional absorption-based ct even at lower radiation dose. *Academic Radiology*, 28(1):e20–e26, 2021. [Cited on page 77.]

C. Tagliati, F. Cerimele, A. D. Martino, F. Capone, M. D. Matteo, N. Caputo, G. L. Pressanti, Y. Mingliang, S. Baldassarre, A. Giovagnoni, and G. M. Giuseppetti. Invasive lobular carcinoma mammographic findings: correlation with age, breast composition, and tumour size. *Polish journal of radiology*, 86:e353—e358, 2021. ISSN 1733-134X. doi: 10.5114/pjr.2021.107426. URL https://europepmc.org/articles/PMC8297481. [Cited on page 119.]

K. Taguchi and J. S. Iwanczyk. Vision 20/20: Single photon counting X-ray detectors in medical imaging. *Medical physics*, 40(10), 2013. doi: 10.1118/1.4820371. [Cited on page 61.]

T. Takahashi and S. Watanabe. Recent progress in CdTe and CdZnTe detectors. *IEEE Transactions on Nuclear Science*, 48(4):950–959, 2001. doi: 10.1109/23.958705. [Cited on page 61.]

T. Takeda, A. Momose, J. Wu, Q. Yu, T. Zeniya, T.-T. Lwin, A. Yoneyama, and Y. Itai. Vessel imaging by interferometric phase-contrast x-ray technique. *Circulation*, 105(14):1708–1712, 2002. [Cited on page 41.]

T. Tanaka, C. Honda, S. Matsuo, K. Noma, H. Oohara, N. Nitta, S. Ota, K. Tsuchiya, Y. Sakashita, A. Yamada, et al. The first trial of phase contrast imaging for digital full-field mammography using a practical molybdenum X-ray tube. *Investigative radiology*, 40 (7):385–396, 2005. doi: 10.1097/01.rli.0000165575.43381.48. [Cited on page 38.]

W. Teh and A. Wilson. The role of ultrasound in breast cancer screening. a consensus statement by the european group for breast cancer screening. *European journal of cancer*, 34(4):449–450, 1998. [Cited on page 28.]

W. Thomlinson, H. Elleaume, L. Porra, and P. Suortti. K-edge subtraction synchrotron X-ray imaging in bio-medical research. *Physica Medica*, 49:58–76, 2018. doi: 10.1016/j.ejmp.2018.04.389. [Cited on page 41.]

M. Töpperwien, F. van der Meer, C. Stadelmann, and T. Salditt. Three-dimensional virtual histology of human cerebellum by x-ray phase-contrast tomography. *Proceedings of the National Academy of Sciences*, 115(27):6940–6945, 2018. [Cited on page 112.]

G. Tromba, R. Longo, A. Abrami, F. Arfelli, A. Astolfo, P. Bregant, F. Brun, K. Casarin, V. Chenda, D. Dreossi, M. Hola, J. Kaiser, L. Mancini, R. Menk, E. Quai, E. Quaia, L. Rigon, T. Rokvic, N. Sodini, D. Sanabor, E. Schultke, M. Tonutti, A. Vascotto, F. Zanconati, M. Cova, and E. Castelli. The syrmep beamline of elettra: Clinical mammography and bio-medical applications. In *AIP Conference Proceedings*, volume 1266, pages 18–23. AIP, 2010. [Cited on page 37.]

W. Twengström, C. F. Moro, J. Romell, J. C. Larsson, E. Sparrelid, M. Björnstedt, and H. M. Hertz. Can laboratory x-ray virtual histology provide intraoperative 3D tumor resection margin assessment? *Journal of Medical Imaging*, 9 (03), Feb. 2022. ISSN 2329-4302. doi: 10.1117/1.JMI.9.3.031503. URL https://www.spiedigitallibrary.org/journals/journal-of-medical-imaging/volume-9/issue-03/031503/Can-laboratory-x-ray-virtual-histology-provide-intraoperative-3D-tumor/10.1117/1.JMI.9.3.031503.full. [Cited on pages 112 and 138.]

J. Uhlig, A. Uhlig, L. Biggemann, U. Fischer, J. Lotz, and S. Wienbeck. Diagnostic accuracy of cone-beam breast computed tomography: a systematic review and diagnostic meta-analysis. *European radiology*, 29(3):1194–1202, 2019. doi: 10.1007/s00330-018-5711-9. [Cited on pages 26 and 97.]

R. Vescovi, M. Du, V. d. Andrade, W. Scullin, D. Gürsoy, and C. Jacobsen. Tomosaic: efficient acquisition and reconstruction of teravoxel tomography data using limited-size synchrotron X-ray beams. *Journal of synchrotron radiation*, 25(5), 2018. doi: 10.1107/S1600577518010093. [Cited on page 133.]

T. Veuthey, G. Herrera, and V. I. Dodero. Dyes and stains: from molecular structure to histological application. *Frontiers in Bioscience-Landmark*, 19(1):91–112, 2014. [Cited on page 110.]

A. Vincenzi, P. De Ruvo, P. Delogu, R. Bellazzini, A. Brez, M. Minuti, M. Pinchera, and G. Spandre. Energy characterization of pixirad-1 photon counting detector system. *Journal of Instrumentation*, 10(04):C04010, 2015. doi: 10.1088/1748-0221/10/04/C04010. [Cited on page 61.]

W. L. Wagner, F. Wuennemann, S. Pacilé, J. Albers, F. Arfelli, D. Dreossi, J. Biederer, P. Konietzke, W. Stiller, M. O. Wielpütz, et al. Towards synchrotron phase-contrast lung imaging in patients–a proof-of-concept study on porcine lungs in a human-scale chest phantom. *Journal of synchrotron radiation*, 25(6), 2018. doi: 10.1107/S1600577518013401. [Cited on pages 41 and 142.]

M. Wallis, A. Tarvidon, T. Helbich, and I. Schreer. Guidelines from the european society of breast imaging for diagnostic interventional breast procedures. *European radiology*, 17(2): 581–588, 2007. [Cited on page 29.]

C. Walsh, P. Tafforeau, W. Wagner, D. Jafree, A. Bellier, C. Werlein, M. Kühnel, E. Boller, S. Walker-Samuel, J. Robertus, et al. Imaging intact human organs with local resolution of cellular structures using hierarchical phase-contrast tomography. *Nature methods*, 18(12): 1532–1541, 2021. doi: 10.1038/s41592-021-01317-x. [Cited on pages 131 and 137.]

R. Walsh, P. Kornguth, M. Soo, R. Bentley, and D. DeLong. Axillary lymph nodes: mammographic, pathologic, and clinical correlation. *AJR. American journal of roentgenology*, 168 (1):33–38, 1997. [Cited on pages 27 and 28.]

W. Wang, R. Qiu, L. Ren, H. Liu, Z. Wu, C. Li, Y. Niu, and J. Li. Monte carlo calculation of conversion coefficients for dose estimation in mammography based on a 3d detailed breast model. *Medical Physics*, 44(6):2503–2514, 2017. [Cited on page 48.]

L. Watson. The role of ultrasound in breast imaging. *Radiologic Technology*, 71(5):441–441, 2000. [Cited on page 28.]

P. Wellman. *Tactile Imaging*. PhD thesis, Cambridge, MA: Harvard University's Division of Engineering and Applied Sciences, 1999. [Cited on page 50.]

S. Wienbeck, J. Lotz, and U. Fischer. Review of clinical studies and first clinical experiences with a commercially available cone-beam breast CT in europe. *Clinical imaging*, 42:50–59, 2017. doi: 10.1016/j.clinimag.2016.11.011. [Cited on page 26.]

S. Wilkins, Y. I. Nesterets, T. Gureyev, S. Mayo, A. Pogany, and A. Stevenson. On the evolution and relative merits of hard X-ray phase-contrast imaging methods. *Phil. Trans. R. Soc. A*, 372(2010):20130021, 2014. doi: 10.1098/rsta.2013.0021. [Cited on page 35.]

L. Wilkinson, V. Thomas, and N. Sharma. Microcalcification on mammography: approaches to interpretation and biopsy. *The British journal of radiology*, 90(1069):20160594, 2017. [Cited on page 18.]

M. J. Willemink, T. Leiner, P. A. de Jong, L. M. de Heer, R. A. Nievelstein, A. M. Schilham, and R. P. Budde. Iterative reconstruction techniques for computed tomography part 2: initial results in dose reduction and image quality. *European radiology*, 23(6):1632–1642, 2013. [Cited on page 98.]

X. Wu, G. T. Barnes, and D. Tucker. Spectral dependence of glandular tissue dose in screen-film mammography. *Radiology*, 179(1):143–148, 1991. [Cited on pages 46, 47, and 79.]

X. Wu, E. L. Gingold, G. T. Barnes, and D. M. Tucker. Normalized average glandular dose in molybdenum target-rhodium filter and rhodium target-rhodium filter mammography. *Radiology*, 193(1):83–89, 1994. [Cited on pages 45 and 46.]

M. J. Yaffe. Digital mammography. In *PACS*, pages 363–371. Springer, 2006. [Cited on pages 19 and 23.]

M. J. Yaffe, R. E. Hendrick, S. A. Feig, L. N. Rothenberg, J. Och, and R. Gagne. Recommended specifications for new mammography equipment: report of the acr-cdc focus group on mammography equipment. *Radiology*, 197(1):19–26, 1995. [Cited on page 23.]

Y. Yang, D. Zhang, F. Yang, M. Teng, Y. Du, and K. Huang. Post-processing method for the removal of mixed ring artifacts in ct images. *Optics Express*, 28(21):30362–30378, 2020. [Cited on page 70.]

Y.-L. Yang, B.-B. Liu, X. Zhang, and L. Fu. Invasive micropapillary carcinoma of the breast: an update. *Archives of pathology & laboratory medicine*, 140(8):799–805, 2016. [Cited on page 118.]

D. C. Zaha. Significance of immunohistochemistry in breast cancer. *World journal of clinical oncology*, 5(3):382, 2014. [Cited on page 109.]

I. Zanette, P. B. Noël, M. B. Cardoso, M. A. Kimm, F. Pfeiffer, et al. Three-dimensional non-destructive soft-tissue visualization with x-ray staining micro-tomography. *Scientific reports*, 5(1):1–7, 2015. [Cited on page 109.]

S.-A. Zhou and A. Brahme. Development of phase-contrast X-ray imaging techniques and potential medical applications. *Physica Medica*, 24(3):129–148, 2008. doi: 10.1016/j.ejmp.2008.05.006. [Cited on pages 34, 35, and 36.]

Y. Zhu, A. M. O'Connell, Y. Ma, A. Liu, H. Li, Y. Zhang, X. Zhang, and Z. Ye. Dedicated breast ct: State of the art—part ii. clinical application and future outlook. *European Radiology*, pages 1–15, 2021. [Cited on page 27.]

Y. Zhu, A. M. O'Connell, Y. Ma, A. Liu, H. Li, Y. Zhang, X. Zhang, and Z. Ye. Dedicated breast ct: state of the art—part i. historical evolution and technical aspects. *European Radiology*, 32(3):1579–1589, 2022. [Cited on page 26.]